UNIVERSITY OF HAWAII
LIBRARY
JUL 18 '57

The
PHILOSOPHICAL MAGAZINE

FIRST PUBLISHED IN 1798

l. 2 Eighth Series No. 18 June 1957

A Journal of Theoretical Experimental and Applied Physics

EDITOR
PROFESSOR N. F. MOTT, M.A., D.Sc., F.R.S.

EDITORIAL BOARD
SIR LAWRENCE BRAGG, O.B.E., M.C., M.A., D.Sc., F.R.S.
SIR GEORGE THOMSON, M.A., D.Sc., F.R.S.
PROFESSOR A. M. TYNDALL, C.B.E., D.Sc., F.R.S.

PRICE £1 5s. 0d.
Annual Subscription £13 10s. 0d. payable in advance

ALERE FLAMMAM.
Printed and Published by
TAYLOR & FRANCIS LTD.
RED LION COURT, FLEET STREET, LONDON, E.C.4

The Scientific Work of René Descartes

(1596–1650)

By

J. F. SCOTT, B.A., M.Sc., Ph.D.

With a foreword by H. W. TURNBULL, M.A., F.R.S.

This book puts the chief mathematical and physical discoveries of Descartes in an accessible form, and fills an outstanding gap upon the shelf devoted to the history of philosophy and science.

There is to be found in this volume the considerable contribution that Descartes made to the physical sciences, which involved much accurate work in geometrical optics and its bearing upon the practical problem of fashioning lenses, as also the deeper problems of light and sight and colour. The careful treatment that Dr. Scott has accorded to this work of Descartes is welcome, is well worth reading and will be an asset to all libraries. Publication is recommended and approved by the Publication Fund Committee of the University of London

212 *pages*, 7" × 10", *amply illustrated*

Price £1 - 0 - 0 net **First published July 1952**

Printed & Published by
TAYLOR & FRANCIS, LTD.
RED LION COURT, FLEET STREET, LONDON, E.C.4

The Anhysteretic Magnetization of Permanent Magnet Alloys†

By E. P. Wohlfarth
Department of Mathematics, Imperial College, London

[Received March 6, 1957]

Summary

Calculations on the basis of the single domain treatment are reported of the anhysteretic magnetization, the anhysteretic remanent magnetization and the initial magnetization for a simple model of a permanent magnet alloy, and the results are compared with experimental curves for Alcomax III (Gould and McCaig 1954).

§ 1. Introduction

The anhysteretic magnetization $I_a = I_a(H)$ of a ferromagnetic specimen is that magnetization which the specimen retains after the application of a direct field H on which is superposed an alternating field of initial amplitude H' which is then slowly reduced to zero. The function $I_a(H)$ is single valued and independent of the value of H' as long as this is sufficiently large (see § 4). If H is the internal field, i.e. corrected for the external demagnetizing factor which depends on the shape of the specimen, then it is found experimentally that the initial slope of the $I_a(H)$ curve is exceedingly large. The theoretical treatment given below and elsewhere indicates that this slope is, in fact, infinite, and where a finite value is observed it has usually been assumed that there is present in the specimen a certain amount of internal demagnetization. This may be due to the presence of grain boundaries, non-magnetic inclusions or other structural imperfections. If the effect is characterized by an internal demagnetizing factor N_i, then the initial slope of the anhysteretic magnetization curve is given by (Néel 1943)

$$[dI_a(H)/dH]_{H\to 0} = 1/N_i. \quad . \quad . \quad . \quad . \quad . \quad . \quad (1)$$

Measurements of anhysteretic magnetization curves have been reported from time to time for a variety of materials. Kahan (1934) obtained results for nickel and cobalt specimens over a range of temperatures, and used relation (1) to determine the temperature dependence of N_i. Similar measurements for nickel and cobalt alloys were reported by Kranz (1956), who related the measured values of N_i directly to some structural properties of the specimens. The structure of permanent magnet alloys has a great influence on their magnetic properties, and it is here that such measurements are of special interest. Experiments on cobalt steel and an Fe–Ni–Al alloy have been reported by Forrer (1943) and Néel *et al.* (1943), and on Magnico by Bulgakov (1950). These authors do not give full anhysteretic magnetization curves but only report the values of N_i. Recently, however, complete curves for Alcomax III have been published by Gould and McCaig (1954). Apart from curves giving $I_a(H)$ parallel and perpendicular to the preferred direction of this anisotropic material, these authors also give corresponding results for the anhysteretic remanent magnetization $I_{ar}(H)$. These are obtained by measuring the magnetization which the specimen retains after the application of the usual anhysteretic treatment and *subsequent* removal of the direct field H. Curves are also given which relate the initial magnetization with direct field H along the two directions. All six curves are reproduced in fig. 2.

---

† Communicated by the Author.

In the present paper theoretical curves corresponding directly to those measured are obtained on the basis of the single domain treatment of Stoner and Wohlfarth (1948).

§ 2. A SIMPLE MODEL FOR A PERMANENT MAGNET ALLOY

The work of Nesbitt and Williams (1955) and others shows that the permanent magnet properties of alloys of the Alcomax type are due to the shape anisotropy of single domain cobalt rich precipitates, and that the anisotropy resulting from the magnetic treatment is due to the preferential nucleation and growth of the precipitates parallel to the field direction (for a review see Kittel and Galt 1956, Wohlfarth 1956). Without entering into the finer details of the structure of these materials, it is possible to describe their magnetic properties by means of the following model, which is both physically reasonable and amenable to simple calculations.

Consider an assembly of prolate spheroidal single domain precipitate particles each of volume V_0, saturation magnetization I_{00} and shape anisotropy coefficient $N_0(m)$, where m is the dimensional ratio of the particles. Further, consider the particles to be oriented at a suitably defined average angle $\theta_{\parallel}$ with the preferred direction and $\theta_{\perp}$ with the perpendicular direction. Ideally, $\theta_{\parallel}=0°$ and $\theta_{\perp}=90°$, but this state of affairs, which would lead to rectangular hysteresis cycles, is never quite realized in practice; in general $\theta_{\parallel}$ is some small angle which may actually be estimated from the measurements under discussion. If the packing factor of the particles is denoted by p, where $p=nV_0$ with n the number of particles per unit volume of the material (precipitates plus matrix), then the saturation magnetization of the material is I_0, where

$$I_0=pI_{00}. \qquad (2)$$

It is difficult to take precise account of the effects of particle interaction (Wohlfarth 1955 a), but in certain circumstances this may be done by defining an effective shape anisotropy coefficient $N(m)$, where, formally,

$$N(m)=f(p)N_0(m). \qquad (3)$$

The magnetization I of the material in an applied field H is given by

$$I=pI_{00}j=I_0j, \quad \ldots \ldots \ldots \quad (4)$$

where

$$H=N(m)I_{00}h=\{f(p)/p\}N_0(m)I_0h. \quad \ldots \ldots \quad (5)$$

Here $j=\cos\phi$, where ϕ is the angle between the directions of I_0 and H, and h are the reduced magnetization and field parameters used by Stoner and Wohlfarth (1948). For a given value of h, j depends on the orientation angle θ between H and the major axis of the particle, so that different I, H relations are obtained depending on whether $\theta=\theta_{\parallel}$ or $\theta_{\perp}$.

Since the function $f(p)$ in relation (3) is in general difficult to determine, it is necessary to obtain the scale factor relating H and h in relation (5) in a different way. If H_c is the coercive force measured parallel to the preferred orientation then, from (5),

$$H_c=\{f(p)/p\}N_0(m)I_0\,|h_0(\theta_{\parallel})|, \quad \ldots \ldots \quad (6)$$

where $h_0(\theta)$ is the reduced critical field calculated by Stoner and Wohlfarth (table 4). Hence

$$H=\{H_c/|h_0(\theta_{\parallel})|\}h. \quad \ldots \ldots \ldots \quad (7)$$

As shown in § 3, relations (4) and (7) may be used to dicsuss the anhysteretic magnetization of a material with given values of the four quantities I_0, H_c, $\theta_{\parallel}$, $\theta_{\perp}$. The assumptions underlying the discussion are considered in § 4.

§ 3. APPLICATION OF THE SINGLE DOMAIN TREATMENT

Figure 1 shows the reduced hysteresis cycle relating j and h for $\theta=20°$, as an example.

Fig. 1

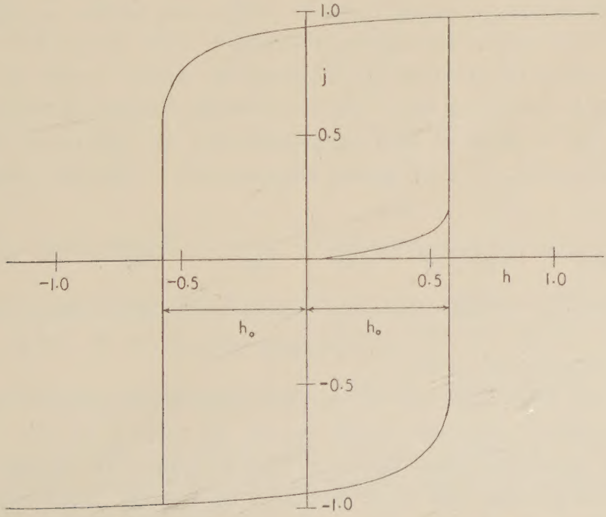

Hysteresis cycle and initial magnetization curve for $\theta=20°$.

Let the reduced direct field applied to the particles be h and the reduced initial amplitude of the alternating field h'. If

$$h' > h + |h_0(\theta)|, \quad . \quad . \quad . \quad . \quad . \quad . \quad . \quad . \quad . \quad (8)$$

then under the influence of the alternating field the magnetization initially describes complete cycles, of the form shown in fig. 1. If the alternating field is now reduced then eventually its amplitude reaches a value h'', where

$$h'' < h + |h_0(\theta)| < h', \quad . \quad . \quad . \quad . \quad . \quad . \quad . \quad . \quad (9)$$

which is insufficient for the magnetization to reverse back into a direction opposite to that of h. Further reversals of the alternating field with decreasing amplitude cause the magnetization to describe smaller and smaller arcs on the upper branch of the cycle, ending up at a point $j = j(h)$ on this branch when the alternating field is zero.

The anhysteretic magnetization curve is thus made up of the vertical line from the origin to the remanence point $j = \cos\theta$, and that part of the upper branch of the cycle which lies in the first quadrant. If, after completion of the anhysteretic treatment, h is reduced to zero, the magnetization returns to the remanence point *independently of h*. The anhysteretic remanence curve is thus made up of the same vertical line to the remanence point and the horizontal line passing through this point and lying in the first quadrant. As discussed in § 4 the two types of magnetization are reduced if h', the reduced initial amplitude of the alternating field, is too small.

In order to transform the reduced curves just discussed so as to be applicable directly to Alcomax III it is necessary to know the values of the four quantities I_0, H_c, $\theta_{\parallel}$, $\theta_{\perp}$, as described in § 2. These are obtained as follows :

Gould and McCaig's experimental curves are shown in fig. 2. From curve 1 and the above discussion it follows that $4\pi I_0 = 14{\cdot}1 \times 10^3$ gauss. The coercive force of Alcomax III is given by Anon. (1952) as 670 oersted. From curves 3 and 4 of fig. 2 the saturation values of the anhysteretic remanence curve parallel and perpendicular to the preferred direction are $4\pi I_r = 13{\cdot}0$ and $4{\cdot}7 \times 10^3$ gauss respectively. Hence, from the above discussion

$$\theta_{\parallel} = \cos^{-1}(13{\cdot}0/14{\cdot}1) \simeq 23°, \quad \theta_{\perp} = \cos^{-1}(4{\cdot}7/14{\cdot}1) \simeq 70°.$$

In the present calculations the angles have been taken to equal 20° and 70°, for which full theoretical data are given in tables 3 and 4 of Stoner and Wohlfarth (1948).

In order to take account of internal demagnetization (cf. § 1) it is necessary to shear the calculated curves according to the value of N_i, the internal demagnetizing factor. This is given by Gould and McCaig as $1/N_i = 103$, as read off from curve 1 of fig. 2. The final calculated curves are shown in fig. 3. The overall agreement between the two sets of curves of figs. 2 and 3 is good. There are some obvious discrepancies, and the reasons for these are discussed in § 4.

Fig. 2

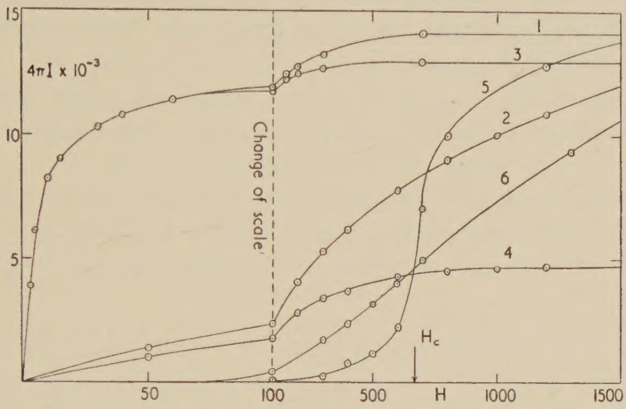

Experimental magnetization curves, after Gould and McCaig (1954, with acknowledgments to the authors and the Physical Society).

1. Anhysteretic curve parallel to preferred direction.
2. Anhysteretic curve perpendicular to preferred direction.
3. Anhysteretic remanence curve parallel to preferred direction.
4. Anhysteretic remanence curve perpendicular to preferred direction.
5. Initial magnetization curve parallel to preferred direction.
6. Initial magnetization curve perpendicular to preferred direction.

Fig. 3

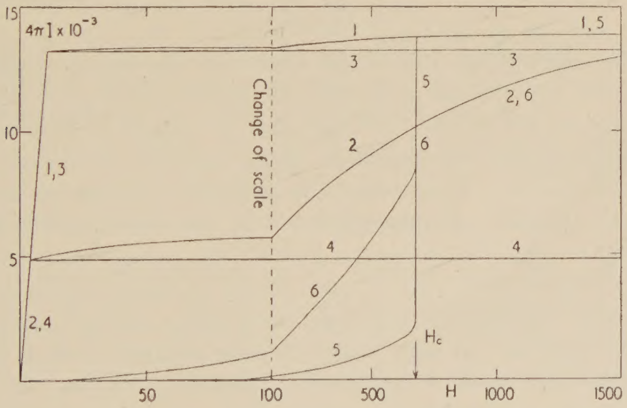

Calculated magnetization curves ; see caption to fig. 2.

§ 4. Discussion

The assumptions underlying the present calculations include the following :

(1) The precipitate particles are single domains. The electron microscope studies of Heidenreich and Nesbitt (1952) and others show that this assumption is reasonable.

(2) All the particles have the same shape. Shape variations may be quite large but, without fuller information, it is impossible to take adequate account of them. As discussed by Wohlfarth (1954) shape variations lead to a smoothing out of the magnetization curves, which would bring the calculated curves of fig. 3 into better agreement with those observed (fig. 2).

(3) The orientation angles of the particles are fixed at $\theta_{\parallel}$ and $\theta_{\perp}$. Fluctuations about these two orientations may well occur; these again would cause the calculated curves to be smoothed out.

(4) The matrix of the permanent magnet material is non-magnetic. It would be difficult to take account of any weak ferromagnetism of the matrix whose magnetization presumably changes by boundary movements.

(5) The internal demagnetizing factor is isotropic. Gould and McCaig actually discuss the possibility of N_i being anisotropic, but no conclusions on this point can be drawn at present since the precise origin of the internal demagnetization is unknown.

(6) The initial amplitude H' of the alternating field is large enough for complete cycles to be described when this field is first applied. Gould and McCaig observed that if H' is too small the magnetization drops steeply. This decrease may be explained as follows: For an assembly of particles with orientation angle θ and corresponding reduced critical field $h_0(\theta)$ complete cycles are described initially only if relation (8) for the reduced field values is satisfied. If, however,

$$h'+h<|h_0(\theta)|, \qquad \text{. . . . . (10)}$$

and if prior to the application of the fields the assembly is demagnetized, then during the process the magnetization of half the particles describes arcs on the upper branch of the cycle and of the other half on the lower branch, no discontinuous reversals being possible in either direction. The final anhysteretic magnetization acquired in the reduced field h is now equal to the *initial* magnetization in this field, and no longer that corresponding to the magnetization at h on the upper branch of the cycle (see fig. 1). A comparison of curves 1 and 5 of figs. 2 and 3 (showing the fully developed anhysteretic magnetization curve and the initial magnetization curve parallel to the preferred orientation) shows that if (10) applies the decrease of the anhysteretic magnetization may be very large. The anhysteretic remanence, in particular, vanishes completely under these conditions. The situation is here completely analogous to that which obtains during the acquisition of the normal static remanent magnetization of a particle assembly after the application of a direct field (Wohlfarth 1955 b). In fact, a curve relating $I_{ar}(H)$ with $(H+H')$ is, according to this discussion, similar in shape to that relating the static remanence $I_r(H)$ with direct field H. Both curves drop to zero values below the critical field. If variations of the particle shape, orientation angles etc. occur which tend to cause fluctuations of the critical field throughout the assembly, the decrease of the magnetization does not take place suddenly. In such cases the decrease will first make itself felt when the combined fields $(H+H')$ lie below the highest critical field of any of the particles, the decrease being most pronounced when $(H+H')$ is somewhat above H_c, the bulk coercivity (Wohlfarth 1955 b). Gould and McCaig's reported decrease occurs when H' is rather below 1000 oersted compared with $H_c=670$ oersted.

§ 5. CONCLUSION

The calculations described show that the single domain treatment gives an adequate account of the anhysteretic magnetization of permanent magnet alloys. The measured curves shown in fig. 2 provide considerable potential information about the structure of such an alloy, Alcomax III, such as the degree of particle alignment ($\theta_{\parallel}$ and $\theta_{\perp}$), fluctuations of the critical fields (smoothness of the curves compared with those calculated; fig. 3) and internal demagnetization (N_i). It may, therefore, be reasonable to suggest an extension of the measurements to other alloys with a view to correlating their structural and magnetic properties. In particular, information is required which might lead eventually to a precise determination of the origin of the internal demagnetization effect.

REFERENCES

ANON., 1952, *Permanent Magnets* (Sheffield : P.M.A.).
BULGAKOV, N. V., 1950, *Dokl. Akad. Nauk. S.S.S.R.*, **70,** 205.
FORRER, R., 1943, *Cahiers de Phys.*, **15,** 57.
GOULD, J. E., and McCAIG, M., 1954, *Proc. Phys. Soc.* B, **67,** 584.
HEIDENREICH, R. D., and NESBITT, E. A., 1952, *J. Appl. Phys.*, **23,** 352.
KAHAN, T., 1934, *J. Phys. Radium*, **5,** 463.
KITTEL, C., and GALT, J. K., 1956, *Solid State Physics*, **3,** 437.
KRANZ, J., 1956, *Beiträge zur Theorie des Ferromagnetismus und der Magnetisierungskurve* (ed. Köster, W.) (Berlin : Springer), p. 180.
NÉEL, L., 1943, *Cahiers de Phys.*, **17,** 47.
NÉEL, L., FORRER, R., JANET, N., and BAFFIE, R., 1943, *Cahiers de Phys.*, **17,** 51.
NESBITT, E. A., and HEIDENREICH, R. D., 1952, *J. Appl. Phys.*, **23,** 366.
NESBITT, E. A., and WILLIAMS, H. J., 1955, *J. Appl. Phys.*, **26,** 1217.
STONER, E. C., and WOHLFARTH, E. P., 1948, *Phil. Trans. Roy. Soc.* A, **240,** 599.
WOHLFARTH, E. P., 1954, *Research*, **7,** S18 ; 1955 a, *Proc. Roy. Soc.* A, **232,** 208 ; 1955 b, *Research*, **8,** S42 ; 1956, *Sci. J. Roy. Coll. Sci.*, **26,** 19.

Magnetic Saturation in Alloys of Neodymium at Low Temperatures†

By J. M. Lock
Royal Radar Establishment, Gt. Malvern, Worcs.

[Received March 13, 1957]

Abstract

The magnetization of alloys of neodymium with lanthanum has been measured from room temperature down to 1·5°K. Above about 15°K the susceptibility is field-independent and obeys a Curie–Weiss law modified by a small temperature-independent paramagnetic term, $\chi=C/(T-\theta)+K$. The Curie constant C gives effective atomic moments for all alloys in approximate agreement with the theoretical value for the Nd^{3+} ion, 3·62 μ_B per atom. At lower temperatures the alloys show striking saturation effects, and it is suggested that this can be accounted for in terms of a model in which the magnetic interactions between neodymium atoms are anti-ferromagnetic for nearest neighbours but ferromagnetic for more distant neighbours.

§ 1. Introduction

In a previous paper (Lock, to be published, referred to hereafter as L), it has been reported that a number of the rare-earth elements including neodymium exhibit magnetic anomalies at low temperatures which appear to be of an anti-ferromagnetic type. In order to study the effect of magnetic dilution on these anomalies susceptibility measurements have been carried out on alloys of neodymium with lanthanum varying in composition from 20% to 75% by weight of the former, at temperatures down to 1·3°K.

§ 2. Experimental Details

A Sucksmith balance apparatus previously described (L) has been used for the susceptibility measurements, which have mostly been carried out in fields up to 4780 gauss. A few measurements, using a larger electromagnet, have been made up to 10 000 gauss.

Three specimens, containing 20·5% (alloy 1), 43·5% (alloy 2), and 73·3% (alloy 3) neodymium by weight, were supplied by Johnson, Matthey and Co., Ltd. They were prepared by melting the pure metals together, and a portion of each was analysed afterwards. They were said to contain less than 0·003% iron impurity. X-ray powder photographs showed that their crystal structure was predominantly hexagonal close-packed. For the magnetic measurements pieces weighing 0·04 to 0·3 g were cut from the main alloy block.

---

† Communicated by the Author.

All three specimens have been investigated from room temperature down to about 1·3°K. Over the upper part of the range the measurements were made in two fields only, 4780 gauss and 2530 gauss, and the susceptibility was deduced from the slope of the straight line joining these two points on a magnetization curve, plotting magnetic moment against applied field. At the lowest temperatures where marked saturation effects became apparent measurements were made in several different fields so that a complete magnetization curve could be plotted.

§ 3. Results

Above about 15 K all three alloys showed almost pure paramagnetic behaviour (susceptibility field-independent), and fig. 1 shows a plot of $1/\chi$ against T in this range. In each case the susceptibility obeys a

Fig. 1

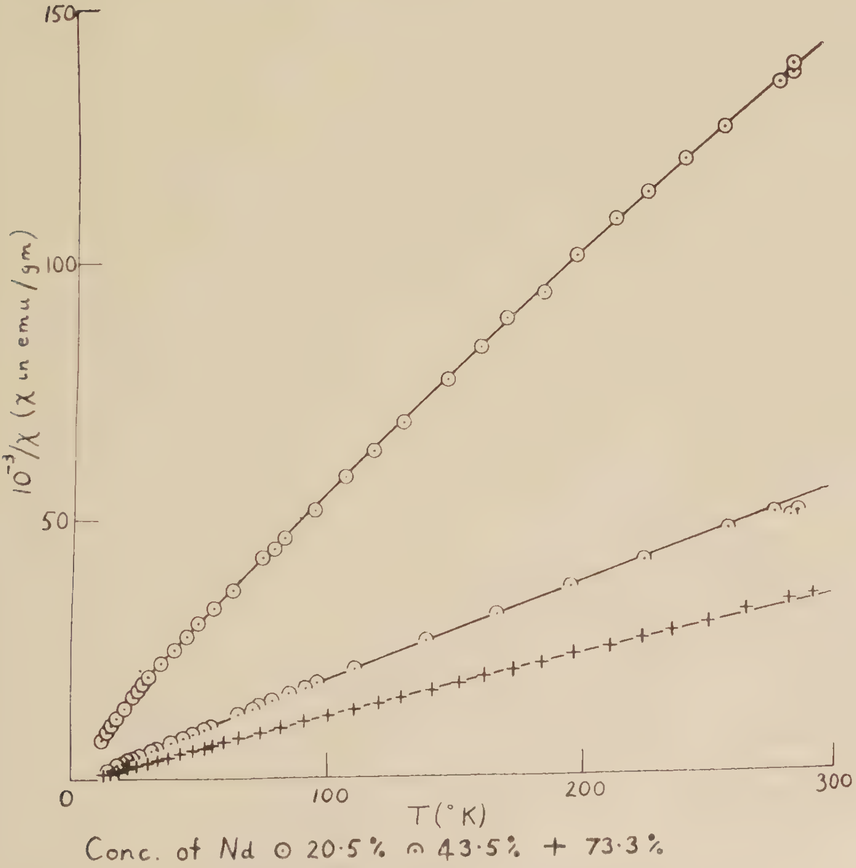

Nd alloys. Temperature variation of $1/\chi$.

Curie–Weiss law modified by a small term corresponding to temperature-independent paramagnetism, similar to the results for pure neodymium (L). The Curie constants per gramme for the three alloys are given in the table, together with the effective moments per atom of neodymium.

At sufficiently low temperatures large saturation effects occur, and fig. 2 shows typical magnetization curves for alloy 3 at a number of different temperatures, the magnetic moment being measured in Bohr magnetons (μ_B) per atom of neodymium. Two magnetization curves for pure neodymium are also plotted for comparison. An attempt to estimate the true saturation moment of alloy 2 at 1·2°K was made by using higher fields, but even at 10 000 gauss the magnetic moment was still increasing appreciably, and assuming an exponential approach to saturation, was still 10% below its saturation value, estimated as $1{\cdot}2\,\mu_B$ per atom.

Fig. 2

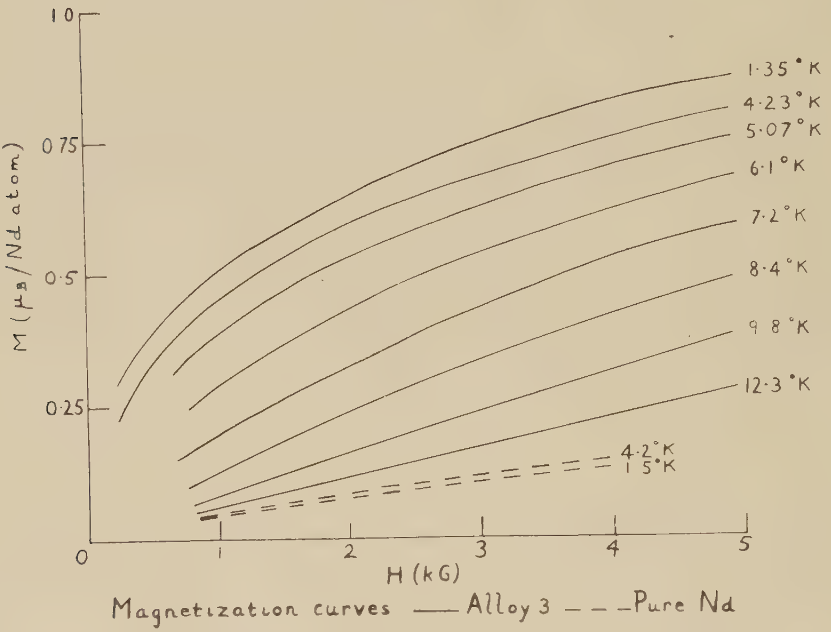

Figure 2 shows that saturation effects decrease as the temperature is raised, the magnetization curves becoming practically linear for alloy 3 between 8° and 10°K. A better estimate of this temperature is obtained by plotting M_0 against temperature, where M_0 is the intercept on the axis of M of the straight line joining two points on the magnetization curves corresponding to standard fields, in this case 4780 and 2530 gauss, and is thus a measure of the non-linearity of the curve. This has been done in fig. 3, and it is seen that for all three alloys M_0 decreases with increasing temperature, falling sharply over an intermediate range, and then tailing off towards zero at higher temperatures. By ignoring this tail and extrapolating the steeply falling portion of the curve, comparative values of the temperature T_c at which non-linear effects first appear in the magnetization curves of the alloys may be obtained, and are given in the table, together with rough estimates of the saturation moment at 1·2°K.

Fig. 3

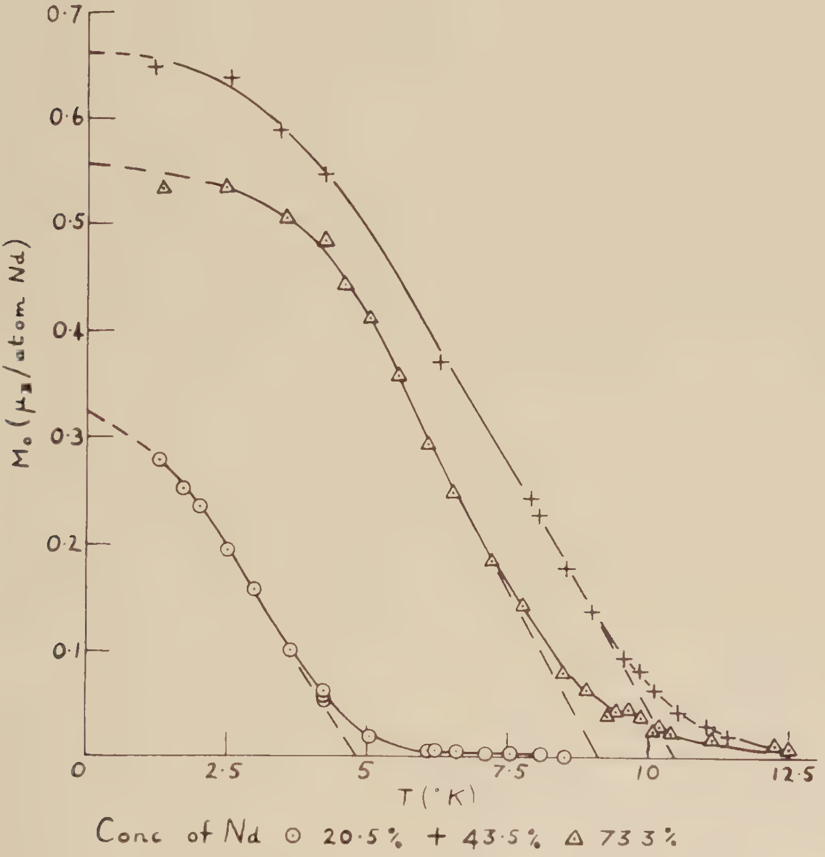

Nd alloys. Temperature variation of M_0.

Composition of alloy (% Nd)	T_c (°K)	Saturation moment (μ_B/atom of Nd)	Curie constant per g × 10^6	Eff. moment (μ_B)
100	7·5 †	—	9470	3·32
73·3	9·1	1·1	7250	3·39
43·5	10·4	1·2	5000	3·64
20·5	4·8	0·8	1870	3·25

† Néel temperature.

The specific heat of alloy 2 has also been measured (L. M. Roberts, private communication). After an approximation to the lattice contribution has been subtracted, for which purpose the atomic heat of pure lanthanum has been used (Parkinson *et al.* 1951), the remaining heat capacity shows a spread out maximum centred on 7·5°K, giving very roughly an extra entropy of 1·1 cal/deg per g atom of neodymium.

§ 4. Discussion

The large saturation effects in these alloys were at first considered to be evidence of ferromagnetism, T_c being a genuine ferromagnetic Curie temperature. However, this hypothesis leaves two curious features unexplained. Firstly, the effective atomic moments of the alloys derived from the calculated Curie constants are in rough agreement with the value $3{\cdot}62\,\mu_B$ per atom calculated for the trivalent neodymium ion in a $^4I_{9/2}$ state (Van Vleck 1932), and if ferromagnetic interactions between these ions is the cause of the low-temperature behaviour a saturation moment of $Jg\mu_B=36/11\,\mu_B$ per atom would be expected, more than $2\frac{1}{2}$ times the greatest value actually obtained. Secondly, it is possible to plot the values of T_c against the mean separation of neodymium atoms in the alloys (fig. 4), and a smooth curve through these points also passes very near a point representing the Néel temperature of pure neodymium, which is believed to become anti-ferromagnetic at 7·5°K (L). It is difficult to believe that such a drastic change in properties could be due to the small change in mean atomic separation from 3·66 Å (pure Nd) to 4·09 Å (73·3% Nd).

Fig. 4

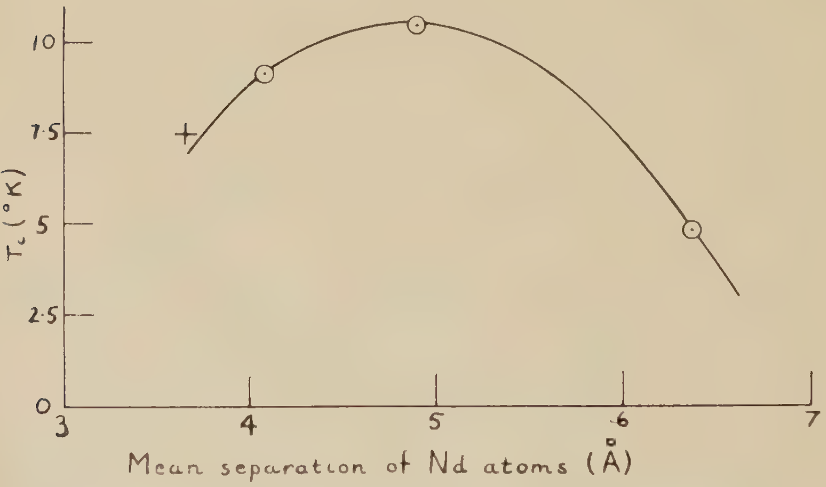

Nd alloys. Variation of T_c with atomic separation. + Néel temperature of pure Nd.

An alternative explanation of these difficulties might be that the saturation effects are due to a kind of unbalanced anti-ferromagnetism. The ordered magnetic lattice of pure neodymium could acquire a resultant moment if the added lanthanum atoms replaced neodymium atoms whose moments pointed in the same direction. If nearest neighbour interactions in neodymium are anti-ferromagnetic, but more distant neighbour interactions are ferromagnetic such an arrangement would seem to be energetically favourable, since then more of the remaining distant neighbour neodymium moments will have ferromagnetic order, while the number of antiparallel nearest neighbour moments will be unaffected. On the other hand, if the alloys are disordered solid solutions, as seems probable, then the lanthanum atoms cannot take up preferential sites in this way. The same effect might be observed however if it were possible for the moment of a neodymium atom to be transferred to a neighbouring lanthanum atom under the influence of the local magnetic forces in the metal. Such a transfer might perhaps be accomplished by electronic transitions between the 4f and 6s or 5d bands of a type similar to that postulated in the transition elements between the d and s bands to account for their poor electrical conductivity and for the properties of their alloys with the noble metals (Mott and Jones 1936).

In the concentrated neodymium alloys this model would predict a maximum saturation moment of $Jg\mu_B(=3{\cdot}27\,\mu_B)$ per atom of *lanthanum*, and alloy 3, containing 26·7% lanthanum by weight, has in fact a saturation moment of $2{\cdot}9\,\mu_B$ per atom of lanthanum, thus lending some support to the idea. When the concentration of lanthanum is of the order of 50% or greater, however, this model will no longer apply, since the original anti-ferromagnetic lattice of neodymium will then have fewer sites occupied by magnetic than by non-magnetic atoms. Under these circumstances ferromagnetic interactions between next-to-nearest and more distant neighbours should predominate, so that a saturation moment will still result, but with its value reduced to less than $Jg\mu_B$ per atom of neodymium by the anti-ferromagnetic effect of the remaining nearest neighbours, in qualitative agreement with the observations.

The anomalous specific heat of alloy 2 is in qualitative agreement with the appearance of magnetic ordering in the lattice, though the rather broad maximum found suggests that its onset is by no means sharp.

§ 5. CONCLUSION

The observed saturation effects in alloys of neodymium with lanthanum seem to be explicable on the assumption that the interactions between neodymium atoms are anti-ferromagnetic for nearest neighbours but ferromagnetic for more distant neighbours, provided that transfer of the neodymium moment to lanthanum atoms is possible to enable the missing moments to line up parallel. Such a change of sign of the interaction between neodymium atoms is in qualitative agreement with theoretical work on the variation of the exchange integral with separation of the magnetic atoms (Bethe 1933).

This work should be regarded as a preliminary investigation, and it is clear that further experiments on alloys of varying composition are desirable.

ACKNOWLEDGMENTS

The author wishes to thank Dr. D. H. Parkinson for suggesting this work and for many helpful discussions during its progress, Mr. J. F. C. Oliver for his assistance with the measurements, and Mrs. L. M. Roberts for making her specific heat measurements available. This paper is published by permission of the Controller, H.M. Stationery Office.

REFERENCES

BETHE, H., 1933, *Handbuch der Physik*, **24,** 595.
LOCK, J. M., *Proc. Phys. Soc.* (to be published).
MOTT, N. F., and JONES, H., 1936, *The Properties of Metals and Alloys* (Oxford : Clarendon Press), pp. 199, 267 and 301.
PARKINSON, D. H., SIMON, F. E., and SPEDDING, F. H., 1951, *Proc. Roy. Soc.* A, **207,** 137.
VAN VLECK, J. H., 1932, *The Theory of Electric and Magnetic Susceptibilities* (Oxford : Clarendon Press), p. 243.

The Calculation of Lattice Constants in Crystal Statistics†

By C. Domb
Wheatstone Laboratory, King's College, London

and M. F. Sykes
Clarendon Laboratory, Oxford

[Received December 24, 1956]

Summary

It is the purpose of the present paper to discuss systematic methods of evaluating and checking certain lattice constants which arise in cooperative phenomena associated with crystal lattices. Many of these constants have been evaluated previously, but little systematic description of methods used exists in the literature, and there are discrepancies between results obtained by different authors. Several new suggestions are put forward, the most important being the use of a ' no immediate return ' random walk problem, and the use of finite close-packed clusters for checking the evaluations.

§ 1. Introduction

The Mayer theory of gas condensation (Mayer and Mayer 1940, Chaps. 13, 14) represented a great step forward in the attempt of statistical mechanics to account for phase transitions. It was able to account for condensation at sufficiently low temperatures, and to indicate how a critical point arose tin liquid–vapour equilibrium. However, when it came to detailed evaluation of cluster integrals little progress was made beyond the first few terms and the problems to be faced seem indeed very formidable. Even the classification of the different types of cluster integral which arise presents great difficulties (Riddell and Uhlenbeck 1953), and for the sixth term, for example, Riddell lists 56 possible ' stars ' (Riddell 1951).

With phase transitions arising from lattice structures more progress is possible. In two dimensions an exact solution is available for a number of lattices for the Ising model in the absence of a magnetic field, and a number of additional features of the model, such as the spontaneous magnetization, can be evaluated exactly (Newell and Montroll 1953). The Ising model is formally equivalent to a regular binary solution in which the constituent atoms occupy sites on a lattice. If one of the

---

† Communicated by the Authors.

constituents is taken to be a hole we have a very crude model of liquid–vapour equilibrium which has been discussed by a number of authors, and is usually referred to as a 'lattice gas'. From a study of the properties of this model it is possible to understand much more clearly how the phenomena associated with the critical point arise. By comparing this model with the Mayer theory, Yang and Lee (1952) were able to analyse critically the conclusions of the theory, and to point out where they were valid, and where they broke down.

For the Ising model the cluster integrals are replaced by cluster sums (Fuchs 1942). If interactions of all neighbours were taken into account, these sums would be almost as difficult to classify and evaluate as cluster integrals ; the simplification in the lattice model arises largely since it is a reasonable physical approximation to take account only of nearest neighbour interactions. For all regular lattices this automatically eliminates many types of cluster, and this is particularly true of loose packed lattices. The basic problem then arising is to count the number of ways in which particular types of configuration can occur on a given lattice.

This latter problem is still one of considerable difficulty, and although many different authors have dealt with it, little attempt seems to have been made to devise systematic methods of enumerating and checking. As a consequence of this, many published results contain errors, and for several important lattices, such as the close-packed cubic, calculations have not been pushed very far.

For the Ising model the cluster sums can be transformed to yield series expansions at low and high temperatures. The evaluation of the cluster sums involves 'spin counts', i.e. a classification and determination of the number of configurations on a given lattice involving a finite number of overturned spins. The high temperature expansions involve 'line counts', i.e. a classification and determination of the number of configurations involving a finite number of lattice bonds.

In the present paper we shall be concerned with high temperature configurations ; these configurations are also of importance for high temperature expansions of more generalized models, such as the Ising model with higher values of spin, and the Heisenberg model. In particular the zero-field solution, and the magnetic susceptibility expansion in zero-field can be expressed in terms of certain irreducible constants, and it is our task to show how these constants can be determined with reliability for various lattices. We shall also demonstrate how certain finite symmetrical clusters can be used to verify our formulae.

§ 2. THE HIGH TEMPERATURE NO-FIELD EXPANSION. WAKEFIELD'S METHOD

If we consider the complete high temperature expansion for the simple Ising model in the presence of a magnetic field, the number of high temperature configurations increases very rapidly with the number of lines. For 1, 2, 3 . . . 6 lines there are 1, 3, 8, 23, 66, 212 distinct configurations. In the absence of a magnetic field very few of these retain a non-zero contribution to the high temperature expansion. If a suitable transformation of variable is employed the partition function can be expressed in the following form (Newell and Montroll 1953)

$$Z_N=2^N(\cosh K)^{Nq/2}\left[1+\sum_r n(r)\tanh^r K\right]. \quad . \quad . \quad . \quad (1)$$

Here $K=J/2kT$, J is the interaction energy of parallel spins, q is the coordination number of the lattice, and $n(r)$ is the number of closed graphs of r lines which can be constructed on the lattice ; only graphs in which an even number of lines meet at each vertex make any contribution. The configurations now required for the first six terms are the following :

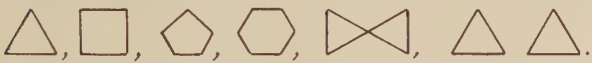

The expansion can be pushed considerably further in this case, and for the simple cubic lattice Wakefield (1951) derived a series up to the 12th term.

Fig. 1

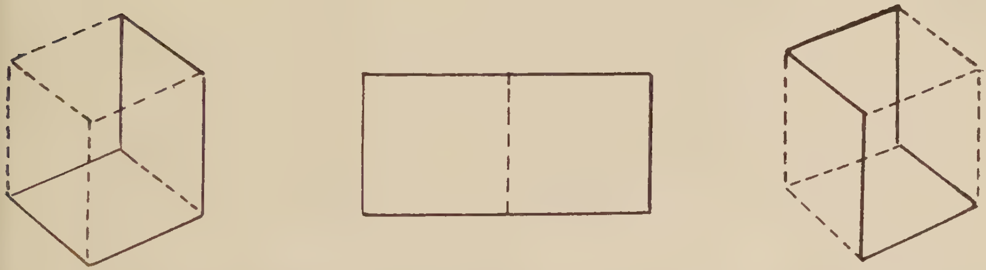

As a simple illustration of the problem of polygon counting let us first consider the number of quadrilaterals on the simple cubic lattice. It is clear that such a structure admits only of quadrilaterals that are plane squares. Through each site of the lattice there pass twelve squares, four in each coordinate plane. We neglect surface effects, assuming that boundaries of the lattice are joined cyclically. The number of distinct squares for a lattice of N points is thus $3N$. When we come to examine the number of hexagons we find that there are three possible space types (fig. 1), and that these can be placed on the lattice in $12N$, $6N$, $4N$ ways respectively. This is the method of division into space types introduced by Wakefield, but the process becomes very laborious after the first few terms ; there are 73 types of decagon, and 756 types of dodecagon.

The chief difficulty, apart from the labour involved, is to ensure that no space types have been overlooked at each stage. For a lattice like the simple cubic it is possible, although laborious, to do this geometrically. We further illustrate the method by listing in Appendix I the 11 types of octagon for this lattice. However for a lattice like the face-centred cubic lattice the method is very cumbersome, and the polygons are more difficult to visualize and draw.

Although we shall in the next section describe an alternative method of counting polygons, the classification of the first few polygons on a lattice into space types is of great use; the space-type technique is also the only one we possess for estimating the value of certain other configurations which arise in series expansions for non-zero field.

§ 3. The Method of Closed Circuit Counting

An alternative method of determining the number of n-sided closed polygons on a lattice depends on the use of an n-step random walk on the lattice. We again illustrate this by the simple example of quadrilaterals on the simple cubic lattice. If we leave the origin along any axis, say Ox, which we may do in six ways, we have after this first step four choices for the next step that will each enable us to return to the origin in one non-self-intersecting path of four steps in all. Thus there are $24N$ possibilities for the whole lattice, and we shall have described every square from each vertex in both directions or eight times. The number of distinct paths is thus $3N$.

In general if u_n is the number of non-self-intersecting random walks of n steps starting and ending at a given lattice point, then the number of distinct polygons is equal to $Nu_n/2n$ $(=Np_n)$. Our problem thus reduces to determining u_n, but this is again a problem of classic difficulty. However, it is quite an easy matter to determine for various lattices the total number, r_n, of random walks of n steps which return to the starting point (see Appendix II). We have also found it possible from this to determine q_n, the total number of random walks which return to the starting point, no immediate reversals being allowed (Appendix III) (this means that two successive steps $\rightleftarrows$ cannot occur, although 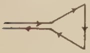 can occur). A similar problem has recently been discussed by Temperley (1956) for the simple quadratic lattice, but our result is more general as it applies to all lattices.

It is now easy to see that for values of $n<6$ only simple polygonal paths are possible, e.g. $n=3$ $n=4$ $n=5$ Thus we find that

$$\left.\begin{aligned} q_3 &= 6p_3 \\ q_4 &= 8p_4 \\ q_5 &= 10p_5 \end{aligned}\right\} \qquad (2)$$

For values of $n>5$ self-intersecting paths will occur. Hence for $n=6$ in addition to a simple hexagonal path, three paths are possible which involve the description of two triangles (fig. 2). The first two correspond to lattice constants of 6 and 5 lines respectively, which we have denoted by p_{6c} and p_{5a}†. The simple hexagon will contribute $12p_6$ paths to q_6; the last configuration, two triangles described successively, will contribute $6p_3$ (the triangles described in the same sense since immediate reversals are not allowed). For p_{6c} there is a choice of paths in accordance with the scheme shown in fig. 3. From the vertices ABDE there will be four ways of describing the configuration (as shown or in the reverse direction), and from the vertex C there will be eight ways; hence the total contribution is $24p_{6c}$. Finally for p_{5a} starting from the vertex A or D the path can be described in two ways (fig. 4 (*a*)) (and reverse direction). Starting from B or C the path can be described in four ways (fig. 4 (*b*)) (and reverse direction). Hence we may deduce that

Fig. 2

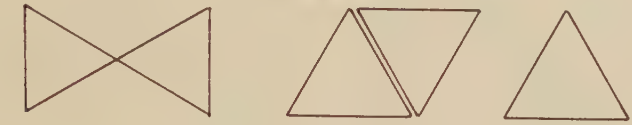

Fig. 3

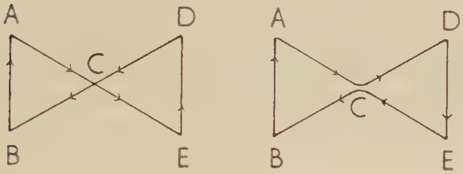

Fig. 4 (*a*)

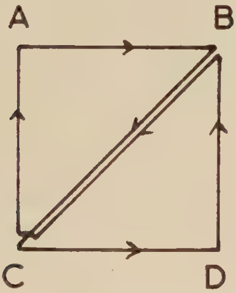

$$q_6 = 12p_6 + 24p_{6c} + 12p_{5a} + 6p_3. \qquad (3)$$

We are thus furnished with a relation between p_6 and other lattice constants such as p_{6c}, p_{5a}. It is convenient to refer to these as reducible lattice constants since they are obtained by putting together two lower order configurations with a common side or vertex ; we shall deal with the calculation of these reducible lattice constants subsequently.

---

† We have found it convenient to regard all closed configurations of n lines as lattice constants. As each new type arises we denote it by a symbol; p_n for a polygon, p_{nx} for any other constant of n lines. All lattice constants are defined per site, so that the total number of distinct configurations is Np_{nx}.

Fig. 4 (*b*)

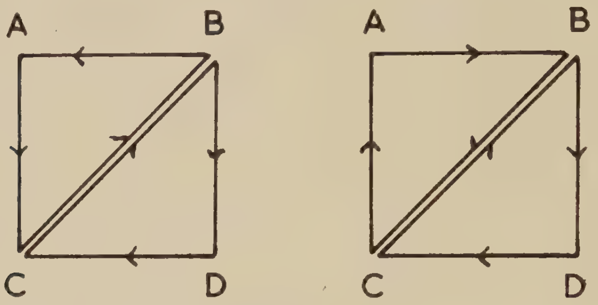

It will be seen that the coefficients of the various constants in the relation (3) can only be obtained directly after a somewhat intricate analysis. We shall show in the next section how finite clusters may be used to provide a substantial check on these coefficients.

§ 4. The Use of Finite Close-Packed Clusters

A close-packed cluster of M spins is a set of M spins in which every spin is connected with every other spin. For 4 spins this corresponds to a tetrahedron, for 6 spins to a hexagon with all bonds connected as shown in fig. 5. Close-packed clusters possess the simplifying feature that every spin is connected to every other in the cluster and hence polygonal counting problems are considerably simplified. Many of the problems of interest for standard lattices can be more easily considered for close-packed clusters, and hence a check can often be obtained on the counting of constants for these lattices.

Fig. 5

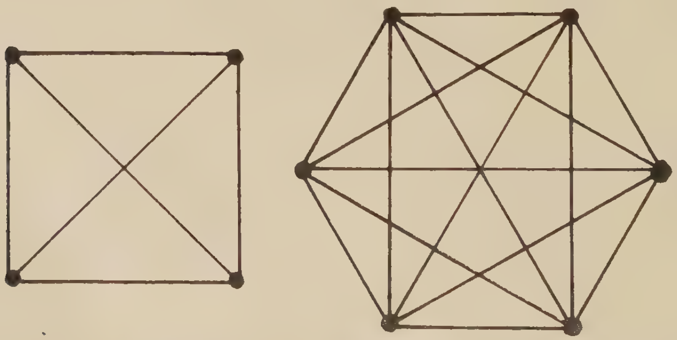

A close-packed cluster of M points has coordination number $(M-1)$ which we denote by $(\sigma+1)$ in accord with our practice for standard lattices; we shall often refer to this cluster briefly as CP(M). The quantities r_n and q_n defined in § 3 can readily be evaluated for finite close-packed clusters, and the derivation is given in Appendix IV. Formulae (24) are polynomials in σ representing the number of paths returning to the origin after n steps for a close-packed cluster of $(\sigma+2)$ points, no immediate reversals being allowed. It is convenient to write these polynomials in the special form:

$$q_n=\alpha_n(\sigma+1)\sigma+\beta_n(\sigma+1)\sigma(\sigma-1)+\gamma_n(\sigma+1)\sigma(\sigma-1)(\sigma-2)+\ldots \quad (4)$$

The number of ways per site of choosing r points on CP(M) is

$$(\sigma+2)(\sigma+1)\ldots(\sigma-r+3)/(\sigma+2)r!,$$

and therefore in (4) the coefficient of α_n is proportional to the number of ways per site of choosing three points on the cluster, the coefficient of β_n is proportional to the number of ways per site of choosing four points on the cluster, the coefficient of γ_n is proportional to the number of ways of choosing five points on the cluster, and so on.

We now refer back to formula (3) of § 3 and note that it is a general formula applying to all lattices and to close-packed clusters. In general we may write

$$q_n=\sum_{\substack{\text{all } p_{sx} \\ s\leqslant n}} \lambda_{s,r}(n)p_{s,r}. \quad \ldots\ldots \quad (5)$$

The λ_{sx} (such as 12, 24, 12, 6 of (3)) may be referred to as path factors. The same lattice constant can occur for different values of n. Thus p_{5a} contributes $12p_{5a}$ to q_6, $28p_{5a}$ to q_7, 0 to q_8 and $36p_{5a}$ to q_9. Hence

$$\left.\begin{array}{ll} \lambda_{5a}(6)=12 & \lambda_6(6)=12 \\ \lambda_{5a}(7)=28 & \lambda_{6c}(6)=24 \\ \lambda_{5a}(8)=0 & \lambda_3(6)=6 \\ \lambda_{5a}(9)=36 & \end{array}\right\} \quad \ldots\ldots \quad (6)$$

Now in the sum represented by (5) there will occur lattice constants with 3, 4, 5 . . . s vertices. If we distinguish them by writing the number of vertices in p_{sx} as a superscript, we have

$$q_n=\sum_{s\leqslant n}\sum_{v=3}^{s} \lambda_{sx}{}^{v}p_{sx}{}^{v}. \quad \ldots\ldots \quad (7)$$

For a close-packed cluster any lattice constant with v vertices is proportional to the number of ways (per site) of choosing v spins in the cluster, i.e.

$$p_{sx}{}^{v}=c_{sx}{}^{v}(\sigma+1)\sigma(\sigma-1)\ldots(\sigma-v+3). \quad \ldots\ldots \quad (8)$$

Here the $c_{sx}{}^{v}$ are pure numbers independent of σ which can easily be determined by the symmetry of the configuration. Thus $c_6{}^6=\frac{1}{12}$ since a polygon can be described in either direction from any of its vertices.

It is not difficult to show for the remaining configurations arising in (3) that $c_{6c}^5=\frac{1}{8}$, $c_{5a}^4=\frac{1}{4}$ and $c_3^3=\frac{1}{6}$.

Thus for a close-packed cluster (7) becomes

$$q_n=\sum_{s\leqslant n}\sum_{v=3}^{s}\lambda_{sx}^{v}c_{sx}^{v}(\sigma+1)\sigma(\sigma-1)\ldots(\sigma-v+3), \qquad (9)$$

and comparing with (4), we find that

$$\left.\begin{array}{l}\displaystyle\sum_{\substack{p_{sx}^3\\ s\leqslant n}}\lambda_{sx}^{3}c_{sx}^{3}=\alpha_n\\[2ex] \displaystyle\sum_{\substack{p_{sx}^4\\ s\leqslant n}}\lambda_{sx}^{4}c_{sx}^{4}=\beta_n\\[2ex] \displaystyle\sum_{\substack{p_{sx}^5\\ s\leqslant n}}\lambda_{sx}^{5}c_{sx}^{5}=\gamma_n\\ \ldots\ldots\ldots\ldots\end{array}\right\} \qquad (10)$$

giving $(n-2)$ relations that must be satisfied by the path factors of q_n. For $n=6$ these relations suffice to determine the path factors uniquely. For $n>6$ there are not sufficient relations to determine the path factors in this way but we obtain $(n-2)$ checks on the validity of the value determined by the direct method. We have been able to derive the path factors in (5) for values of n up to 9.

§ 5. REDUCIBLE LATTICE CONSTANTS

We use the term reducible lattice constants to denote constants which may be constructed by placing together two lower order configurations at one vertex or along one side. Examples of such reducible lattice constants are p_{5a} and p_{6c} referred to in § 3 ; the former arises by placing together two triangles with a side in common and the latter by placing together two triangles with a vertex in common. It should be noted that although we have used the term reducible for these configurations, they may nevertheless be multiply-connected (e.g. p_{5a}).

The method of calculation of such constants is best illustrated by examples, and we shall calculate p_{6c}, p_{5a} in terms of lower order constants. We first note that since there are Np_n simple n-sided polygons on the lattice, and each polygon has n vertices, np_n such polygons pass through any site of the lattice. Similarly, if q is the coordination number of the lattice $(=\sigma+1)$ there are $Nq/2$ bonds in the lattice, and each polygon has n sides ; $2np_n/q$ polygons therefore pass through each bond of the lattice.

We now form p_{6c} 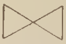 by putting together two triangles at a vertex. We can choose the first triangle in p_3 ways (per site), and the vertex in three ways. We can then choose for the second triangle any of the $3p_3$ triangles passing through this vertex. In doing so we shall describe p_{6c} twice, because of the symmetry with respect to the constituent triangles. But we shall also describe other configurations: thus if the two triangles have two vertices (that is one side) in common we shall obtain p_{5a}; every possible p_{5a} will be described four times, twice from each of the vertices at the end of the diagonal. Finally the triangles may have three vertices in common; we shall then describe every p_3 three times, once from each vertex. Hence we may write

$$9p_3^2=2p_{6c}+4p_{5a}+3p_3. \qquad \ldots\ldots \quad (11)$$

We form p_{5a} by placing two triangles together along a line. The first triangle can be chosen in p_3 ways (per site) and has three sides; having fixed the side, the second triangle can be any of the $6p_3\,q$ triangles passing through this side. We form p_{5a} twice because of the symmetry of the configuration with respect to the triangles, and p_3 three times, once from each side. Hence we have,

$$18p_3^2\,q=2p_{5a}+3p_3. \qquad \ldots\ldots \quad (12)$$

Clearly formulae (11) and (12) suffice to determine p_{6c} and p_{5a} in terms of p_3 and q.

We now observe that relations such as (11) and (12) must also hold for finite close-packed clusters CP(M), for which the values of the constants can be much more readily evaluated (§ 4, eqn. (8)). Hence these finite close-packed clusters can be used as a check on equations such as (11) and (12). It is possible to substitute for the lattice constants the algebraic polynomials in σ given by (8) and to check both sides algebraically. However, it is usually more convenient to employ numerical checks since if M is sufficiently large all the configurations occur on CP(M). Thus for CP(5) $p_{5a}=6$, $p_{6c}=3$, $p_3=2$ and it is easily verified that the relations (11) and (12) are satisfied.

§ 6. IRREDUCIBLE LATTICE CONSTANTS

Any constants which cannot be expressed in terms of lower order configurations we refer to as irreducible. The most important class of irreducible constants are the simple polygons. After this we must deal with constants involving a double bridge, such as p_{6a}, p_{7f}, p_{8c} shown in fig. 6. These can be counted by the space type method, but it is somewhat simpler to use a modified circuit counting technique. The simple polygons

Fig. 6

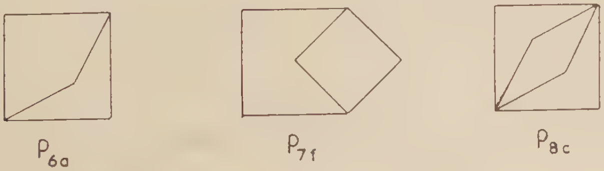

which form the framework of the configuration must be classified into different space types, and for each type we must count the number of sites adjacent to the pair which are at the end of the double bridge. We illustrate by obtaining the value of p_{6a} for the face-centred cubic lattice.

Fig. 7

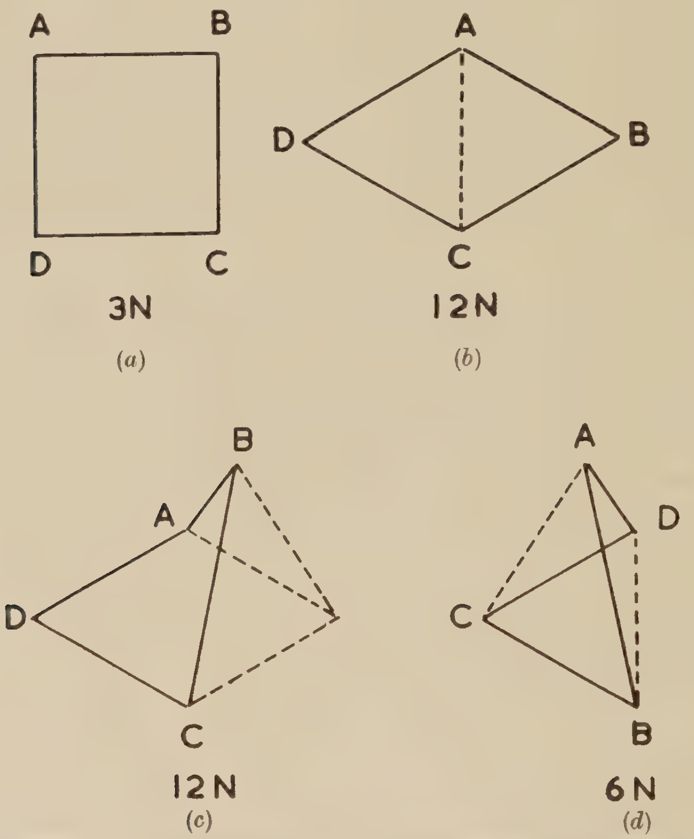

(*a*) Flat square. (*b*) Flat diamond. (*c*) Obtuse diamond. (*d*) Acute diamond.

For this lattice there are four different types of quadrilateral which occur $3N$, $12N$, $12N$, $6N$ times respectively (fig. 7). For type (*a*) there are four double bridges two each from AC, BD. For type (*b*) there are two double bridges from AC. For types (*c*) and (*d*) there are four double bridges two each from AC, BD. (This can only be seen properly with the aid of a model.) Hence we have a total of $108N$ types. But in carrying out this procedure we have counted each p_{6a} exactly three times since each of the three double links can equally well be regarded as the double bridge, and the remaining pair of double links as the basic quadrilateral. Thus p_{6a} is equal to 36.

When all the irreducible lattice constants of a given order have been determined the analysis of q_n provided by an equation such as (3) enables us to check the determination. Thus we have been able to obtain the following three relations to follow (2):

$$\left.\begin{aligned} p_6 &= \tfrac{1}{12}[q_6-4q_3-3q_3^2(1-3/q)] \\ p_7 &= \tfrac{1}{14}[q_7+7q_3(q_3/q-1)(q_3/q-3)-7q_3q_4(1-3/q)] \\ p_8+3p_{6a}-6p_{8c}-33p_{6d} &= \tfrac{1}{16}[q_8-5q_4-80q_3 \\ &\quad -4(q_4^2+2q_3q_5)(1-3/q)+8q_3^2(3q_4-8q_3)/q^2 \\ &\quad +32q_3(4q_3-q_4)/q-4q_3^2(q-4)] \quad (q=\sigma+1) \end{aligned}\right\} \quad . \quad (13)$$

§ 7. General Conclusions

Our main purpose in the present paper has been to indicate methods of evaluating and checking lattice constant determinations which arise in crystal statistics. The same constants enter in a variety of problems connected with cooperative phenomena, and it has seemed worth while devoting attention specifically to their determination. An analysis of previous results of even the most careful workers has revealed discrepancies and errors, and we have therefore concentrated particularly on checking our results. It is perhaps too much to expect that all sources of error have been removed in so complex a problem, but we hope that at least a substantial number have been eliminated.

We hope elsewhere to publish fuller details of the evaluation of higher order lattice constants, and tables of the constants which we have succeeded in determining. We wish here to summarize the results of our investigation, and to quote some of the series expansions which have been derived from them. Thus for the expansion of the partition function of the Ising model quoted in (1) we may write:

$$\left.\begin{aligned} n(3) &= Np_3 \\ n(4) &= Np_4 \\ n(5) &= Np_5 \\ n(6) &= \tfrac{1}{2}N^2p_3^2-N(p_{5a}+\tfrac{1}{2}p_3-p_6) \\ n(7) &= N^2p_3p_4-N(2p_{7g}+p_{6b}+2p_{5a}-p_7) \end{aligned}\right\} \quad . \quad . \quad . \quad (14)$$

and we have derived $n(8)$, $n(9)$ for a general lattice. For a loose-packed lattice many configurations do not enter and we have obtained $n(10)$.

For the initial susceptibility of the Ising model at high temperatures we may write

$$\chi_0 = \frac{Nm^2}{kT}(1-\sigma v)^{-2}\left[1-(\sigma-1)v-\sigma v^2+\sum_{3}^{\infty} c_r v^r\right] \quad . \quad . \quad . \quad (15)$$

Constant		Lattice constants						
		Simple quadratic	Simple cubic	Body-centred cubic	Tri-angular	Face-centred cubic	CP(5)	CP(6)
$\sigma=q-1$		3	5	7	5	11	3	4
p_3†	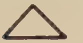	0	0	0	2	8	2	10/3
p_4†	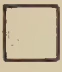	1	3	12	3	33	3	15/2
p_5†	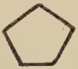	0	0	0	6	168	12/5	12
p_{5a}	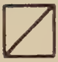	0	0	0	3	36	6	15
p_6†	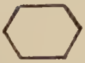	2	22	148	15	970	0	10
p_{6a}†	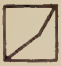	0	0	12	0	36	2	10
p_{6b}	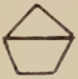	0	0	0	12	384	12	60
p_{6c}	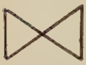	0	0	0	9	204	3	15
p_{6d}†	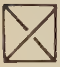	0	0	0	0	2	1	5/2
p_7†	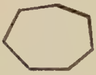	0	0	0	42	6168	0	0
p_{7a}	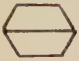	2	18	192	12	966	0	30
p_{7b}	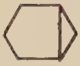	0	0	0	30	2400	0	60
p_{7c}	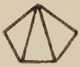	0	0	0	6	192	12	60
p_{7d}	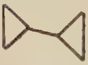	0	0	0	42	2196	0	15
p_{7e}	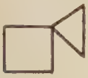	0	0	0	30	2040	0	30
p_{7f}†	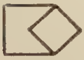	0	0	0	0	600	0	30
p_{7g}	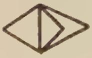	0	0	0	0	24	2	10
p_{7h}†	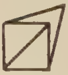	0	0	0	0	48	6	30

† Irreducible.

where m is the magnetic moment of a single spin, $v=\tanh K$, and the c_r are independent of σ. We then find that

$$\left.\begin{aligned}
c_3 &= -6p_3\\
c_4 &= -8p_4\\
c_5 &= 6p_3-10p_5+8p_{5a}\\
c_6 &= 6p_3+8p_4-12p_6+28p_{5a}+8(p_{6a}+p_{6b}+p_{6c})\\
c_7 &= 10p_5-14p_7+36p_{5a}+16p_{6a}+30p_{6b}+16p_{6c}\\
&\qquad +8(p_{7a}+p_{7b}+p_{7c}+p_{7d}+p_{7e}+p_{7f})+44p_{7g}
\end{aligned}\right\} \quad . \quad . \quad (16)$$

We have also derived c_8 for a general lattice and c_9 for a loose-packed lattice. Expansions of this type for the Heisenberg model have been given by Rushbrooke and Wood (1955); the same constants enter, as indeed they must for all lattice models of this kind. The detailed physical conclusions to be drawn from these susceptibility expansions have been discussed elsewhere (Domb and Sykes 1957). The lattice constants corresponding to seven lines and less are presented in the table for a number of lattices.

Finally, we quote series expansions for the partition function per spin for the simple cubic, body-centred cubic and face-centred cubic lattices, which are derived by taking the Nth root of Z_N in (1) and correspond formally to putting $N=1$ in (14):

$$\left.\begin{aligned}
&\text{Simple cubic}\\
&Z=2(\cosh K)^3[1+3v^4+22v^6+192v^8+2046v^{10}+24\,861v^{12}\ldots]\\
&\text{Body-centred cubic}\\
&Z=2(\cosh K)^4[1+12v^4+148v^6+2568v^8+53\,944v^{10}+\ldots]\\
&\text{Face-centred cubic}\\
&Z=2(\cosh K)^6[1+8v^3+33v^4+168v^5+962v^6+5928v^7+38\,907v^8\\
&\qquad\qquad +268\,056v^9+\ldots]
\end{aligned}\right\} \quad . \quad (17)$$

The coefficient of v^{10} for the simple cubic lattice differs from those of Wakefield (1951) and Trefftz (1950) who both give 2070; the coefficient of v^{12} differs from that of Wakefield who gives 24 943 (Rushbrooke 1952). However we have discussed this point privately with Wakefield who agrees that some of his space types were counted wrongly. The term in v^{10} for the body-centred cubic lattice is new, as are the terms in v^8 and v^9 for the face-centred cubic lattice. The discussion of the physical conclusions to be drawn from the expansions (17) is deferred to another paper.

APPENDIX I

Octagons on the simple cubic lattice (after Wakefield). (11 types. Total contribution $207N$. $p_8=207$.)

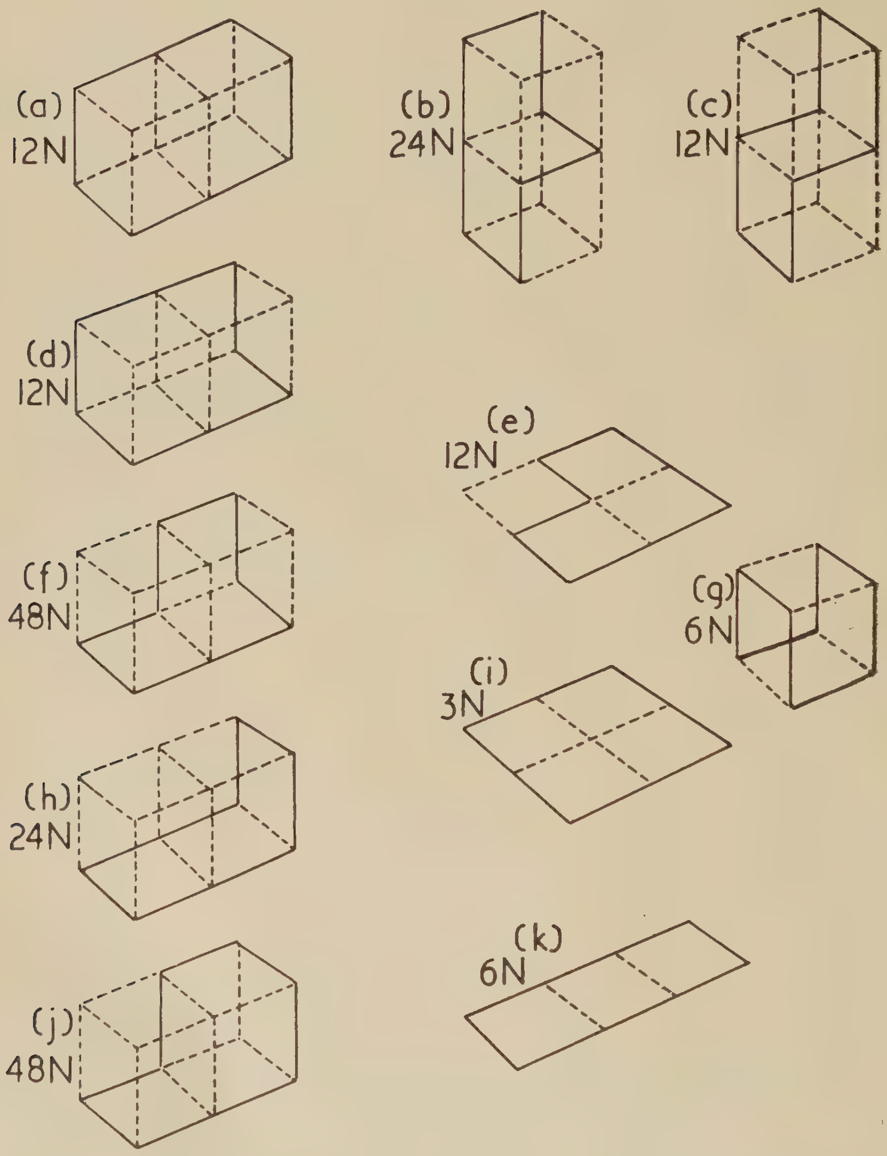

APPENDIX II

The Number of Returns to the Origin after n Steps of a Random Walk

This problem has been considered in detail elsewhere (e.g. Domb 1954). To each particular lattice corresponds a generating function $\phi(x, y, z)$, and the number of returns to the origin after n steps is given by the coefficient independent of x, y, z in $[\phi(x, y, z)]^n$. The generating functions for the simple well-known lattices and corresponding values of r_n are as follows:

$$\left.\begin{array}{l}
\text{Simple quadratic} \\
\phi=\frac{1}{4}(x^{-1}+x+y^{-1}+y), \\
r_n=(n\,!)^2/[(\frac{1}{2}n)\,!]^4 \quad (n \text{ even}). \\
\text{Triangular} \\
\phi=\frac{1}{6}(x^{-1}+x+y^{-1}+y+xy^{-1}+x^{-1}y), \\
r_n=\sum\limits_{s,\,t}\dfrac{1}{s\,!\;t\,!}\sum\limits_{q=0}^{s}2^{s-q}\dfrac{(t+q)\,!}{[(t+q)/2\,!]^2}\dfrac{1}{q\,!\,(s-q)\,!}. \\
s, t=0, 1 \ldots n\,; \quad (2s+t)=n\,; \qquad (t+q) \text{ even}. \\
\text{Simple cubic} \\
\phi=\frac{1}{6}(x^{-1}+x+y^{-1}+y+z^{-1}+z). \\
r_n=\sum\limits_{r,\,s,\,t}\dfrac{n\,!}{(r\,!)^2\,(s\,!)^2\,(t\,!)^2},\, r, s, t=0, 1 \ldots \nu, r+s+t=\nu, n=2\nu \text{ (even)}. \\
\text{Body-centred cubic} \\
\phi=\frac{1}{8}(x^{-1}+x)(y^{-1}+y)(z^{-1}+z). \\
r_n=(n\,!)^3/\{(\frac{1}{2}n)\,!\}^6 \quad (n \text{ even}). \\
\text{Face-centred cubic} \\
\phi=\frac{1}{12}[(y^{-1}+y)(z^{-1}+z)+(z^{-1}+z)(x^{-1}+x)+(x^{-1}+x)(y^{-1}+y)]. \\
r_n=\sum\limits_{r,\,s,\,t}\dfrac{n\,!}{r\,!\;s\,!\;t\,!}\dfrac{(r+s)\,!}{[(\frac{1}{2}(r+s))\,!]^2}\dfrac{(s+t)\,!}{[(\frac{1}{2}(s+t))\,!]^2}\dfrac{(r+t)\,!}{[(\frac{1}{2}(r+t))\,!]^2},\, r+s+t=n. \\
\qquad r, s, t=0, 1 \ldots n, \qquad r, s, t \text{ all odd or all even}.
\end{array}\right\} \quad (18)$$

APPENDIX III

Random Walk with no Immediate Reversals

We have been able to derive the following general formula for q_n in terms of r_n for any lattice of coordination number $(\sigma+1)$ $(r_0=1)$,

$$\begin{aligned} q_n=\frac{\sigma-1}{2}[(1)^n+(-1)^n]+r_n-\sigma n r_{n-2}+\sigma^2\frac{n(n-3)}{2\,!}r_{n-4} \\ -\sigma^3\frac{n(n-4)(n-5)}{3\,!}r_{n-6}+\sigma^4\frac{n(n-5)(n-6)(n-7)}{4\,!}r_{n-8}+\ldots \end{aligned} \quad (19)$$

There are two independent methods of establishing this formula. The first and most obvious is to treat the random walk with no immediate reversals as a Markoff process. The generating matrix for a simple quadratic lattice, for example, is:

$$A=\left|\begin{array}{cccc} x & 0 & x & x \\ 0 & x^{-1} & x^{-1} & x^{-1} \\ y & y & y & 0 \\ y^{-1} & y^{-1} & 0 & y^{-1} \end{array}\right| \quad \ldots\ldots \quad (20)$$

and q_n is the coefficient independent of x, y in spur (A^n). It is easy to establish that formula (19) holds in this case, and the method is similar to that used by Temperley (1956). However, for a lattice such as the face-centred cubic a matrix of order 12 needs to be considered, and although the method can be followed through it is quite involved. In any case since only the coordination number enters into formula (19) it should be possible to establish it by a method which is simultaneously valid for all lattices.

An alternative approach was therefore put forward as follows. In any random walk on a lattice starting at the origin let $r_n(a, b, c)$ represent the number of paths in which the walker is at (a, b, c) after n steps, and let $q_n(a, b, c)$ represent the corresponding number in a walk with no immediate reversals. Then $r_n(a, b, c)$ can be divided into mutually exclusive classes in which the first reversal $\leftrightarrows$ occurs after r steps; each particular class thus consists of the first r steps with no reversal, then a reversal which can occur in σ ways and then the remaining $(n-r-2)$ steps of an ordinary random walk. Hence we may write:

$$\begin{aligned} r_n(a, b, c) = q_n(a, b, c) + \sigma q_{n-2}(a, b, c) + \sigma \sum_{a'b'c'} q_{n-3}(a', b', c') r_1(a'', b'', c'') \\ + \sigma \sum_{a'b'c'} q_{n-4}(a', b', c') r_2(a'', b'', c'') \\ + \dots \sigma \sum_{a'b'c'} q_1(a', b', c') r_{n-3}(a'', b'', c'') \\ + (\sigma+1) r_{n-2}(a, b, c), \quad . \quad . \quad (21) \end{aligned}$$

$$\left. \begin{aligned} a'+a''&=a \\ b'+b''&=b \\ c'+c''&=c \end{aligned} \right\}.$$

Introducing generating functions:

$$R_n(x, y, z) = \sum_{a, b, c,} r_n(a, b, c) x^a y^b z^c$$

$$Q_n(x, y, z) = \sum_{a, b, c,} q_n(a, b, c) x^a y^b z^c$$

we find that (21) leads to

$$R_n = Q_n + \sigma\{Q_{n-2}R_0 + Q_{n-3}R_1 + \dots + Q_1 R_{n-3}\} + (\sigma+1)R_{n-2} \qquad (22)$$

and hence we can solve for Q_n in terms of R_n. Further details of the method (which has been developed in conjunction with M. E. Fisher) will be published elsewhere.

APPENDIX IV

Random Walk on a Close-Packed Cluster

Select one point as origin O and suppose a random walk is started at O. Then at each stage there are $(\sigma+1)$ possibilities, and the total number of paths after n steps is $(\sigma+1)^n$. Of these the number at O is by definition r_n. Since the cluster is perfectly symmetric in regard to the constituent points, the number of arrivals at each of the $(\sigma+1)$ other points must be

$$[(\sigma+1)^n-r_n]/(\sigma+1). \qquad (23)$$

If now one more step is taken the number of arrivals at O will be $(\sigma+1)$ times the expression (23), and this is by definition r_{n+1}. Thus

$$r_{n+1}=(\sigma+1)^n-r_n$$

and hence the r_n can readily be determined as polynomials in σ.

The second method of Appendix III can be adapted to apply to close-packed clusters. Hence using formula (19) the q_n can readily be determined as polynomials in σ. The first few polynomials are as follows :

$$\left.\begin{aligned} q_1&=0\\ q_2&=0\\ q_3&=\sigma(\sigma+1)\\ q_4&=\sigma(\sigma+1)(\sigma-1)\\ q_5&=\sigma(\sigma+1)(\sigma^2-3\sigma+2)\\ q_6&=\sigma(\sigma+1)(\sigma^3-3\sigma^2+5\sigma-2)\\ q_7&=\sigma(\sigma+1)(\sigma^4-3\sigma^3+7\sigma^2-8\sigma+3)\end{aligned}\right\} \qquad (24)$$

ACKNOWLEDGMENT

We are grateful to Dr. A. J. Wakefield for helpful correspondence.

REFERENCES

DOMB, C., 1954, *Proc. Camb. Phil. Soc.*, **50,** 586.
DOMB, C., and SYKES, M. F., 1957, *Proc. Roy. Soc.* A (in the press).
FUCHS, K., 1942, *Proc. Roy. Soc.* A, **179,** 340.
MAYER, J. E., and MAYER, M. G., 1940, *Statistical Mechanics* (New York : John Wiley and Sons).
NEWELL, G. F., and MONTROLL, E. W., 1953, *Rev. Mod. Phys.*, **25,** 353.
RIDDELL, R. J., 1951, *Thesis*, University of Michigan.
RIDDELL, R. J., and UHLENBECK, G. E., 1953, *J. Chem. Phys.*, **21,** 2056.
RUSHBROOKE, G. S., 1952, *Changements de Phases* (Paris : Société de Chimie Physique), p. 177.
RUSHBROOKE, G. S., and WOOD, P. J., 1955, *Proc. Phys. Soc.* A, **68,** 1161.
TEMPERLEY, H. N. V., 1956, *Phys. Rev.*, **103,** 1.
TREFFTZ, E., 1950, *Z. Phys.*, **127,** 371.
WAKEFIELD, A. J., 1951, *Proc. Camb. Phil. Soc.*, **47,** 419.
YANG, C. N., and LEE, T. D., 1952, *Phys. Rev.*, **87,** 404.

The Initial Stages of Growth of Thin Metal Films on a Silver Single-Crystal Substrate†

By R. C. Newman
Department of Physics, Imperial College, London, S.W.7‡

[Received March 15, 1957]

Abstract

Very thin layers of several metals have been deposited onto smooth (111) surfaces of silver single crystals. The initial stages of growth of these deposits were followed by electron diffraction. Lead, thallium and silver grew in the form of oriented monolayers, while three-dimensional crystallites of gold and nickel were found in the earliest detectable stages. Thin deposits up to about 8 Å of both tin and antimony possessed an amorphous structure only. Spontaneous crystallization of these films was observed and thicker films were wholly crystalline. In several cases a proportion of randomly oriented deposit was formed which predominated when the thickness of the film was increased. This shows the importance of examining the initial stages of the process. No evidence for pseudomorphic growth was observed.

§ 1. Introduction

Many results are now available on the structure of thin films deposited on single-crystal substrates. Such deposits are often oriented relative to the substrate ; a comprehensive review of these epitaxial growths has recently been given by Pashley (1956). In very few of the experiments, however, have deposits of less than 5 Å in mean thickness been examined, and information concerning the earliest stages in the formation of an oriented overgrowth has not been obtained. In most cases it is not known whether the first atoms to arrive on the substrate spread over the surface to form an oriented monolayer, or whether they coalesce to form three-dimensional crystallites. It is important to obtain such information, so that in any theory of oriented overgrowths a model is used which is in agreement with the experimental observations.

To make these observations, it is necessary to perform experiments under highly controlled conditions, and to record the growth of the deposit continuously in the range of thicknesses from 0 to 5 Å. The evaporation technique for producing the deposit on the substrate *in situ* in an electron diffraction camera is the best way to obtain a controlled rate of deposition, and the growth of the film can then be followed from changes in the diffraction pattern ; apparatus built for this purpose has already been described by Kehoe *et al.* (1954, 1955). The growth of copper deposits on silver single crystals has been studied in this way, and radioactive copper was used to determine the thickness of the deposits (Newman and Pashley 1955). It was found that a surface film with a mean thickness equal to that of a monomolecular layer, deposited on a flat substrate surface, was easily detectable by electron diffraction. In fact the thinnest layer of copper which gave rise to a distinct diffraction pattern was only 0·8 Å in mean thickness. The copper formed small oriented crystallites about 12 Å in height and 60 Å in width, even in the earliest stages of growth ; there was no evidence for the formation of a monolayer as would be required in the theory of Frank and Van der Merwe (1949 a, b).

---

† Communicated by Dr. M. Blackman.

‡ Now at Research Laboratory, Associated Electrical Industries, Ltd., Aldermaston Court, Aldermaston, Berkshire.

The purpose of the present work is to extend these observations to the initial stages of growth of other metal deposits. Silver single crystals, prepared by evaporation onto heated mica, have again been used as the substrates. These specimens possess surfaces which are essentially smooth on an atomic scale, which gives the optimum condition for the observation of the deposits. In addition, no difficulty is experienced due to charging of the specimens in the electron beam, as in the case of non-conducting crystals. The growth of thin films of several metals deposited at a rate of 1 to 10 Å/min onto these substrates has been examined in detail.

§ 2. EXPERIMENTAL TECHNIQUES

All evaporations were carried out in the diffraction camera at a pressure of better than 10^{-4} mm Hg. Most metals were evaporated from either tungsten or molybdenum wire spirals, although lead and thallium were evaporated from a nickel wire (see Caldwell 1941). At the low rates of deposition which were used, there was no appreciable heating of the silver substrates which were at room temperature in all cases.

Several methods were used to estimate the thickness of the deposits. The average rate of evaporation was calculated from the time required to evaporate a known mass of the metal. The rate of deposition could only be obtained from this value if it was assumed that there was no re-evaporation from the surface of the silver substrates, as discussed by Frenkel (1923). In addition, the diffraction patterns from the deposits were compared with those obtained from copper deposits and silver bromide overgrowths in experiments where radioactive tracers were used to measure the average thickness directly (see Newman and Pashley 1955). This comparison technique has one serious disadvantage. If the initial layers of a deposit formed a pseudomorphic overgrowth, it would be almost impossible to detect whether the layer had in fact formed, since there would be little or no change from the original substrate diffraction pattern. In order to overcome this difficulty, another technique was employed. A cleaved rocksalt specimen was mounted next to the silver substrate on the specimen holder and thus deposits of approximately equal thickness were formed on both surfaces. The deposit formed on the rocksalt could be examined at any time by a simple deflection of the electron beam from the silver crystal. The rate of deposition could be calibrated in the following way. It has been found that a layer of copper 2 Å in thickness, deposited onto rocksalt at room temperature, gave rise to an observable ring pattern on the fluorescent screen (see Newman 1955). The limiting thickness for any other metal to give a similar pattern was calculated from the difference in scattering power between the metal and copper. The rate of deposition onto the silver specimen in the initial stages was thus found from the time taken before a ring pattern became visible from the same thickness of deposit on the rocksalt sample. This technique was particularly valuable in the case of silver and gold deposits because the diffraction patterns from these films were coincident with that of the substrate.

The methods of thickness estimation described above are obviously far less accurate than the radioactive tracer technique. The accuracy of the present measurements is not, however, considered to be in error by more than ±50%

Estimates of the size of crystallites of the deposits were made from the width and height of the diffraction spots and the usual reservations apply to the values given (see Pinsker 1953, p. 201).

§ 3. RESULTS

3.1. *Lead*

The presence of a lead deposit was first detected in the diffraction pattern by the gradual appearance of continuous streaks of intensity inside the streaked spots due to the silver substrate. (A diffraction pattern from a typical silver specimen has already been published—see Newman and Pashley 1955.) The orientation was (111) lead parallel to (111) silver with [110] lead parallel to [110] silver. These effects were observed when the mean thickness of the deposit was less than 1 Å. As the thickness was increased up to about 3 to 4 Å, these streaks became much more intense, but retained their continuous nature perpendicular to the surface, even when the specimen was viewed at different angles of incidence in the electron beam. In addition, extra weaker streaks appeared due to double scattering via the silver substrate. A typical pattern is shown in fig. 1 (Plate), in which the streaks about the centre line of spots are due to the double scattering process.

Since no intensity changes could be seen along the length of the streaks, it was concluded that the lead had formed a monomolecular layer on the silver surface. If the lateral dimensions of this layer had been large, the streaks would have been exceedingly sharp, but measurements of the width of the streaks corresponded to a crystal size of 80 Å. The deposit is thus thought to be in the form of islands of monolayer. The lattice spacing of these deposits was determined relative to the silver base and a value of the closest distance of approach of $a_1=3{\cdot}42\pm0{\cdot}02$ Å was obtained from measurements on seven plates. This value would correspond to a cube length of $a_0=4{\cdot}84\pm0{\cdot}03$ Å which is about 2% smaller than the x-ray value of 4·92 Å. A contraction of this order may be explained by the fact that, in a monolayer structure, the coordination number is only six instead of the usual value of twelve in a three-dimensional lattice. There was no evidence to suggest that the lead had the same lattice constant as the silver in the earliest stages of growth of the layer.

As the thickness of the deposit was increased beyond 3 to 4 Å, variations in intensity appeared along the formerly continuous streaks. Gradually, definite spots were resolved, although they were still linked by streaks. The spot pattern indicated that equal amounts of lead were oriented with $[1\bar{1}0]$ and $[\bar{1}10]$ directions parallel to the silver $[1\bar{1}0]$ direction (this parallel and anti-parallel orientation will hereafter be termed double positioning). In addition, rings due to randomly oriented lead were observed. When the thickness was increased to about 6 Å, the pattern from the silver was almost completely obscured as shown in fig. 2 (Plate). An unusual feature of this pattern is that the regions of greatest intensity on the side diffraction streaks and spots occur at increasing distances from the shadow edge with increasing distance from centre line. A tentative explanation may be that the lead is not oriented strictly parallel to the silver but that there are two orientations such that the lead [110] and $[\bar{1}10]$ directions make small positive and negative angles with the silver $[1\bar{1}0]$ direction. This would lead to two diffraction patterns each slightly off azimuth with respect to the original silver pattern which was set accurately before deposition was started. The composite pattern would then be expected to resemble that shown in fig. 2 (Plate).

Lead was deposited further until the mean thickness of the layer was about 60 to 100 Å. These layers gave rise to diffraction patterns which showed sharp spots due to lead in double positioning and a sharp set of rings due to randomly oriented lead. There were also extra faint spots due to twinning on {111} planes. The height and width of the diffraction spots indicated a crystallite height of about 40 Å and a width of 80 Å, while the width of the rings corresponded to crystallites of about 100 Å in diameter. These values probably represent only lower limits due to the lack of penetration of the electron beam into the crystallites because of the high scattering power of lead.

These results were obtained with a rate of deposition of about 10 Å/min. If a rate of only 1 Å/min was used, the patterns became indistinct due to a high background intensity, and no three-dimensional crystallites formed in the later stages of growth of the deposit. These effects were thought to be due to oxidation or attack of the lead by the residual oxygen and water vapour in the vacuum atmosphere.

3.2. *Thallium*

Metallic thallium resembles lead in many of its physical properties, and it was found that the growth of a thallium film was closely analogous with that of the lead deposits described above. Thallium has a close-packed hexagonal structure and thin layers again gave rise to streak patterns with (001) thallium parallel to (111) silver and [100] thallium parallel to [110] silver, as shown in fig. 3 (Plate). It was found that the secondary diffraction pattern was much stronger than that which was observed from the lead films, but no satisfactory explanation for this is known. From the width of the primary streaks it was concluded that the deposit had formed islands of monolayer growth about 60 Å in diameter. The closest distance of approach was measured relative to the silver and a value of $a=3{\cdot}31\pm0{\cdot}02$ Å was obtained. This is about 4% lower than the value of $a=3{\cdot}45$ Å found for bulk thallium by x-rays. This contraction is of the same order as that found in the very thin lead deposits.

As the thickness was increased beyond about 4 Å, discrete spots became visible on the streaks, and rings due to hexagonal thallium appeared. When the thickness was increased up to about 100 Å, a sharp pattern of slightly arced spots, together with sharp rings, was obtained. It was impossible to estimate the width of the oriented crystallites due to the arcing, which amounted to about ±3° of disorientation. The width of the rings corresponded to a crystal size of about 100 Å.

The above results were obtained with a rate of deposition of about 10 Å/min, since at lower rates there was a deterioration of the diffraction patterns, presumably due to oxidation of the thallium.

3.3. *Tin*

The results for tin were quite different from those described for lead and thallium. As the thickness of the deposit was increased, the pattern from the silver substrate weakened and two very diffuse haloes became visible, indicating that the deposit had an amorphous structure. The silver pattern gradually disappeared and then, quite suddenly, spots appeared along the centre diffraction line, as shown in fig. 4 (Plate), when the thickness of tin was about 7 to 8 Å. Deposits greater than 10 Å in mean thickness gave rise to a sharp pattern of spots and rings as shown in fig. 5 (Plate), and the broad haloes, which can be seen in fig. 4 (Plate), completely disappeared. This sequence of patterns indicates that the amorphous layer of tin suddenly crystallizes at a critical thickness into both oriented and random crystallites. The sharpness of the spots and rings indicates a particle size of at least 200 Å.

The ring pattern was due to white tin which possesses a tetragonal structure with $a=5{\cdot}82$ Å and $c=3{\cdot}17$ Å and where the structure amplitude factor is given by

$$S=\{1+\exp(\pi i\Sigma h)\}[1+\exp\{\pi i(h_2+h_3/2)\}].$$

An analysis of the spot patterns showed that there were three equivalent orientations of the tin, i.e. (100) tin parallel to (111) silver and [010] tin parallel to any of the three equivalent ⟨110⟩ silver directions. The positions of the tin atoms relative to the substrate is shown diagrammatically in fig. 6. It is seen that there is only a small misfit along the [1$\bar{1}$0] silver direction, since the distance between silver atoms is 2·89 Å, which is almost half the distance between the tin atoms of 5·82 Å. In addition, there is an almost perfect angular fit since the [011] tin direction makes an angle of 28° 15′ with the [1$\bar{1}$0] silver direction, and hence is almost coincident with the [2$\bar{1}\bar{1}$] silver direction. The relative misfit along the [001] tin direction is, however, −36%.

Fig. 6

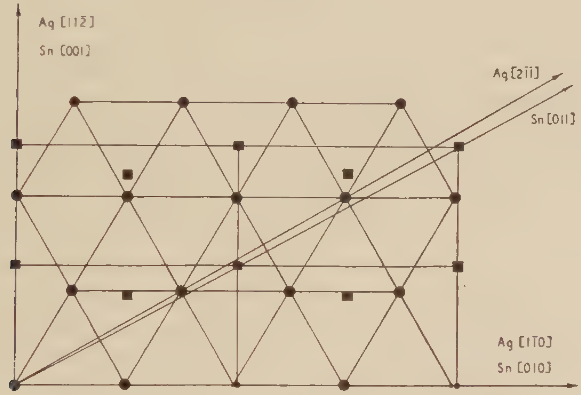

● Silver atoms. ▬ Tin atoms.

The arrangement of tin atoms relative to the substrate silver atoms.

There were also some spots on the centre diffraction line due to the orientation (110) tin parallel to (111) silver; it was not possible to determine whether there was any azimuthal orientation as there were no other associated strong spots. It is interesting to note that this was the orientation which predominated immediately after the transition from amorphous to crystalline tin, although the reason for this is not understood.

3.4. *Silver*

Deposits up to 50 Å in average thickness produced no change from the original substrate diffraction pattern, i.e. the orientation of the substrate was continued in the deposit, the surface remained smooth on an atomic scale (the diffraction spots still showed refraction), and the prominent Kikuchi pattern remained quite clear as shown in fig. 7 (Plate). As the thickness was increased beyond 50 Å, some randomly oriented silver was formed and the Kikuchi pattern became much fainter. Eventually the Kikuchi pattern disappeared completely and the proportion of randomly oriented silver increased until it predominated, the size of the crystallites being about 50 Å.

3.5. *Gold*

Thin layers up to about 8 Å in thickness were oriented in double positioning, it being quite easy to detect a marked change in the diffraction patterns, even though the pattern from the gold was superposed on that of the silver substrate. The refraction effects due to the flat surface of the silver disappeared and the diffraction spots became much broader. The width and height of the gold crystallites were estimated to be about 40 Å and 20 Å respectively.

When the thickness was increased beyond 8 Å, broad rings due to randomly oriented gold appeared in the pattern and the Kikuchi pattern from the silver disappeared. Thicker layers gave rise to a ring pattern only, the sharpness of the rings increasing somewhat as the deposit built up. Measurements showed an increase in crystal size from 20 Å to about 40 Å.

3.6. *Nickel*

The experiments with nickel were not very satisfactory, since the molten bead of metal attacked the tungsten evaporator filament, causing it to burn out. Sufficient control over the rate of deposition was not therefore obtained, and the amount of tungsten evaporated with the nickel may have been quite appreciable (see Heavens 1952).

Oriented deposits showing double positioning were obtained however up to a mean thickness of about 2 to 3 Å. The size of the crystallites was only about 25 Å, and hence accurate measurements of the lattice constant were difficult to make because of the broadening of the spots. A value equal to that of bulk nickel was obtained but the error was at least ±2%.

Thicker deposits showed only randomly oriented nickel with a small crystal size.

3.7. *Antimony*

Deposits of only a few angstroms in mean thickness had the amorphous structure similar to that found by Richter (1943), and Pinsker (1953, p. 244). The next stage in the growth of the deposit was noted when strong well-defined spots appeared on the centre diffraction line, as shown in fig. 8 (Plate). There were only very faint spots visible in other positions, and hence it must be concluded that there was a regular packing of layers of deposit atoms on the surface, but that there was little regular structure in each layer. As the thickness was increased still further, an extensive spot pattern appeared and the broad rings due to the amorphous antimony completely disappeared, as shown in fig. 9 (Plate). The spot pattern was independent of the azimuth setting apart from some very slight intensity changes, showing that the crystallized antimony had a fibrous orientation with the pseudo-cube plane ((110) in the rhombohedral system) parallel to the silver (111) plane. This orientation is similar to that found by Geiling and Richter

(1949) for arsenic deposits on an amorphous base. The size of the antimony crystallites was estimated to be 25 Å high and 40 Å wide. Further experiments revealed that the fibre axis was not influenced by the angular position of the evaporator relative to the silver surface, as has been found in some cases (see Schulz 1949).

3.8. *Other Metals*

Of the metals examined, germanium and silicon formed only amorphous deposits, which is in accord with the work of Collins and Heavens (1952), and Hass (1948). Deposits of tellurium were completely amorphous in very thin layers but became partially crystalline as the thickness was increased (see Sakurai and Munesue 1952). Bismuth deposits were fibrously oriented with both the (110) and (211) planes (rhombohedral system), in contact with the silver (111) plane: there was also randomly oriented material present. Deposits of aluminium, cobalt, chromium, iron, maganese and palladium were all randomly oriented, the particle size being about 20 Å in all cases. Zinc and cadmium would not condense on the silver substrates even when high rates of evaporation were used. Similar effects have been found for these metals by other workers (see Cockcroft 1928 and Ehlers 1953).

§ 4. DISCUSSION

The present experiments provide useful information about the initial stages in the formation of oriented overgrowths and indicate that either the type of growth mechanism proposed by Frenkel (1923) or the monolayer mechanism may occur in any particular case. Thus, in the case of tin deposits, a transition from an amorphous to a crystalline state was observed when the average thickness of the deposit was about 10 Å. This is consistent with the Frenkel model, in which it is assumed that deposited atoms still retain a certain amount of energy and move over the surface freely as a two-dimensional gas. As more atoms arrive on the surface, larger mobile aggregates form and at some stage spontaneous crystallization occurs. The problem is to predict where the crystallites will form and whether they will be oriented relative to the substrate. The crystallites may form at random points on the surface, or they may grow at the ends of dislocations or at gross faults in the substrate, as has been observed in the growth of copper on hot silver (see Kehoe *et al.* 1956). In the case of tin, both randomly oriented and oriented crystallites were formed, although their location was not known.

The growth of antimony deposits was similar to that described above, although the antimony crystallites, once formed, had only a fibrous orientation with the plane of closest packing in contact with the silver surface.

This mode of growth may also be described by the spontaneous crystallization of a supercooled liquid. Takagi (1954) found that thin layers of tin, lead and bismuth, 50 Å in thickness, showed remarkably large supercooling effects; up to 192 degrees for tin, 157 degrees for lead, and 147 degrees for bismuth. He also showed that the degree of supercooling increased with decreasing film thickness. Thus, in the case of tin which has a melting point of only 232°c, supercooling right down to room temperature might easily be obtained for the thinnest observable deposits.

Although there is some indirect evidence to suggest that this type of mechanism may occur to a limited extent in other cases, described below, it obviously does not apply generally to the same extent as in the growth of tin deposits. Thus, no amorphous or supercooled liquid state was observed in the initial stages of growth of bismuth, thallium or lead deposits even though these metals possess low melting points of 271°c, 304°c and 327°c respectively.

In the initial stages of growth of nickel, gold and copper (see Newman and Pashley 1955), oriented crystallites were formed. It was found that individual crystallites did not continue to grow as more material was deposited, but that the density of crystallites increased. Similar results have also been found by other workers using different materials (see Schulz 1952). These observations are in accord with a spontaneous nucleation process, although the average thickness when crystallization occurs would have to be very small, since no amorphous deposits are observed. The reason why the crystallites do not continue to grow is not known. In the case of the copper deposits, it may be argued that a thin surface film of oxide forms on the crystallites and prevents their further growth, but this argument cannot be applied to gold deposits. These observations explain in a simple way why deposits of these materials rapidly become randomly oriented when the thickness is increased beyond a few angstroms. When the density of crystallites becomes such that an appreciable proportion of the surface is covered, growth must occur on top of the initial crystallites. In general, there will be regions of misfit between neighbouring crystallites, since the lattice constant of the deposit bears no simple relationship to that of the substrate, and the crystallites grow at random points on the surface. Random growth would be expected from these regions of misfit. These results emphasize the need to examine the thinnest possible films when testing whether or not epitaxy occurs in a particular case.

Another type of growth occurred in the case of lead and thallium deposits which grew in the form of monolayers. Three-dimensional crystallites were only observed when the average thickness of the deposit was increased beyond about 4 Å. Thicker deposits again showed a mixture of oriented and randomly oriented crystallites. The randomly oriented material may have formed by the mechanism given above. The growth of silver on itself must also have proceeded by a monolayer mechanism because of the observed refraction effects from layers up to 60 Å in thickness. The growth of silver was different from that of the other face-centred cubic metals, since it grew in a strictly parallel orientation, in contrast to the orientation in double positioning in the other cases.

The reason for the non-orientation of certain metals such as cobalt, iron and palladium, may be due to low mobilities of atoms of these materials on the silver surface. This would be substantiated by the small crystal size observed for these deposits. Oriented growths of iron and palladium on a copper single crystal have, however, recently been found by Haase (1956).

The parameter of relative misfit between deposit and substrate is often regarded as an important factor in the formation of oriented overgrowths and this factor has been found to influence the nature of deposits in some cases. Thus, Schulz (1951, 1952) found that alkali halides grew as monolayers for small values of misfit with the substrate (less than 10% on mica, and less than 20% on other alkali halides), whereas nucleated growth occurred for larger misfits. Such an effect has not been observed in the present work. On the contrary, gold, nickel and copper grew as nucleated deposits, although the misfit is less than 14% in each case, while lead and thallium grew in the form of monolayers where the misfits are 21% and 19% respectively.

The lattice spacing of the deposit in the initial stages of growth is also of importance as a result of the theory of Frank and Van der Merwe (1949 a, b) and previously reported cases of pseudomorphism (for a review see Pashley 1956). If the deposit grows in the form of oriented three-dimensional crystallites which increase in density as the total amount of material is increased, then the growth of an individual crystallite cannot be followed. Thus, the lattice spacing of the atoms in the plane in contact with the substrate cannot be measured. Pseudomorphism could only be detected if the overgrowth builds up atom by atom in the form of a monolayer. Lead and thallium have grown in this way in the present experiments. The results show that the deposits had their own characteristic lattice constants in the earliest stages of their growth. The spacings found were somewhat modified from those of the bulk metals, but this may be expected as a result of the two-dimensional character of a monolayer. There was no evidence to support the theory of Frank and Van der Merwe (1949 a, b) which predicts that oriented monolayers are constrained to fit the substrate lattice. These two cases probably afford the best evidence on monolayer growth, although Schulz (1951, 1952) has also observed monolayer growth with alkali halides. The metal deposits seem to be somewhat superior than those due to the larger degree of misfit which results in a better resolution in the diffraction patterns. Also, no difficulty is experienced due to charging effects which cause a blurring of the patterns.

Finally, it should be remembered that the vacuum conditions under which such work as that described above was carried out, are far from satisfactory. It is well known that surfaces are covered with a monolayer of gas when the vacuum is only 10^{-5} mm Hg. Ideally, experiments should be performed in a vacuum of at least 10^{-9} mm Hg when the rate of bombardment of the surface by the gas molecules would be less than the rate at which the deposit atoms arrive (1 Å/min). Results obtained under these conditions may be vastly different from those described above, with regard to the size of crystallites and the degree of orientation. Unfortunately a vacuum of this order is not at present attainable in a standard metal apparatus.

Acknowledgments

The author wishes to thank Dr. M. Blackman for his interest and many useful discussions throughout the work. The author is also indebted to the University of London for a Postgraduate Studentship.

References

Caldwell, W. C., 1941, *J. Appl. Phys.*, **12,** 779.

Cockcroft, J. D., 1928, *Proc. Roy. Soc.* A, **119,** 293.

Collins, L. E., and Heavens, O. S., 1952, *Proc. Phys. Soc.* B, **65,** 825.

Ehlers, H., 1953, *Z. Phys.*, **136,** 379.

Frank, F. C., and Van der Merwe, J. H., 1949 a, *Proc. Roy. Soc.* A, **198,** 205; 1949 b, *Ibid.*, **200,** 125.

Frenkel, J., 1923, *Z. Phys.*, **26,** 117.

Geiling, S., and Richter, H., 1949, *Acta Cryst.*, **2,** 305.

Hass, G., 1948, *Z. Anorg. Chem.*, **257,** 166.

Haase, O., 1956, *Z. Naturforsch.*, **112,** 862.

Heavens, O. S., 1952, *Proc. Phys. Soc.* B, **65,** 788.

Kehoe, R. B., Newman, R. C., and Pashley, D. W., 1954, *J. Sci. Instrum*, **31,** 399; 1955, *Brit. J. Appl. Phys.*, **7,** 29; 1956, *Phil. Mag.*, **1,** 783.

Newman, R. C., 1955, *Ph.D. Thesis*, University of London.

Newman, R. C., and Pashley, D. W., 1955, *Phil. Mag.*, **46,** 927.

Pashley, D. W., 1956, *Advanc. Physics*, **5,** 173.

Pinsker, Z. L., 1953, *Electron Diffraction* (London: Butterworth).

Richter, H., 1943, *Phys. Z.*, **44,** 406.

Sakurai, T., and Munesue, S., 1952, *Phys. Rev.*, **85,** 921.

Schulz, L. G., 1949, *J. Chem. Phys.*, **17,** 1153; 1951, *Acta Cryst.*, **4,** 483; 1952, *Ibid.*, **5,** 130.

Takagi, M., 1954, *J. Phys. Soc., Japan*, **9,** 359.

The Scattering of Positive Ions by Neutral Atoms†

By D. W. SIDA
University College, London‡

[Received November 11, 1956, and in revised form March 24, 1957]

ABSTRACT

The interaction between a positive ion and a neutral atom is calculated from a statistical model which treats the electrons as a Fermi gas and considers the electrostatic forces between it and the nuclei, as well as the kinetic and exchange energies of the gas itself. This is applied to the case of Ca^{++} ions and neon atoms and of K^{+} ions and argon atoms. The former is extended to consider also neutral calcium atoms and neon atoms.

The elastic scattering of these ions is calculated by the classical and also by the quantum method over an energy range up to about 15 kev using these interactions. The results have been applied to problems of meteor trails (Massey and Sida 1955) and the spread of a beam of ions due to multiple scattering.

§ 1. INTRODUCTION

ALTHOUGH the scattering of electrons and protons has been explored theoretically, little has been accomplished for heavy atoms. These are important, for many processes, both in the laboratory and in astrophysics, involve the scattering between heavy atoms and ions. For example a knowledge of the behaviour of a beam of positive ions in a neutral gas is often required and such questions as its spread depend on the amount of scattering. In astrophysics the processes of excitation and ionization of meteor atoms are brought about by collisions with air molecules and atoms and using the methods of this paper these have been discussed by Massey and Sida (1955). The first requirement of the scattering problem is to obtain an accurate representation of the inter-atomic forces between the particles.

The Hellmann–Feynman theorem (Feynman 1939) indicates that the forces on the nuclei of a molecule as determined from quantum mechanical potential energy surfaces are essentially those arising from classical electrostatics and a knowledge of the electron probability density. Thus the inter-atomic forces will depend on obtaining this electron charge density and determining the electrostatic forces which arise from the nuclear charges and the inter-penetration of the electron shells. Most methods which have been used have been based on this theorem but the difficulty is to represent the electron density and the part played by the Pauli Principle. To overcome these problems it has been usual to postulate a form for the repulsive part of the potential as an exponential or a polynomial in inverse powers, and to obtain values for the parameters thereby introduced from considerations of such properties as viscosity, the virial coefficients and crystal structures (Massey and Burhop 1953, chap. VII).

---

† Communicated by Professor H. S. W. Massey, F.R.S. This paper is abridged from a thesis submitted to the University of London in support of an application for the degree of Doctor of Philosophy.

‡ Now at Mathematics Department, University of Leeds.

In this paper we do not postulate any particular form for the interaction between two atomic systems but make certain assumptions by which the electrons of the atoms concerned are treated statistically. The statistical model employed here is substantially that used for solid state investigations by Lenz and Jensen (1932) and refined and widely applied by Wigner and Seitz (1934) and by Gombas (1949). The electrons are treated in each particle as a free Fermi gas and we consider the change in the total energy of the two systems caused by overlapping of the two gases and also the electrostatic forces arising between the nuclei and these clouds. Thus one expects the method to be most applicable to particles with (*a*) many electrons and (*b*) closed shells (e.g. Ca^{++}, K^{+} A, Ne). There is a further restriction which may be important at high energies in that the particles must not approach each other too closely as no allowance is made for distortion of the original cloud distributions.

At large distances of nuclear separation the chemical repulsive forces are replaced by the attractive Van der Waals forces. To a first approximation these can be expressed as a single inverse power but the present method fails to give these terms, as indeed most other methods have failed. The attractive forces however give no contribution for the scattering of heavy particles above about 50 ev and hence are neglected in this paper.

In § 2 the interaction expression is derived and in § 3 applied to the two cases of calcium ions with neon atoms, and potassium ions with argon atoms. In § 4 these results are applied to calculations of elastic scattering and finally the problem of multiple scattering of a positive ion beam is also discussed.

§ 2. The Interaction between Atomic Systems

The outline of the method used in calculating the interaction between the systems is given in the paper by Massey and Sida (1955). The first formula is eqn. (8) of that paper which can be written in the form

$$V(r)=r^{-1}[W_1+W_2+W_3+W_4+W_5] \quad . \quad . \quad . \quad . \quad . \quad (1)$$

where

$$W_1 = e^2[Z_1Z_2 - \{Z_1N_2 + Z_2N_1\} + N_1N_2],$$

$$W_2 = e^2[Z_1N_2g_2(r) + Z_2N_1g_1(r)],$$

$$W_3 = -e^2N_1N_2\left[g_2(r) + r\int \frac{g_1(r_1)}{r_1}\,\frac{\nabla_2{}^2\phi_2(r_2)}{eN_2}\,\frac{d\tau}{4\pi}\right],$$

$$W_4 = \frac{A}{2}\int_0^\infty \int_{|r-r|}^{|r+r_1|} r_1r_2\{[\nabla_1{}^2\phi_1 + \nabla_2{}^2\phi_2]^{5/3} - [\nabla_1{}^2\phi_1]^{5/3} - [\nabla_2{}^2\phi_2]^{5/3}\}\,dr_2\,dr_1$$

$$W_5 = -\frac{B}{2}\int_0^\infty \int_{|r-r_1|}^{|r+r_1|} r_1r_2\{[\nabla_1{}^2\phi_1 + \nabla_2{}^2\phi_2]^{4/3} - [\nabla_1{}^2\phi_1]^{4/3} - [\nabla_2{}^2\phi_2]^{4/3}\}\,dr_2\,dr_1.$$

$V(r)$ is the interaction energy between the two systems when at a distance r apart. Z_1, Z_2 are the nuclear charges and N_1, N_2 the numbers of electrons in the respective systems. ϕ_1 and ϕ_2 are the electrostatic potentials due to the electron clouds in each atom and

$$\phi(r) = -\frac{Ne}{r}\{1 - g(r)\}.$$

A and B are the two constants

$$A = 0{\cdot}5312a_0e^{1/3}, \qquad B = 0{\cdot}3177e^{2/3}.$$

The first term W_1, is the coulomb interaction of the positive and negative charges and is zero if either particle is neutral. W_2 arises from one nucleus of charge Z_1e being penetrated by the charge cloud of the second. The cloud no longer screens its nucleus completely and the penetrated nucleus is thus repelled by the effective nuclear charge, $N_2g_2(r)$, of the approaching atom. W_3 arises from those parts of the charge clouds which overlap and hence no longer repel each other: the unsymmetrical form is due to simplifying by Green's theorem.

The interaction $V(r)$ can be evaluated if suitable forms for $Ng(r)$ and $\nabla^2\phi(r)$ are obtained for each atom. These represent the effective nuclear charge and charge density respectively and can be obtained from either the Fermi–Thomas–Dirac model or the Hartree–Fock field. The latter was chosen as being more accurate since the results are available for the atoms investigated. The two cases investigated were Ca^{++} ions with neon atoms and K^{+} ions with argon atoms. The integrations W_3, W_4 and W_5 were performed numerically and were rather laborious. The values of $Ng(r)$ and $\nabla^2\phi(r)$ for each atom were taken from the Hartree–Fock calculations for calcium (Hartree and Hartree 1938), potassium and argon (Hartree and Hartree 1935) and for neon (Brown 1933). In terms of Hartree's results

$$Ng(r) = Z_p + N - Z,$$

$$\nabla^2\phi(r) = \frac{1}{r^2}U(r),$$

where Z_p and $U(r)$ are tabulated.

We also investigated the effect of the two valence electrons, $(^4\text{S})^2$, of calcium and $V(r)$ was calculated by amending the values of $Ng(r)$ and $\nabla^2\phi(r)$ accordingly.

§ 3. RESULTS OF THE CALCULATIONS

From the form of $V(r)$, eqn. (1), being the sum of five terms it follows that there will be a certain amount of cancellation and this coupled with the tedious numerical calculations is rather a disadvantage to the method. Tables 1 and 2 give the results including values of the respective terms.

Table 1. Interaction of Ca^{++} Ions with Neon Atoms

r	$+W_2$	$-W_3$	$+W_4$	$-W_5$	ΣW_i	$V=(1/r)\Sigma W_i$
0·5	62·20	36·89	23·06	1·80	46·57	93·14
0·8	30·40	23·98	21·03	2·05	25·40	31·75
1·0	18·60	18·32	19·23	1·94	17·57	17·57
1·4	7·20	10·12	12·39	1·60	7·87	5·62
2·0	1·80	3·51 (3·66)	5·71 (6·11)	0·94 (1·09)	3·06 (3·16)	1·53 (1·58)
3·0	0·220	0·486 (0·762)	0·947 (1·578)	0·257 (0·422)	0·424 (0·613)	0·141 (0·204)
4·0	0·032	0·0635 (0·296)	0·121 (0·711)	0·055 (0·228)	0·0305 (0·219)	0·0076 (0·0548)
4·5	0·012	0·0235 (0·207)	0·043 (0·552)	0·025 (0·180)	0·007 (0·178)	0·0015 (0·0395)

Figures in parenthesis refer to amendment due to $(^4S)^2$ valence electrons for calcium. Unit of r is a_0 and of $V(r)$ it is e^2/a_0.

Table 2. Interaction of K^{+} Ions with Argon Atoms

r	$+W_2$	$-W_3$	$+W_4$	$-W_5$	ΣW_i	$V=(1/r)\Sigma W_i$
0·5	102·12	63·99	38·30	2·52	73·91	147·82
0·8	65·550	48·756	24·148	0·2390	38·552	48·19
1·0	47·690	40·530	23·897	2·432	28·625	28·625
2·0	7·077$_5$	11·079$_5$	10·901	1·710	5·189	2·594$_5$
3·0	0·9025	2·0120	3·1699	0·5725	1·308	0·436
4·0	0·1045	0·3040	0·7100	0·2327	0·2778	0·0694$_5$
5·0	0·0125$_5$	0·0400	0·1389	0·0640	0·0474$_5$	0·0095

Unit of r is a_0 and of $V(r)$ it is e^2/a_0.

The exchange term W_5 has little effect for $r<1$ but is of considerable importance at large distances. It can be shown that as $r \rightarrow 0$, W_4 and W_5 each tend to constant values.

For values of $r>4$, the interactions all tend to zero exponentially so that no attractive force is given. This forms a limit to the validity of the method and it would be unwise to extrapolate much further. So that in all applications we must ensure that any contribution to scattering from parts of the potential curve for $r>4$ is quite small ; this forms a lower limit to the energy and angle at which scattering can be investigated. It is impossible to carry out calculations of $V(r)$ at much larger distances since there are insufficient figures given in the Hartree-Fock results to allow for the cancellation which always occurs.

Actually Gombas (1943) introduced a further term (W_6), similar to W_5 to take account of electrons with anti-parallel spin, a polarization or correlation term, which he evaluated for the Fermi–Thomas–Dirac field. This he estimated increases the electron density in the marginal region of the atom by about 45% in his model but the exchange term by only 13%. Wigner (1934) also introduced a correlation term in his solution to the Hartree–Fock field with considerable improvement to his results which depended on long range interactions. However the work involved in such an amendment to the present scheme does not seem justified.

§ 4. ELASTIC SCATTERING AND MOMENTUM LOSS CROSS SECTION

The classical expression for the differential elastic scattering cross section should be quite valid for the heavy mass particles with which we are concerned down to very small angles and low energy. This is given by

$$I(\theta) \sin \theta \, d\theta \, d\phi = p \left| \frac{dp}{d\theta} \right| \sin \theta \, d\theta \, d\phi$$

where

$$\theta = \pi - 2p \int_{r_0}^{\infty} dr/r[r^2(1-V/E)-p^2]^{1/2}, \quad . \quad . \quad . \quad . \quad (2)$$

p is the impact parameter, r_0 is the largest singularity of the integrand. (Massey and Burhop 1953, p. 373). From this expression the momentum loss cross section is given by

$$Q_d(E) = 2\pi \int_0^{\pi} (1-\cos \theta) I(\theta) \sin \theta \, d\theta. \quad . \quad . \quad . \quad . \quad (3)$$

This converges since the $(1-\cos \theta)$ factor considerably decreases the effect of small angle scattering which according to (2) increases to infinity. Results for collisions of K^+ ions with energies ranging from 100 ev to 30 000 ev with argon atoms at rest are given in table 3 (Q_d) and in figs. 1 and 2 $I(\theta)$. The only experimental observations available for comparison are those of Rouse (1937) which are rather limited in angular range and are not absolute. As far as it can be checked there is good general agreement.

Cross sections for collisions of Ca^{++} ions with neon atoms have already been published by Massey and Sida (1955).

The quantum mechanical method gives the total elastic cross section and momentum loss cross section in terms of the phase shifts as follows (Mott and Massey 1949).

$$Q(E)=\frac{4\pi}{k^2}\sum(2n+1)\sin^2\eta_n \quad . \quad . \quad . \quad . \quad . \quad . \quad . \quad . \quad (4)$$

$$Q_d(E)=\frac{4\pi}{k^2}\sum(n+1)\sin^2(\eta_n-\eta_{n-1}) . \quad . \quad . \quad . \quad . \quad . \quad . \quad (5)$$

The B.W.K. approximation

$$\eta_n=\int_{r_n}^{\infty}\left[k^2-\frac{2m}{\hbar^2}V(r)-\frac{(n+\frac{1}{2})^2}{r^2}\right]^{1/2}dr-\int_{r_0}^{\infty}\left[k^2-\frac{(n+\frac{1}{2})^2}{r^2}\right]^{1/2}dr \quad . \quad (6)$$

where r_n and r_0 are the roots of the integrands, was used for large values of η_n and the Born approximation

$$\eta_n=-\frac{\pi}{2}\frac{2m}{\hbar^2}\int_0^{\infty}V(r)[J_{n+1/2}(kr)]^2r\,dr. \quad . \quad . \quad . \quad . \quad . \quad (7)$$

for small values up to a radian. It was found that for these heavy atoms the Born approximation was quite reliable up to this value.

Table 3. Momentum Loss Cross Section for Collisions of K^+ Ions with Argon Atoms

Energy (ev)	Q_d (units πa_0^2)	Energy (ev)	Q_d (units πa_0^2)
180	$4{\cdot}21_5$	4000	0·66
360	$3{\cdot}05_5$	10000	0·300
1000	1·68	20000	0·157
2000	1·08	30000	0·107

For calcium ions at 200 ev and potassium ions at 30 kev the momentum loss was calculated by both methods with good agreement in both cases.

There was no difference in the calculations over a range 100–2000 ev. for momentum loss or large angle scattering of Ca^{++} ions and neutral calcium atoms by neon atoms; the difference was only in small angle scattering ($<20°$) and is shown in the total elastic cross section calculated from (4) which was $37\pi a_0^2$ for Ca^{++} but $102\pi a_0^2$ for the neutral atoms.

The difficulty of experimental verification is indicated in the results for K^+ ions at 30 kev for which the quantum method gives $5\times10^9 a_0^2$ for zero angle scattering $I(0)$ while the classical method at 0·005 radians gives for $I(\theta)$ $8\times10^4 a_0^2$; this is a difference of 5 orders of magnitude in about 20 minutes of arc, for with such heavy particles classical scattering should be valid down to about 10 minutes of arc.

For large energies, above 10 kev, the results for ions indicate that the total momentum loss cross section varies approximately inversely with the energy.

Fig. 1

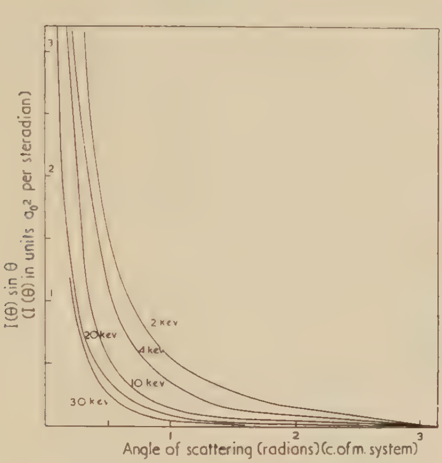

Elastic scattering of K^+ ions by argon atoms.
Energy 2–30 kev (lab. system).

Fig. 2

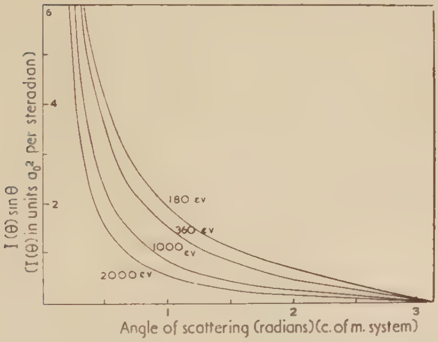

Elastic scattering of K^+ ions by argon atoms.
Energy 180 ev–2000 ev (lab. system).

§ 5. SPREAD OF AN ION BEAM DUE TO MULTIPLE SCATTERING

A narrow beam of positive ions will be spread by multiple scattering with gas atoms ; the amount of spread may be calculated as a function of the path length and pressure of the residual gas through which the beam passes. This is particularly important for isotope separation and similar experiments. From the above work it may be very simply evaluated to a good approximation.

Consider a particle incident in the z-direction on a scattering material. We suppose that in its collisions with the scatterer the particle loses a negligible fraction of its incident energy. Then, according to Fermi, the probability that, after penetrating a distance z into the scatterer, the transverse displacement of the particle is x and projection of its direction of motion on the xz plane makes an angle η with the z-axis, is

$$W(x\,;\,\eta\,;\,z)\,dx\,d\eta=\frac{\sqrt{3}}{2\pi}\frac{\lambda}{z^2}\exp\left\{-\frac{\lambda}{z}\left(\eta^2-3\eta\frac{x}{z}+\frac{3x^2}{z^2}\right)\right\}dx\,d\eta. \quad (8)$$

The mean free path λ is given in terms of a cross section Q_d by

$$\lambda=1/NQ_d \quad (9)$$

where N is the number density of particles and

$$Q_d=\int_0^{\pi}\int_0^{2\pi}(1-\cos\theta)I(\theta)\sin\theta\,d\theta\,d\phi \quad (10)$$

where $I(\theta)\sin\theta\,d\theta\,d\phi$ is the differential cross section for elastic scattering of the particles by the scatterer. This assumes that the scattering centres are infinitely massive. In our case in which the incident ions and scattering atoms are of nearly equal mass we must replace (10) by

$$Q_d^e=\int_0^{\pi}\int_0^{2\pi}(1-\cos\tfrac{1}{2}\theta)I(\theta)\sin\theta\,d\theta\,d\phi \quad (11)$$

which we shall call the effective diffusion cross section.

Scott (1949) expresses the formula (8) in terms of the angular displacement ψ and the direction ϕ to the chord of the position of the particle. Thus $\psi\simeq x/z$ and $\phi=\eta-\psi$. Hence in eqn. (8)

$$W(\psi\,;\,\phi\,;\,z)\,d\psi\,d\phi=\frac{\sqrt{3}}{2\pi}\frac{\lambda}{z}\exp\left\{-\frac{\lambda}{z}(\psi^2-\psi\phi+\phi^2)\right\}d\psi\,d\phi. \quad (12)$$

Table 4. Effective Diffusion Cross Sections Q_d^e for K$^+$ Ions in Argon

Energy (lab. system, kev)	$Q_d^e(\pi a_0^2)$
30	0·030
20	0·045
10	0·086
4	0·193

We transform to a dimensionless parameter

$$p=\lambda/z=1/NzQ_d. \quad (13)$$

which is the ratio of the mean free path to the total path traversed. Then on integrating over the angle ϕ we get the total probability of an angular displacement in one plane between ψ and $\psi+d\psi$ to be $W(\psi\,;\,z)\,d\psi$ where

$$W(\psi\,;\,z)=\left(\frac{3p}{4\pi}\right)^{1/2}\exp\left(-\frac{3p}{4}\psi^2\right). \quad (14)$$

For potassium ions in argon the effective diffusion cross section Q_d^e is found to have the values given in table 4.

Calculations were then made to obtain the distribution function (14) in a number of different cases of potassium ion beams in argon to investigate the effect of varying the total path length, the pressure, and the cross section (i.e. incident energy). The results are shown in figs. 3, 4 and 5. The considerable broadening of the beam for long path lengths, high pressures and low energies is clearly shown and indicates the degree

Fig. 3

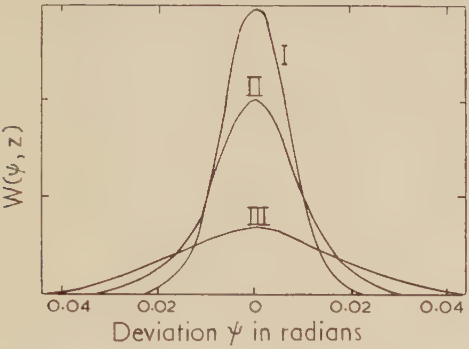

Multiple scattering of K+ ions in argon. Variation with path length (z).

Curve I $z=20$ cm. Curve II $z=40$ cm. Curve III $z=100$ cm.

(Pressure of gas $1{\cdot}3\times10^{-5}$ mm. Cross section $Q_d{}^e=0{\cdot}11\pi a_0{}^2$.)
Incident Energy 8 kev (lab.).

Fig. 4

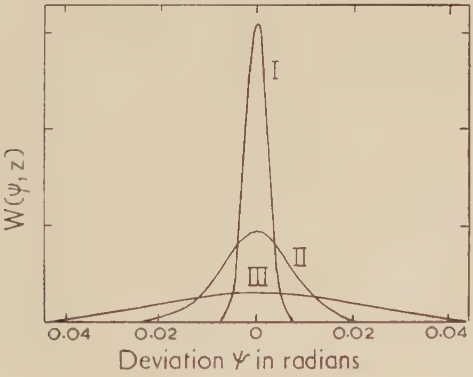

Multiple scattering of K+ ions in argon. Variation with pressure (p).

Curve I $p=1{\cdot}3\times10^{-6}$ mm. Curve II $p=1{\cdot}3\times10^{-5}$ mm.
Curve III $p=1{\cdot}3\times10^{-4}$ mm.

(Path length $z=20$ cm. Cross section $Q_d=0{\cdot}11\pi a_0{}^2$.)
Incident energy 8 kev (lab.).

to which these factors have to be taken into account in retaining a narrow beam, or in the case of isotopes in obtaining a high yield of separation. It must be remembered that no allowance has been made for the energy loss in small angle elastic scattering. This will also increase the broadening particularly in isotope separation. Its importance will be examined in a later paper.

Fig. 5

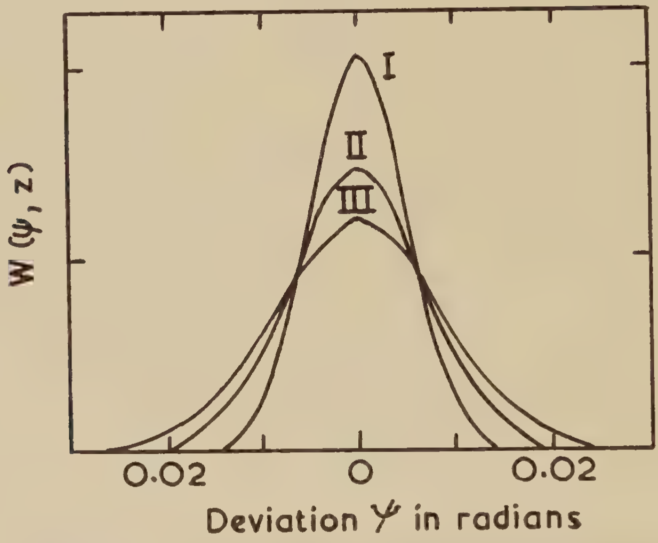

Multiple scattering of K+ ions in argon. Variation with cross section (Q_d). Curve I $Q_d=0{\cdot}055\pi a_0^2$, energy 16 kev (lab.). Curve II $Q_d=0{\cdot}11\pi a_0^2$, energy 8 kev (lab.). Curve III $Q_d=0{\cdot}16\pi a_0^2$, energy 5 kev (lab.).

(Path length $z=20$ cm. Pressure $p=1{\cdot}3\times10^{-5}$ mm.)

§ 6. EXTENSION TO VERY LOW ENERGIES

The present method has been shown to be suitable where the scattering is dependent only on the repulsive forces between the particles. For very low energies of several hundred degrees absolute, the attractive interactions associated with large inter-nuclear separations are of prime importance. Therefore for problems of this nature a polarization energy inversely proportional to the fourth power of this separation, can be postulated. It is not altogether clear under what circumstances the scattering is independent of the repulsive interaction. A calculation of the mobility of potassium ions in argon atoms at 293°K gave a value 20% below the experimental result when only a polarization potential was used. The result differed even further from the Langevin theory and furthermore the variation with temperature was also very different. This suggests that the region of the interaction where it reaches a minimum and where it changes from positive to negative values must be taken into account for low energy scattering. At present there is no obvious way of fitting a polarization potential to the statistical results and it would seem that this is required so that we have a continuous curve. The most likely method would be to investigate the potential forms required to give the experimental mobility results in the same way that the viscosity has been used for calculations on the interactions between neutral atoms. The wide range and accuracy of the experimental data make this possible and such a programme is obviously desirable from a theoretical standpoint.

ACKNOWLEDGMENTS

I wish to thank Professor H. S. W. Massey, F.R.S. for suggesting this work and for his guidance and help throughout. Also I must thank Miss Jean Nicholson for carrying out most of the long calculations involved and the Department of Scientific and Industrial Research for a maintenance award.

REFERENCES

BROWN, F. W., 1933, *Phys. Rev.*, **44,** 214.
FEYNMAN, R. P., 1939, *Phys. Rev.*, **56,** 340.
GOMBAS, P., 1943, *Z. Phys.*, **121,** 523; 1949, *Die Statistische Theorie des Atoms* (Vienna: Springer).
HARTREE, D. R., and HARTREE, W., 1935, *Proc. roy. Soc.* **A, 149,** 210; 1938, *Ibid.*, **164,** 167.
LENZ, W., and JENSEN, H., 1932, *Z. Phys.*, **77,** 713, 722.
MASSEY, H. S. W., and BURHOP, E. H. S., 1953, *Theory of Electronic and Ionic Phenomena* (Oxford: University Press), Chap. VII.
MASSEY, H. S. W., and SIDA, D. W., 1955, *Phil. Mag.*, **46,** 190.
MOTT, N., and MASSEY, H. S. W., 1949, *Theory of Atomic Collisions*, 2nd Edn. (Oxford: University Press).
ROUSE, W., 1937, *Phys. Rev.*, **52,** 1238.
SCOTT, W. I., 1949, *Phys. Rev.*, **76,** 212.
WIGNER, E., 1934, *Phys. Rev.*, **46,** 1002.
WIGNER, E., and SEITZ, F., 1934, *Phys. Rev.*, **46,** 509.

Photoelastic Study of Dislocation Arrangements in Crystals†

By J. F. Nye, R. D. Spence‡ and M. T. Sprackling

H. H. Wills Physics Laboratory, University of Bristol

[Received February 28, 1957]

Abstract

The plastic deformation of single crystal bars of silver chloride in tension and bending has been studied by using the photoelastic effect. It is found that in tension the plastic deformation is not uniform over a given cross section but is greatest near the surfaces. In bending the plastic deformation is found to propagate longitudinally along the bars rather than transversely. The distribution of birefringence, and hence that of stress, has been measured and the result interpreted by means of a simple dislocation model. It is concluded that, in silver chloride, the ratio of the stress necessary to propagate dislocations to the stress necessary to generate them is less than about 0·6. The shear stress on the glide plane necessary to propagate dislocations is approximately $5{\cdot}2\times10^6$ dynes/cm^2.

§ 1. Introduction

When a crystal is not fully annealed the dislocations within it produce long range elastic strains. In a transparent cubic crystal such strains are visible as distributions of birefringence produced by the photoelastic effect. Detailed photoelastic observations of silver chloride under a low power microscope (Nye 1949 a, b) have shown that, after plastic deformation by glide, the internal stresses are of two kinds (other cubic crystals show similar effects). (A) Each glide packet is subject to pure elastic bending ; this gives a ‘ saw-tooth ’ distribution of stresses with a period equal to the spacing of the glide zones. (B) Superimposed on the saw-tooth distribution is a more slowly varying stress ; it is this second, larger scale, kind of stress which is the subject of the present note.

§ 2. Experiments

2.1. *Plastic Extension*

Single crystal bars of silver chloride have been prepared with rectangular cross sections of dimensions 1×1 to 1×5 mm and lengths from 30 to 45 mm. The final treatment of the surfaces was a polish produced by agitation in a strong solution of 'hypo' for a few minutes. The orientations were variable. When a fully annealed crystal is plastically extended and the load is removed a photoelastic pattern is seen between crossed nicols which corresponds to stresses of type (B). It always has the general form shown in fig. 1(*a*)†. In this figure two neutral lines are visible parallel to the length of the specimen. (The path differences in this, as in nearly all our experiments, are less than a quarter of a wavelength and the extinction angle is nearly the same at all points of any one specimen.) The neutral lines also show up well in a circular polariscope. The variation of the birefringence across the specimen, which gives rise to the photoelastic pattern, is shown by the curve in fig. 1(*b*). Since we may assume that the birefringence is proportional to the stress, the curve may equally well be taken to represent the distribution of the (longitudinal) internal stress σ in the specimen. A photoelastic pattern of the same general type is seen when the bar is viewed through the other pair of opposite faces. The sign of the effect is such that the outer parts of the bar are in compression, while the inner core is in tension. It seems, therefore, that during the plastic extension the outer layers have deformed plastically more than the inner core; for when the load is removed the outer part would then be thrown into compression, as is observed. One is thus led to conclude tentatively that more dislocation sources are active at or near the surface than in the interior.

---

† Communicated by the Authors.

‡ Present address : Physics Dept., Michigan State University, East Lansing, Michigan, U.S.A.

2.2. *Plastic Bending*

When a similar specimen is bent elastically by applying equal and opposite couples to the ends, so that the upper side is convex, the photoelastic pattern seen between crossed nicols is as shown in fig. 2(*b*). The corresponding distribution of birefringence, and therefore, we suppose, of longitudinal stress, is drawn in fig. 2(*a*). The bar thus shows the normal linear variation of stress to be expected within the elastic range, and if the couples are removed the birefringence disappears. (As will be explained later, the specimens from which the photographs of fig. 2(*b*, *c*, *d*) are taken were actually partly in the elastic and partly in the plastic range; the section shown in fig. 2(*b*), however, was completely elastic and serves well enough for illustration.) When the bar is bent into the plastic range the photoelastic pattern changes to that shown in fig. 2(*d*) and the corresponding distribution of birefringence and stress is then as shown in fig. 2(*e*). If now the couples are removed from the ends the photoelastic pattern changes to fig. 3(*a*) and the corresponding stress distribution to fig. 3(*b*). There are now three neutral planes and the resultant distribution gives no resultant force or couple (bending moment) over a cross section. Figure 3(*b*) is the same as fig. 2(*e*) except for the addition of a linear elastic stress distribution; we therefore conclude that there is no significant reverse plastic deformation when the external couples are removed.

---

† All figures are plates.

The sign of the residual stress in these bending experiments is again consistent with the hypothesis that more plastic deformation has taken place near the surface than in the interior—but this is hardly surprising, since the outer layers were the most highly stressed during the bending. What is surprising is (i) the very high stress gradient across the neutral plane in fig. 2(*e*), as shown by the sharpness of the central dark line in fig. 2(*d*), and (ii) the uniformity of the stress in all other regions, except possibly in the regions very close to the edges. The transition from a uniform tension σ_p to a uniform compression $-\sigma_p$, as judged by the change in sign of the birefringence, occurs over a distance which is typically about 0·1 mm. The actual transition may be even sharper, because it is probably blurred by overlapping of successive layers of crystal normal to the direction of viewing. The birefringence is uniform outside the transition region to within 5%.

One naturally asks what are the intermediate stages by which the pattern of fig. 2(*d*) is produced. The conventional view of plastic bending is that the deformation starts at the more highly stressed outer surfaces, and then two plastic regions spread inwards towards the neutral plane, one from each side of the bar. But in our specimens this was not the case. Instead of propagating transversely, the deformation propagated longitudinally down the bar. It began at one end near the knife-edges used to produce the couples, and progressed down the bar at a rate which could be controlled by the rate of bending. Figures 2(*b*), (*c*) and (*d*) show three sections of bars in which the plastic zone had reached an intermediate position and with the external couples still applied. The section in fig. 2(*b*) is still in the elastic range, as already described. The section in fig. 2(*d*) is plastically bent. Figure 2(*c*) shows the transition region : its length is rather less than the width of the specimen.

To find numerical values for the stresses we need to know the photoelastic constant, but since cubic crystals are not photoelastically isotropic the appropriate photoelastic constant depends on the crystal orientation. We have therefore measured the constant for each of our specimens by applying known bending couples in the elastic range and measuring the birefringence at known distances from the neutral plane. This enables us to deduce the longitudinal stress at any point in a plastic or partially plastic bar. In a partially plastic bar equilibrium considerations show that the maximum stress σ_m in the elastic part must be $\frac{3}{2}$ times the uniform stress σ_p in the plastic part. This is verified by our experiments. Values of σ_m in five different specimens were 12·7, 17·6, 19·4, 11·7, $18{\cdot}8\times10^6$ dynes/cm^2. Since deformation appeared to be by glide on a single set of planes we have calculated the corresponding shear stresses on the glide plane (not resolved along the glide direction, since this was not known). The results are 5·7, 8·5, 9·7, 5·8, $9{\cdot}0\times10^6$ dynes/cm^2 ; mean$=7{\cdot}8\times10^6$ dynes/cm^2. The shear stress on the glide plane in the plastic region is $\frac{2}{3}$ of these values and thus has a mean of $5{\cdot}2\times10^6$ dynes/cm^2.

§ 3. Tentative Model

Our tentative explanation of the behaviour of the bars in bending is briefly as follows. We may first try to explain how the distribution of stress shown in fig. 3(*b*) can be maintained. As a start, consider a row of negative edge dislocations arranged along the neutral plane with Burgers vectors parallel to the neutral plane and with their lengths parallel to the axis of bending. They would produce a stress 'discontinuity' on the neutral plane of the same sign as that observed, that is, tension above and compression below (Nye 1949 b). But since the extra half-planes would be in the lower half of the crystal the bar would be bent with the upper surface concave ; this is the opposite curvature to that observed. Such a model therefore fails.

We can, however, produce both a curvature and a stress discontinuity of the correct sign by taking the following related model. The crystal is filled with a macroscopically continuous distribution of positive dislocations. These produce a curvature of the correct sign, but if arranged suitably (Nye 1953) they give no macroscopic internal stress. We now remove those (positive) dislocations which are situated within a narrow band containing the neutral plane. This is equivalent to adding a narrow strip of negative dislocations and produces a stress discontinuity of the correct sign. According to this model, then, the observed stress distribution is produced not so much by the presence of dislocations as by an absence of them.

In the real crystal bars the Burgers vectors of the dislocations responsible for the bending are not parallel to the neutral plane. We deal with this by superposing on our model a distribution of edge dislocations with Burgers vectors perpendicular to the axis of the bar. This second distribution produces no long-range stresses but accomplishes the necessary adjustment of the resultant Burgers vectors. There will also doubtless be present in the real crystal bars other dislocations apart from those responsible for the bending, but since their arrangement is such as to produce no long range stresses they make no contribution to the photoelastic effect.

An explanation for the longitudinal propagation shown in fig. 2 may be derived from a recent paper by Read (1957). Read has calculated the bending moment versus curvature curve for plastic bending by using a simple dislocation model. In his model σ_c is the stress necessary to generate dislocations and σ_0 is the stress necessary to move them through the crystal. The curve obtained depends on the ratio $\sigma_0\ \sigma_c$ and is such that the bending moment goes through a maximum for all values of $\sigma_0\ \sigma_c$ between 0 and 1. However, when $\sigma_0\ \sigma_c$ is greater than about 0·67 the maximum is very flat, and would easily be destroyed if a little strain-hardening were introduced. On the other hand, when $\sigma_0\ \sigma_c$ is less than 0·6 the bending moment goes through a sharp maximum at the elastic limit. This, from our point of view, is the crucial fact, for we should then expect instability in a bending test ; when deformation started at a certain place it would continue there preferentially. (One is reminded of the behaviour of mild steel in tension.) The fact that the deformation is non-uniform along the length of the silver chloride bars can therefore be interpreted to mean that in this crystal σ_0/σ_c is less than about 0·6.

Apart from the instability just mentioned, which is a logical consequence of Read's model, our results for the distribution of stress in the plastic region shown in fig. 2(*e*) are in general agreement with Read's theoretical expectations. In particular, the uniform stress σ_p that we observe may be identified with the theoretical stress σ_0. (For completeness it should also be said that according to Read's model, the stress in the regions very close to the upper and lower surfaces in fig. 2(*e*) would not be σ_0 but would rise linearly from σ_0 to the value σ_c on the surface. Unfortunately, however, the viewing conditions in these narrow regions very close to the surfaces are not good enough to enable us to say whether or not they behave as the theory predicts.)

We have seen that the stress σ_p, and therefore the stress σ_0 necessary to move dislocations through the crystal, is $5{\cdot}2\times10^6$ dynes/cm^2 when expressed as a shear stress on the glide plane. Our experiments give no precise information as yet about the value of the shear stress necessary to generate the dislocations beyond the fact that it must be greater than about 1/0·6 times this value, that is, greater than $8{\cdot}7\times10^6$ dynes/cm^2.

More detailed measurements are being made of the phenomena both in pure tension and in bending, and a full account will be published.

ACKNOWLEDGMENTS

We should like to thank Professor F. C. Frank for kindly reading and commenting on the manuscript of this paper. The work described was done while R. D. Spence was a Fellow of the John Simon Guggenheim Memorial Foundation, and M. T. Sprackling was receiving a maintenance grant from the Department of Scientific and Industrial Research.

REFERENCES

NYE, J. F., 1949 a, *Proc. Roy. Soc.* A, **198,** 190 ; 1949 b, *Ibid.*, **200,** 47 ; 1953, *Acta Met.*, **1,** 153.

READ, W. T., Jr., 1957, *Acta Met.*, **5,** 83.

The Absorption of Slow Negative π-Mesons by the Elements in Nuclear Emulsions†

By G. Brown and I. S. Hughes
Department of Natural Philosophy, The University, Glasgow

[Received March 15, 1957]

In all previous investigations of the absorption of slow negative π-mesons by the constituent elements in nuclear emulsions, the separation of the observed events into those involving the nuclei of the light elements (carbon, nitrogen and oxygen), and of the heavy elements (silver and bromine) has been achieved largely by means of the ' α-particle method '. In order to effect a separation of the events in light and heavy nuclei independently of the α-particle, and other indirect methods, an experiment has been performed in which π-mesons were allowed to pass into emulsions of different compositions.

Ilford normal G5 and dilute G5 × 4 emulsions were exposed simultaneously and symmetrically to π-mesons obtained by means of the Glasgow 300 mev synchrotron. The stars induced by the π^--mesons which stopped in the emulsions were subdivided according to the number n, of secondary prongs.

The numbers of stars with $n \geqslant 1$ have been corrected for the efficiencies of the observers for different types of event in normal and dilute emulsions. The relative numbers in dilute and normal emulsions have also been normalized to allow for differences in the areas scanned in each type of emulsion, for the differences in stopping power and for slight differences in thickness. The final normalization factor is in agreement with that obtained by comparing the numbers of positive π-mesons stopping in the two types of emulsion. The prong distributions were obtained with the conventions (a) that only tracks of length $\geqslant 5\,\mu$ were counted as prongs and (b) that all tracks having a definite direction were counted as prongs. The results presented are those obtained using convention (b).

If σ_H and σ_L are the cross sections for the production of a particular type of event in heavy and light elements respectively, then the equivalent numbers of such an event in the normal and dilute emulsions are given by

$$N_{\text{normal}} \propto 2{\cdot}06\sigma_H + 2{\cdot}67\sigma_L$$

$$N_{\text{dilute}} \propto 0{\cdot}92\sigma_H + 4{\cdot}32\sigma_L$$

where the numerical coefficients are proportional to the numbers of heavy and light nuclei in the two types of emulsion. These equations may be solved to give σ_H and σ_L and hence the percentages of the various types of events in heavy and light elements for the normal emulsion.

In order to decrease the statistical errors in σ_H and σ_L, for the normal emulsion we have added to the data of the present experiment for this type of emulsion those of all the previous workers who have used a criterion similar to ours for the minimum prong length. Thus well determined values are obtained for N_{normal} and the statistical errors in the final results arise from the more limited numbers of events, from the present experiment alone, which contribute to N_{dilute}.

---

† Communicated by Professor P. I. Dee, F.R.S.

The distribution in prong number for the heavy elements is shown in fig. 1(*a*) as a percentage of all stars in heavy nuclei, while fig. 1(*b*) shows the corresponding results for light nuclei. The errors shown are standard deviations and include the errors in the efficiency determinations. In order to compare the results with those obtained by other workers the numbers are presented in the table as percentages of the total number of π^- stars in nuclei other than hydrogen in a normal emulsion. The results of the present experiment offer direct confirmation of the results obtained by the more indirect methods.

Fig. 1

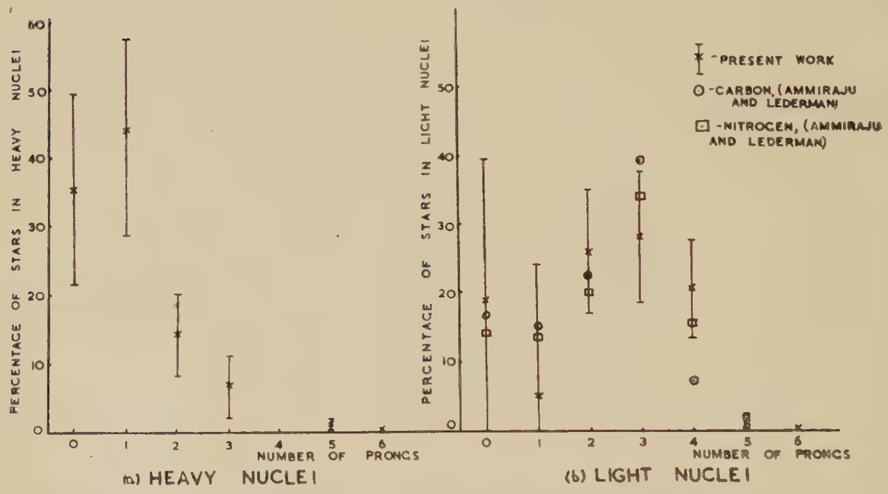

Distribution in prong number for (*a*) stars formed by absorption of the π-meson in a heavy nucleus, and (*b*) stars formed by absorption of the meson in a light nucleus. For light nuclei the results are compared with those of Ammiraju and Lederman (1956) for the aborption of mesons in carbon and in nitrogen.

No direct determination was made of the number of events without secondary prongs. However, using a mean value of the proportion of stars without secondary prongs obtained by Menon *et al.* (1950), Adelman (1952), and Demeur *et al.* (1956) for a normal emulsion, it is possible to determine the total number of negative mesons entering the emulsions. Subtraction of the number of events with $n \geqslant 1$ then gives the number of events with $n=0$ in the dilute emulsion. The percentages of stars with $n=0$ in light and heavy nuclei have been obtained in this way.

In fig. 1(*b*), along with the results of the present experiment for light nuclei, are shown the prong distributions obtained for the absorption of π^--mesons in carbon and nitrogen by Ammiraju and Lederman (1956) using a diffusion cloud chamber. The apparent difference in the percentage of four-prong stars observed by these workers and in the present experiment is attributable to the presence of a considerable proportion of oxygen among the light elements contained in a nuclear emulsion. If, as is strongly indicated by the presence of a maximum in the prong distribution at $n=3$, a common consequence of the absorption of a π^--meson by a light nucleus is its complete disintegration into α-particles, a proton and neutrons, then oxygen will frequently give a four-prong star.

Author	Number of stars	Percentage of stars with n prongs					
		$n=0$		$n=1$		$n=2$	
		L	H	L	H	L	H
Menon *et al.* (1950)	500	— 28 —		8	19	9	13
De Sabbata *et al.* (1953)	500	— 27 —		6·5	26	9·5	9·5
Demeur *et al.* (1956)	1038	— 35 —		3	23	7	10·5
Present Work	788	7·5	21	2	26	10·5	8·5
		±8·5	±9	±8	±10	±3	±3·5

		$n=3$		$n=4$		$n=5$	
		L	H	L	H	L	H
Menon *et al.* (1950)	500	11	3	4·5	3·5	0·5	0·5
De Sabbata *et al.* (1953)	500	12	2·5	4·5	1·5	1·0	0·1
Demeur *et al.* (1956)	1038	11	2·5	6·5	0·2	1·5	0
Present work	788	11	4	8	—2·5	0·3	1·0
		±3	±3	±2	±2·0	±0·3	±1·0

L—Light nucleus H—Heavy nucleus

ACKNOWLEDGMENT

The authors are grateful to Dr. H. Muirhead, who originally suggested this experiment, for valuable discussions throughout the course of the work.

REFERENCES

ADELMAN, F. L., 1952, *Phys. Rev.*, **85**, 249.
AMMIRAJU, P., and LEDERMAN, L. M., 1956, *Nuovo Cim.*, **2**, 283.
DEMEUR, M., HULEUX, A., and VANDERHAEGHE, G., 1956, *Nuovo Cim.*, **4**, 509.
DE SABBATA, V., MANARESI, E., and PUPPI, G., 1953, *Nuovo Cim.*, **10**, 1704.
MENON, M. G. K., MUIRHEAD, H., and ROCHAT, O., 1950, *Phil. Mag.*, **41**, 583.

The Nuclear Photoeffect in Light Nuclei†

By F. C. Barker
Research School of Physical Sciences, Australian National University

[Received February 2, 1957]

The energy of the giant resonance of the nuclear photoeffect is observed to be roughly independent of the mass number A for $A \lesssim 30$, then to decrease slowly as A increases (Ferguson *et al.* 1954). Several calculations of the energy have been made for heavy nuclei, exhibiting the decrease for large A (see Levinger 1954). Here we show that the results for light nuclei are consistent with the predictions of the nuclear shell model.

Observationally the most characteristic energy associated with the giant resonance is the peak energy E_m. This however is not very significant theoretically, and we have calculated instead the harmonic mean energy W_H defined by

$$W_H = \frac{\int_0^\infty \sigma(E)\,dE}{\int_0^\infty E^{-1}\sigma(E)\,dE},$$

where $\sigma(E)$ is the total absorption cross section for γ-rays of energy E. It is difficult to obtain precise values of W_H from the observed cross sections, as usually only one or other of the partial cross sections, such as $\sigma_{\gamma n}$, has been measured. The estimates of W_H which we use for comparison with the calculations are given in the last column of the table, and are admittedly very rough. This is particularly the case for those based on the cross sections of Ferguson *et al.* (1954), which are uncertain at energies above the giant resonance and most likely lead to values of W_H which are too small.

If it is assumed that only electric dipole absorption is operative, then (Levinger and Bethe 1950)

$$W_H = \frac{(\Psi_0{}^\dagger[D^\dagger HD - D^\dagger DH]\Psi_0)}{(\Psi_0{}^\dagger D^\dagger D\Psi_0)}. \qquad \ldots\ldots \quad (1)$$

Here Ψ_0 is the ground state wave function, H is the nuclear Hamiltonian and D is the electric dipole operator

$$D = \sum_{i=1}^{A} \tfrac{1}{2}(1-\tau_{0i})\left(z_i - \frac{1}{A}\sum_{j=1}^{A} z_j\right).$$

Levinger and Kent (1954) and Levinger (1955) have used shell model wave functions in (1) to calculate W_H for various nuclei. An alternative formula for W_H is

$$W_H = \frac{(\Psi_0{}^\dagger D^\dagger HD\Psi_0)}{(\Psi_0{}^\dagger D^\dagger D\Psi_0)} - \frac{(\Psi_0{}^\dagger H\Psi_0)}{(\Psi_0{}^\dagger\Psi_0)}, \qquad \ldots\ldots \quad (2)$$

which is identical with (1) if Ψ_0 is the exact wave function of the ground state corresponding to the Hamiltonian H. For approximate wave functions Ψ_0, the two formulae give different results. W_H given by (2) can be interpreted as the difference E_1-E_0 of the expectation values of the Hamiltonian in the state $\Psi_1\equiv D\Psi_0$ and in the ground state. Only eigenstates of H which contain appreciable amounts of Ψ_1 will be excited by E1 absorption, and these states will have energies near E_1 (see Wilkinson 1955).

---

† Communicated by Professor K. J. Le Couteur.

For Ψ_0 we have taken shell model wave functions belonging to the lowest configuration and in L–S coupling, built up from wave functions for single particles in an oscillator potential well with parameter a. These wave functions are given in the table, for the various light nuclei we have considered. Although they may not represent the actual ground states very well, they should be satisfactory for our calculation which does not appear to be sensitive to the choice of Ψ_0. The nuclear Hamiltonian has been assumed to contain a general charge-independent two-body central interaction between nucleons :

$$H=-\frac{\hbar^2}{2M}\sum_{i=1}^{A}\nabla_i^2+\sum_{i<j=1}^{A}[a_0+a_\sigma(\sigma_i\,.\,\sigma_j)+a_\tau(\tau_i\,.\,\tau_j)$$
$$+a_{\sigma\tau}(\sigma_i\,.\,\sigma_j)(\tau_i\,.\,\tau_j)]J(r_{ij}).$$

For all of our calculations we have used a Yukawa potential

$$J(r)=V_0\exp(-\kappa r)/\kappa r.$$

If the values of W_H given by (1), (2) are called W_{H1}, W_{H2} respectively, then we note that matrix elements of only one-particle and two-particle operators are required for W_{H1}, whereas W_{H2} involves matrix elements of one-, two-, three- and four-particle operators. To calculate W_{H2}, we therefore use

$$W_{H2}=W_{H1}+\Delta W_H$$

where

$$\Delta W_H=\frac{\sum\limits_{n\neq0}(\Psi_0\,D^\dagger D\Psi_n)(\Psi_n\,H\Psi_0)}{(\Psi_0{}^\dagger D^\dagger D\Psi_0)}.$$

The orthonormal states Ψ_n include all those which are coupled to Ψ_0 by both of the operators $D^\dagger D$ and H, apart from Ψ_0 itself. Because oscillator wave functions are used, there is only a finite manageable number of such states Ψ_n. Only one- and two-particle matrix elements are required in ΔW_H. Thus W_{H1} and ΔW_H can be calculated by standard fractional parentage techniques (Elliott 1953). Then

$$W_{H1}=\hbar^2/Ma^2+\alpha V_0,$$
$$\Delta W_H=-\hbar^2/2Ma^2+\beta V_0.$$

It is found that both α and β are closely proportional to $(\kappa a)^{-2}$, so that

$$W_{H1}=\hbar^2/Ma^2(1+\gamma_1 b),$$
$$W_{H2}=\hbar^2/Ma^2(\tfrac{1}{2}+\gamma_2 b),$$

where $b=MV_0/\hbar^2\kappa^2$, and $\gamma_1=(\kappa a)^2\alpha$ and $\gamma_2=(\kappa a)^2(\alpha+\beta)$ are more or less independent of κa. Also b does not depend sensitively on κ if the internucleon potential is assumed to be the same as that acting between neutron and proton in the deuteron, since then (Rosenfeld 1948)

$$b=1{\cdot}680+2{\cdot}266\eta-0{\cdot}246\eta^2+0{\cdot}144\eta^3-\ldots,$$

where $\eta=(ME_B/\hbar^2\kappa^2)^{1/2}$, E_B being the deuteron binding energy. For reasonable values of κ, this gives b close to 2·3, which value we have used. The calculations have been carried out both for a Rosenfeld potential :

$$a_0=0, \qquad a_\sigma=0, \qquad a_\tau=0{\cdot}100, \qquad a_{\sigma\tau}=0{\cdot}233,$$

and for a Serber potential :

$$a_0=-0{\cdot}30, \qquad a_\sigma=0{\cdot}05, \qquad a_\tau=0{\cdot}15, \qquad a_{\sigma\tau}=0{\cdot}10.$$

The value of a has been chosen to make the mean square radius of the nucleus equal to $\frac{3}{5}(r_0A^{1/3})^2$, leading to the values of a/r_0 given in the table. These distances have been measured from the centre of mass of the nucleus rather than from the well centre. For the moment we assume that r_0 is the same for all the nuclei considered, and choose the value of r_0 to make W_H for ^{16}O fit the experimental value, taken as 25 Mev. These values of r_0 are given in the table below the columns giving the values of W_{H1} and W_{H2}.

A further calculation has been made for ^{12}C, including a spin–orbit interaction in the Hamiltonian and using intermediate coupling for the ground state wave function. It is easily seen, however, that this spin–orbit interaction gives no direct contribution to either W_{H1} (Frankel 1955) or ΔW_H. The ground state wave function of ^{12}C obtained by fitting certain properties of ^{13}C and ^{13}N (Lane 1953) is

$$\Psi_0=0{\cdot}829\Psi([44]000)-0{\cdot}497\Psi([431]011)+0{\cdot}107\Psi([422]000)$$
$$-0{\cdot}208\Psi([422]022)-0{\cdot}103\Psi([332]011),$$

all states belonging to the configuration $1s^41p^8$. We have approximated this by

$$\Psi_0=0{\cdot}83\Psi([44]000)-0{\cdot}56\Psi([431]011).$$

There are no contributions to W_H from interference between these states (such contributions come only from states with the same S and L values and even then are very small), so the values of W_H obtained with the new Ψ_0 are not very different from those obtained previously, being of the order of 1 Mev less.

From the table it is seen that, apart from the values of r_0 required, the Rosenfeld and Serber potentials give similar results, and the same is true of the formulae (1) and (2) for the nuclei with $A \lesssim 10$. For these nuclei the agreement with the experimental results is reasonably good. The discrepancy in the case of ^{9}Be may be removed by choosing a larger value of r_0 for this nucleus, of order $1{\cdot}5\times10^{-13}$ cm ; this change is supported by experimental evidence from electron scattering and mirror nuclei (Hofstadter 1956) which indicates that r_0 is appreciably greater for Li and Be than for He, C or O. For ^{4}He, W_{H1} seems to agree better with the experimental value than does W_{H2}. If, however, W_H were of

Values of Harmonic Mean Energy W_H and Peak Energy E_m for various Light Nuclei

Nucleus	$\Psi_0(C[\lambda]TSL)$	$\frac{a}{r_0}$	Rosenfeld		Serber		Experimental	
			W_{H1} (MeV)	W_{H2} (MeV)	W_{H1} (MeV)	W_{H2} (MeV)	E (MeV)	W_H (MeV)
^{4}He	$\Psi(1s^4[4]000)$	1·160	32·4	20·7	32·5	16·7	$24{\cdot}0^a$, $26{\cdot}0^b$	29^b
^{6}Li	$\Psi(1s^41p^2[2]010)$	1·118	32·8	24·6	33·9	22·8	—	—
^{7}Li	$\Psi(1s^41p^3[3]\frac{1}{2}\frac{1}{2}1)$	1·131	32·9	28·7	33·4	26·8	—	—
^{9}Be	$\Psi(1s^41p^5[41]\frac{1}{2}\frac{1}{2}1)$	1·172	31·0	29·1	31·3	27·4	$22{\cdot}0^c$	21^c
^{10}B	$\Psi(1s^41p^6[42]012_I)$	1·196	29·6	27·4	30·2	26·5	—	—
^{12}C	$\Psi(1s^41p^8[44]000)$	1·241	28·6	28·8	28·6	27·6	$22{\cdot}5^d$, $23{\cdot}0^e$	$29^{d,e}$
^{13}C	$\Psi(1s^41p^9[441]\frac{1}{2}\frac{1}{2}1)$	1·264	27·0	26·6	27·2	26·3	$25{\cdot}5^f$	25^f
^{14}N	$\Psi(1s^41p^{10}[442]012)$	1·287	25·9	25·1	26·3	25·2	$22{\cdot}5^a$	21^a
^{16}O	$\Psi(1s^41p^{12}[444]000)$	1·330	25·0	25·0	25·0	25·0	$22{\cdot}5^a$, $24{\cdot}0^e$	22^a, 26^e
^{20}Ne	$\Psi(1s^41p^{12}2s^4000)$	1·350	24·0	23·1	24·1	24·4	$21{\cdot}5^a$	20^a
^{36}A	$\Psi(1s^41p^{12}1d^{20}000)$	1·501	19·7	21·3	19·6	21·0		
^{40}Ca	$\Psi(1s^41p^{12}2s^41d^{20}000)$	1·539	18·8	21·4	18·7	22·7	$20{\cdot}0^{a\dagger}$	$19^{a\dagger}$
	r_0 (10^{-13} cm)		1·25	1·35	1·14	1·31		

a Ferguson *et al.* 1954,
b Perry and Bame 1955,
c Nathans and Halpern 1953,
d Barber *et al.* 1955,
e Carver and Lokan 1957,
f Cook *et al*, 1956.

† Values for ^{40}A,

the order of 20 Mev, it could not be obtained in the way we have used just from the (γ, p) and (γ, n) cross sections for which the thresholds are at about 20 Mev. The values of r_0 which we obtain are in agreement with the values of about $1{\cdot}3 \times 10^{-13}$ cm obtained for the nuclei from C to Ca from electron scattering experiments (Hofstadter 1956). This success of the shell model in fitting the experimental harmonic mean energies for the photoabsorption cross sections shows that the shell model is capable of giving the energy difference between states belonging to different configurations.

A connection between these calculations and the effective mass concept of Van Vleck (1935), Bardeen (1937), Bruechner (1955) and others has been pointed out by Professor K. J. Le Couteur. The harmonic mean energy calculated for nucleons of mass M^* moving in an oscillator potential well with parameter a is $W_H = h^2/M^*a^2$. Thus by comparison with the formula for W_{H1}, the ratio of the effective nucleon mass to the free nucleon mass can be taken as

$$M^*/M = (1+\gamma_1 b)^{-1}.$$

This is about the same for all the nuclei considered here, being 0·6 for the Rosenfeld potential and 0·7 for the Serber potential. These values are comparable with those deduced from the variation of effective well depth with nucleon energy in the optical model of medium and heavy nuclei (Melkanoff *et al.* 1956). The corresponding quantity $(\frac{1}{2}+\gamma_2 b)^{-1}$ obtained from W_{H2} decreases as A increases, being 0·8 for ^{4}He, 0·6 for ^{7}Li, 0·5 for ^{16}O and 0·44 for ^{40}Ca for the Rosenfeld potential, and slightly larger for the Serber potential.

REFERENCES

BARBER, W. C., GEORGE, W. D., and REAGAN, D. D., 1955, *Phys. Rev.*, **98,** 73.
BARDEEN, J., 1937, *Phys. Rev.*, **51,** 799.
BRUECHNER, K. A., 1955, *Phys. Rev.*, **97,** 1353.
CARVER, J. H., and LOKAN, K. H., 1957, *Aust. J. Phys.* (to be published).
COOK, B. C., PENFOLD, A. S., and TELEGDI, V. L., 1956, *Phys. Rev.*, **104,** 554.
ELLIOTT, J. P., 1953, *Proc. Roy. Soc.* A, **218,** 345.
FERGUSON, G. A., HALPERN, J., NATHANS, R., and YERGIN, P. F., 1954, *Phys. Rev.*, **95,** 776.
FRANKEL, S., 1955, *Phys. Rev.*, **99,** 169.
HOFSTADTER, R., 1956, *Rev. Mod. Phys.*, **28,** 214.
LANE, A. M., 1953, *Proc. Phys. Soc.* A, **66,** 977.
LEVINGER, J. S., 1954, *Ann. Rev. Nucl. Sci.*, **4,** 13; 1955, *Phys. Rev.*, **97,** 122.
LEVINGER, J. S., and BETHE, H. A., 1950, *Phys. Rev.*, **78,** 115.
LEVINGER, J. S., and KENT, D. C., 1954, *Phys. Rev.*, **95,** 418.
MELKANOFF, M. A., MOSZKOWSKI, S. A., NODVIK, J., and SAXON, D. S., 1956, *Phys. Rev.*, **101,** 507.
NATHANS, R., and HALPERN, J., 1953, *Phys. Rev.*, **92,** 940.
PERRY, J. E., and BAME, S. J., 1955, *Phys. Rev.*, **99,** 1368.
ROSENFELD, L., 1948, *Nuclear Forces* (Amsterdam: North-Holland Publishing Company), p. 79.
VAN VLECK, J. H., 1935, *Phys. Rev.*, **48,** 367.
WILKINSON, D. H., 1955, *Proceedings of the* 1954 *Glasgow Conference on Nuclear and Meson Physics* (London and New York: Pergamon Press), p. 161.

A Study of Protons Emitted from Aluminium, Iron and Rhodium on Bombardment with Neutrons of 13·2 MeV†

By G. Brown,‡ G. C. Morrison,§ H. Muirhead and W. T. Morton
Department of Natural Philosophy, University of Glasgow

[Received April 18, 1957]

Summary

The angular distributions and energy spectra of the protons emitted, through the interaction of neutrons with an energy of 13·2 MeV with natural aluminium, iron and rhodium, have been studied using photographic emulsions. The experimental results have been compared with the predictions of a model which assumes that these protons can be emitted by two processes: by direct collisions of the incident neutron with a proton in the target nucleus and by the decay of a compound nucleus. Evidence for the process of direct interaction has been obtained in all cases.

§ 1. Introduction

In a previous paper from this laboratory (Morrison *et al.* 1953) on the interaction of high energy protons with the heavy nuclei (silver and bromine) of photographic emulsion, evidence was presented which strongly suggested that direct interaction was possible inside the nucleus between two nucleons of low energy. The observation of the direct emission of protons of low energy was confused, however, by the considerable number of evaporation protons emitted in the decay of the highly excited nuclei produced in that experiment. It was decided that a study of the interaction of nucleons of lower energy could provide more definite information concerning the probability of direct emission.

Paul and Clarke (1953) have made a survey of the cross sections for reactions of the type ${}_{Z}N^{A}(n, p\gamma)_{Z-1}N^{A}$ for neutrons with an energy of 14·5 MeV, and have shown that the cross sections are, in many cases, much larger than would be expected on the basis of the statistical theory of Weisskopf and Ewing (1940). These results have been interpreted by McManus and Sharp (1955) and by Brown and Muirhead (1957) as evidence for direct interaction of the incident neutron with the nucleons of the nucleus. Observations on the inelastic scattering of protons with energies of 18 MeV (Gugelot 1954) and of 31 MeV (Eisberg and Igo 1954) have indicated also that direct interaction as opposed to the immediate formation of a compound nucleus is of importance at intermediate energies.

---

† Communicated by Professor P. I. Dee, F.R.S.
‡ Now at Atomic Energy Group, G.E.C., Erith.
§ Now at A.E.R.E., Harwell.

Fig. 1

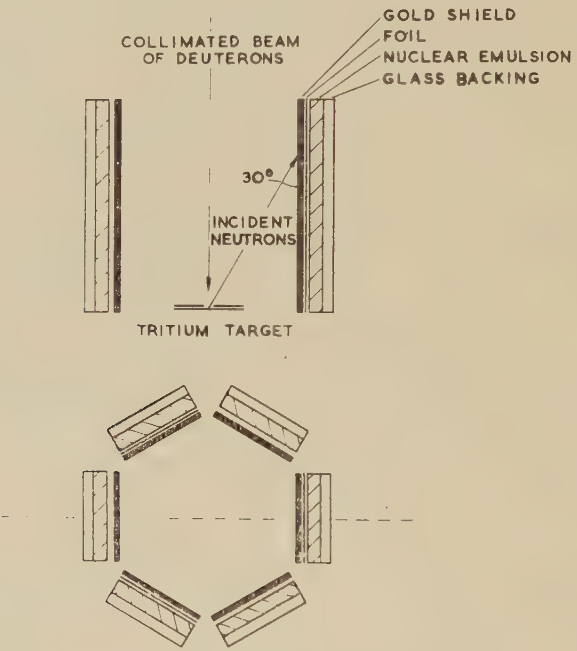

Schematic diagram of apparatus.

This paper describes a further investigation of the interaction of nucleons with nuclei at intermediate energies. The distributions in energy and angle of the protons emitted following the interaction of 13·2 MeV neutrons with aluminium, iron and rhodium have been obtained using photographic emulsions. A study of the (n, p) reaction in other elements is in progress.

§ 2. Experimental Procedure

2.1. *Exposure of the Plates*

The source of neutrons was the T(d, n)^{4}He reaction. The neutrons were produced by the bombardment of tritium, absorbed in a target of zirconium, with deuterons accelerated in the Glasgow H.T. set. Despite the intense flux of neutrons available from this reaction, the small cross section for the (n, p) reaction severely limits the possible geometry of an experiment in which observations are made on both the angular distributions and the energy spectrum of the protons.

In view of this consideration the scattering chamber shown in fig. 1 was constructed. The essential features are the following. Only a small portion of the tritium target, $\frac{1}{16}$ in. in diameter, was exposed to the beam of deuterons; thus the neutrons could be considered to arise from a point source. Collimation of the deuteron beam above the plate holder ensured that the deuterons were incident upon the uncovered portion of the tritium target. The scattering chamber was insulated from the H.T. set so that the integrated current of deuterons incident on the target could be measured.

Six nuclear emulsions (Ilford C2, 4 in. × 1 in. × 400 μ) were mounted hexagonally around this target. Foils, 4 in. × 1 in., of the element to be investigated were placed in contact with alternate emulsions. These foils and the surfaces of the other three emulsions were covered by gold strips of size 4 in. × 1 in. × 400 μ. The gold, which has a very small (n, p) cross section was used to shield the surface of the emulsion from external sources of protons.

Successive irradiations of iron, aluminium and rhodium foils were carried out in this arrangement. The time of each exposure was controlled by the current integrator.

2.2. *Examination of the Photographic Plates*

The photographic plates were examined in a region corresponding to neutrons incident at an angle of 30° ± 2°. For the exposures with foils of aluminium and iron, the area of emulsion examined on each plate was 6 mm × 0·3 mm; for rhodium the area examined on each plate was 6 mm × 0·6 mm. The energy of the neutrons incident over this area was calculated from the dynamics of the T(d, n)^{4}He reaction to be 13·2 ± 0·2 Mev.

The plates were examined with × 45 and × 90 oil immersion objectives and × 10 eyepieces for tracks of protons entering the surface of the emulsion[†]. Those tracks whose angle of dip was less than 30° in the case of the exposure to iron and less than 45° in the case of the aluminium and rhodium were selected for measurement. The limitation on dip angle ensured that nearly all tracks that started at the surface ended inside the emulsion. The position of the scan was such that measurements on protons making angles greater than 150° to the direction of the incident neutrons could not be made. Scanning was also carried out inside a known volume of emulsion for all protons that satisfied the same geometrical condition as imposed at the surface.

The range, the angle in the plane of the emulsion with respect to the direction of the incident neutron and the angle of dip were determined for every track selected. The daily variation of the thickness of the processed emulsion was taken into account in the computation of the angle of dip and the range. The energies of the protons were determined from their ranges in dry C2 emulsion (Rotblat 1951). The angles in space of the protons with respect to the direction of the incident neutron were calculated from their dips and projected angles.

[†] It was assumed that all tracks of unit charge were protons since it was impossible to separate protons and deuterons of low energy by grain counting in C2 emulsion. The validity of this assumption will be discussed in the presentation of the results.

§ 3. ANALYSIS

3.1. *Separation of Events*

Not all protons that were observed to start at the surface of the emulsion originated from the elements in contact with the emulsion. Protons starting in the emulsion within a distance of 1 or 2 microns from the surface are optically unresolvable from those entering the emulsion. Protons in this category were divided into two groups :

(1) recoil protons produced as a result of the collision of the incident neutrons of 13·2 MEV energy with hydrogen present in the emulsion.

(2) protons produced as a result of the interaction of the incident neutrons with the nuclei of the emulsion, or as a result of the collision of neutrons of lower energy with hydrogen atoms. These will be called background protons.

The recoil protons (1) were easily distinguished by applying the relationship

$$E_p = (13{\cdot}2 \pm 0{\cdot}2) \cos^2 \theta$$

where E_p=energy of the recoil proton and θ=spatial angle between the direction of the recoil proton and the direction of the incident neutron. Allowance was also made for the errors in the measurements of E_p and θ in the classification of recoil protons.

The correction for protons orginating from processes outlined in (2) was obtained from the measurements made on protons occurring inside the emulsion. Since the ratio of background to recoil protons starting at the surface and at points inside the emulsion should be the same, the number of surface tracks subtracted as ' background ' events was made proportional to that for protons identified as recoil tracks. The grouping of the subracted tracks in intervals of energy and spatial angle was made in the same relative numbers as those observed inside the emulsion.

The remaining surface protons could have arisen only in the materials placed in contact with the photographic emulsion. The effect of protons originating in the gold strip was eliminated by considering the energy and angle of the protons left (after subtraction of (1) and (2)) at emulsion surfaces in contact with the gold strips alone. Before subtraction from the data obtained on emulsions exposed to the foils, allowance was made for the form that this spectrum would take after the traversal of the foil.

The procedure described above may be conveniently summarized by the schematic equation

protons from foil = protons observed at the surface
− [(1) + (2) + modified protons from gold].

The number of tracks entering the various categories is shown in table 1.

Table 1

Element (angle of dip)	Protons observed	Recoils	Back-ground	Modified gold	Protons from Foil
Al (10°–45°)	1600	220	30	70	1280
Fe (10°–30°)	1190	200	55	50	885
Rh (10°–45°)	1140	490	60	90	500

3.2. *The Correction for the Energy Loss of Protons Produced in the Foil*

The thickness of the foils used in these investigations was 6, 13 and 12 mg cm^2 of aluminium, iron and rhodium respectively. However, the protons that were accepted for analysis had traversed the foil obliquely so that the effective thickness of a foil was greater than the figure quoted. A proton of 5 MEV energy that passes through a foil at an angle of dip of 30° loses an energy of 0·7, 1·2 and 1·0 MEV in aluminium, iron and rhodium respectively. The energy of a proton produced within a foil may therefore be considerably modified, particularly at low energy, by its passage through the foil to the surface of the emulsion. For this reason protons observed with angles of dip of less than 10° were discarded because of the large thickness of foil they might have traversed.

A relaxation method was adopted to correct for the energy loss of protons produced in a semi-thick target. This correction was applied for protons originating in the aluminium and iron foils. For rhodium the observed energy spectrum was simply corrected to half the thickness of the foil, since no protons were found to originate with an energy less than 4 MEV.

3.2. *The Determination of the Cross Section for the Emission of Protons*

The differential cross section, $(d\sigma/d\omega)_\theta$, for the emission of protons at an angle θ, may be related to the number of protons, $N_p(\theta)$, observed at an angle θ by the expression

$$N_p(\theta) = F(d\sigma/d\omega)_\theta d\Omega_\theta \, nV$$

where F = total flux of neutrons per cm^2 at the foil, $d\Omega_\theta$ = solid angle available for acceptance of a proton emitted at an angle θ, n = number of atoms per cm^3 of the foil, and V = volume of the portion of the foil under examination.

The total flux of neutrons incident on the foils in each exposure was determined by counting the number of recoil protons observed within a known volume of emulsion. The efficiency for detection of recoil tracks was estimated to be 80±10% by examination of the same volume of emulsion by different observers. The consequent error in the determination of the neutron flux, however, was only taken into account in the calculation of the total cross section for emission of protons, since the error was systematic and would not affect the relative differential cross sections..

The solid angle $d\Omega_\theta$ was restricted by the geometry of the exposure and the limitations imposed upon the angle of dip of the tracks selected for measurements. This solid angle was calculated and taken into account in the determination of the differential cross sections.

§ 4. RESULTS

The energy spectra, over the range from 0° to 140°, of the protons emitted from aluminium, iron and rhodium are shown in figs. 2, 3 and 4. The corresponding angular distributions for different ranges of energy are shown in figs. 5, 6 and 7. The total cross section for the emission of protons from each element was obtained by integration of the angular distributions extrapolated to 180°. The results are given in table 2 and compared with those obtained by other workers.

Table 2

Element	Cross section in millibarns				
	Nuclear emulsions			Activation methods	
	Present results	Allan	Present results corrected to n, pγ	Paul and Clarke	Forbes
^{27}Al	140±30	140	55±15	52±10	82±5
^{56}Fe†	120±30	190	120±30	97±12	124±12
^{103}Rh	25±5		11±3		

† A target of natural iron was employed in this experiment. To obtain the value quoted for ^{56}Fe a small background (~30 mb) due to the presence of ^{54}Fe (Allan, private communication) has been substracted from the observed cross section.

The nuclear reactions leading to the production of protons that can be induced by neutrons with an energy of 13·2 MeV can be represented schematically as follows :

$$
\begin{aligned}
{}_{Z}N^{A}+n \rightarrow\ & {}_{Z-1}N^{A}+p+\gamma && (a)\\
& {}_{Z-1}N^{A-1}+p+n && (b)\\
& {}_{Z-1}N^{A-1}+n+p. && (c)
\end{aligned}
$$

Fig. 2

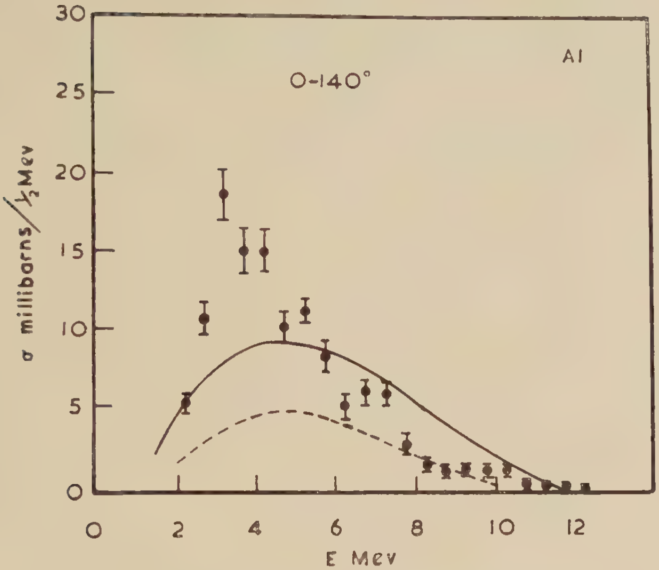

Energy spectra of protons from aluminium.

Fig. 3

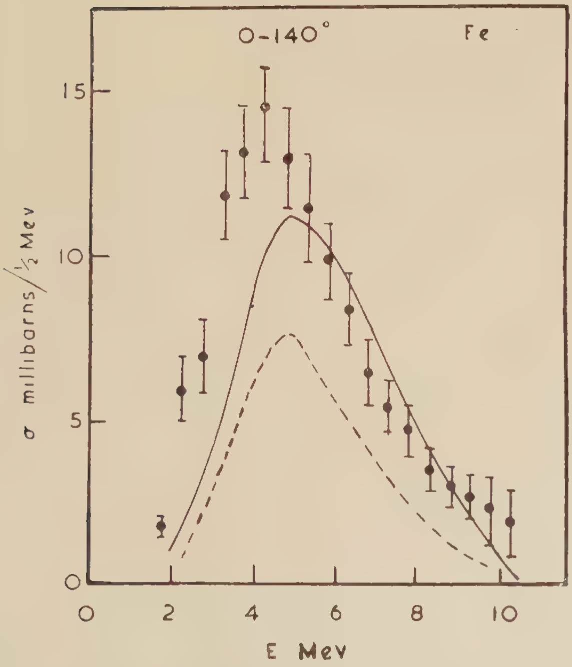

Energy spectra of protons from iron.

In the present experiment the sum of the contribution from all three reactions is observed. The processes (n, pp) and (n, d) are also energetically possible, but, due to the effects of the large negative Q-values

Fig. 4

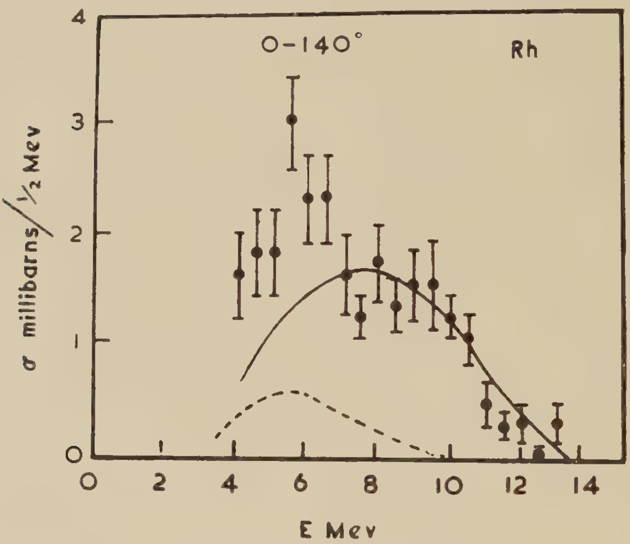

Energy spectra of protons from rhodium.

Fig. 5

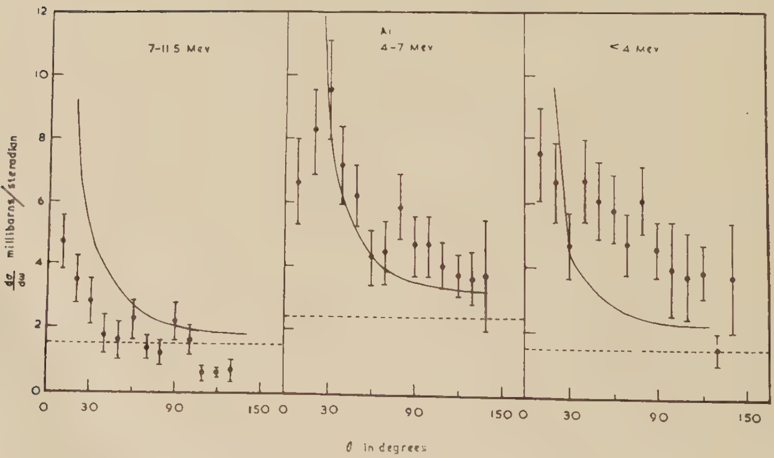

Angular distributions of protons from aluminium.

and the coulomb barrier are expected to make a negligible contribution to the observed data. If the reasonable assumption is made that the emission of a neutron normally accompanies that of a proton when the energy of the latter is less than $13{\cdot}2+q$ (where q represents the Q-value for the processes (b) and (c)) an estimate of the cross section for the process (a) can be made by integrating the observed spectrum for energies greater than this limit. The cross sections derived in this way are given in column 4 of table 2 and compare favourably with those obtained by measurements of the activity of the residual nucleus $_{Z-1}N^A$ (Paul and Clarke 1953, Forbes 1952).

Fig. 6

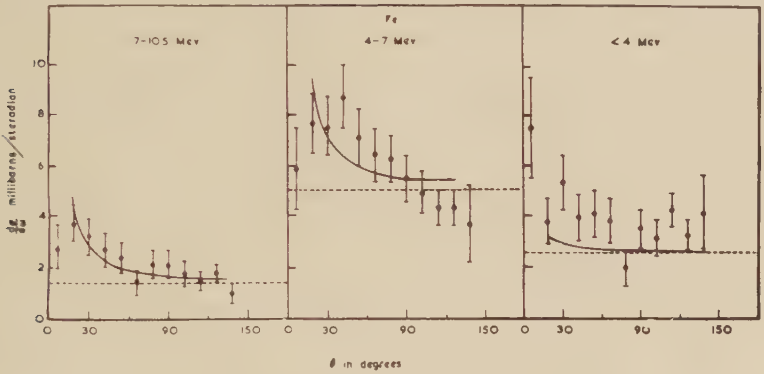

Angular distributions of protons from iron.

Fig. 7

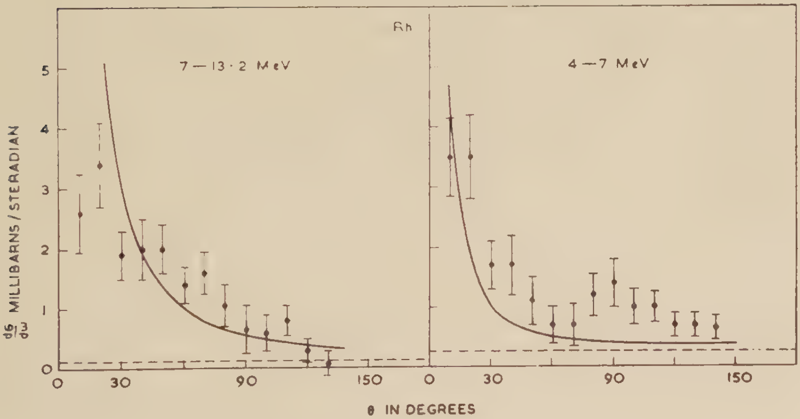

Angular distributions of protons from rhodium.

In the investigations of Allan (private communication), the angle of observation for protons emitted in the three reactions (a), (b) and (c) was 34°±20°. When account is taken of the forward peak in the angular distribution found in the present experiment the cross sections obtained by Allan would be reduced by about 20%.

§ 5. DISCUSSION OF RESULTS

The angular distributions at all energies show preferential emission of protons in the forward hemisphere. A similar trend in the angular distribution of the high energy protons emitted when ^{64}Zn is bombarded by neutrons with an energy of 14 Mev has been reported recently (Rosen, private communication). A preferential emission of this nature would be expected if some protons were emitted following the direct collision of the incident neutron with a proton inside the nucleus. The direct emission of protons should be enhanced relative to the emission from the decay of a compound nucleus for protons of high energy and nuclei of high atomic number. It can be seen that, experimentally, the lack of symmetry about the position of 90° is particularly evident for protons of high energy, and that it is greatest for rhodium.

It is of interest to compare the experimental results with the predictions of a simple model which takes into account both the direct emission and that from the decay of the compound nucleus (Brown and Muirhead 1957). This model assumes that nucleon–nucleon interactions can occur throughout the nuclear volume.

The magnitudes of the cross sections for the emission of protons in the reactions, ${}_{Z}N^{A}(n, p\gamma)_{Z-1}N^{A}$ and ${}_{Z}N^{A}(n, pn)_{Z-1}N^{A-1}$ have been calculated using this model. In table 3 the calculated cross sections, σ_p(dir), for the emission of protons by direct collision, and σ_p(comp) for the emission of protons by the decay of an excited nucleus are given.

Table 3

Element	Calculated cross section in millibarns			Experimental cross section in millibarns
	σ_p(dir)	σ_p(comp)	Total	
^{27}Al	80	70	150	140 ± 30
^{56}Fe	25	70	95	120 ± 30
^{103}Rh	20	5	25	25 ± 5

The calculated energy and angular distributions are shown in figs. 2–7; the broken line represents the cross section for the emission of protons from the decay of the compound nucleus, while the full curve is the sum of this cross section and that for the emission of protons by direct collision.

The apparent difference in the calculated and experimental energy spectra at low energies in aluminium can be mainly accounted for by considering the contribution of protons from the (n, np) reaction. The difference between the Q-values for the processes (n, np) and (n, 2n) may result in the favoured emission of protons over a limited region of the energy spectrum. This is indicated in table 4.

In the case of aluminium, therefore, the contribution is expected to be particularly important. In the case of iron and rhodium the effect is reduced considerably since there is no favoured emission of protons over the region of the observed energy spectrum.

§ 6. CONCLUSIONS

The present results for the total cross sections for the (n, p) reaction are in satisfactory agreement with those of other workers. Moreover, evidence for the process of direct interaction has been obtained in all cases from the angular distributions of the protons emitted in the (n, p) reaction.

It can also be seen that the application of the model, proposed by two of us (Brown and Muirhead *loc. cit.*), to the reactions studied leads to rough quantitative agreement with the experimental results. However, the theoretical model makes the extreme assumption that a nucleus may be treated as a Fermi gas, and that the detailed properties of an individual nucleus may be ignored. Thus it is not surprising that detailed comparisons do not show more than semi-quantitative agreement. Further defects of this model are the neglect of conservation laws other than those for energy and linear momentum, and the over simplification of the problem of transmission at the nuclear surface.

Table 4

Element	*Q*-values in MEV		Maximum proton energy from (n, np) in MEV	Energy limits for favoured proton emission in MEV
	n, np	n, 2n		
^{27}Al	—8·3	—13·0	4·9	0–4·7
^{56}Fe	—10·2	—11·2	3·0	0–1·0
^{103}Rh	—6·5	—9·4	6·7	0–2·9

The possibility of the enhanced production of protons at the nuclear surface also should be considered (Austern *et al.* 1953). Conservation of angular momentum, which is taken into account in this theory, could then impose more stringent conditions on the angular distributions of the outgoing protons than is assumed in the present model of volume production. Unfortunately this theory does not yield absolute cross sections.

It can be seen, therefore, that there is a need to improve the theory of nuclear reactions in the intermediate energy region. It must also be pointed out that considerable refinements are required for the experiments performed in this energy range. None of the experiments so far reported for examining the (n, p), (n, n) or (p, n) processes could have detected satisfactorily the existence of discrete states superimposed on a continuum as suggested by the experiments of Gugelot (1954) on the inelastic scattering of protons. Thus considerable improvement in the energy resolution should be sought in future experiments in this field.

ACKNOWLEDGMENTS

The authors wish to thank Professor P. I. Dee for his interest and encouragement during the course of this work, and are deeply indebted to Drs. W. M. Deuchars and A. M. Ward for their advice and help during the exposures at the H.T. set.

REFERENCES

AUSTERN, N., BUTLER, S. T., and McMANUS, H., 1953, *Phys. Rev.*, **92,** 351.
BROWN, G., and MUIRHEAD, H., 1957, *Phil. Mag.*, **2,** 473.
EISBERG, R. M., and IGO, G., 1954, *Phys. Rev.*, **93,** 1039.
FORBES, S. G., 1952, *Phys. Rev.*, **88,** 1309.
GUGELOT, P. C., 1954, *Phys. Rev.*, **93,** 425.
McMANUS, H., and SHARP, W. T., 1955, *Statistical aspects of the nucleus*, B.N.L. Report, 68.
MORRISON, G. C., MUIRHEAD, H., and ROSSER, W. G. V., 1953, *Phil. Mag.*, **44,** 1326.
PAUL, E. B., and CLARKE, R. L., 1953, *Canad. J. Phys.*, **31,** 267.
ROTBLAT, J., 1951, *Nature, Lond.*, **167,** 550.
WEISSKOPF, V. F., and EWING, D. H., 1940, *Phys. Rev.*, **57,** 472.

Observations on Extensive Air Showers
I. Apparatus†

By T. E. Cranshaw and W. Galbraith
Atomic Energy Research Establishment, Harwell

[Received March 21, 1957]

§ 1. Introduction

An arrangement of Geiger–Muller (G.M.) counters, covering an area of approximately 0·5 km², together with other apparatus, has been set up at Culham (alt. 60 m) near Harwell, to study various aspects of extensive air showers.

The results of the investigations will be given in a series of papers, and this is intended to be an introduction to the series. It contains a general description of the apparatus used, and also includes in Appendices details of some of the electronic circuits which may be of interest to other workers in this field. Specialized apparatus for particular experiments will be described in the appropriate papers.

§ 2. Lattice Arrangement of G.M. Counters

As in an earlier Harwell experiment (Cranshaw and Galbraith 1954) G.M. counters on a lattice are used to detect the arrival of extensive air showers. The arrangement is shown in fig. 1, and fig. 2 gives a block

Fig. 1

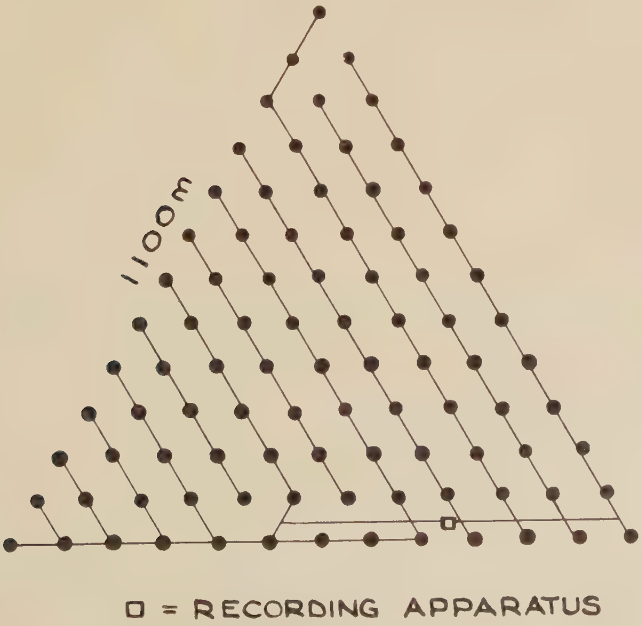

---

† Communicated by the Authors.

diagram of the apparatus. At each of the ninety-one points in fig. 1 there is a G.M. unit containing three counters, two of area 200 cm^2 (Cintel G.M. 1A4) and a smaller 15 cm^2 counter (G.M. 4A4). The distance between units is 90 metres, and the area covered is an equilateral triangle of area 0·5 km^2. The shape of the lattice was dictated by the area available, but it is also convenient for calculation.

Each G.M. unit contains the following electronic circuits.

(*a*) A quench circuit for each counter which lowers the E.H.T. on the counter below the threshold for a period of 2 msecs after a discharge†. Details of this circuit are given in Appendix I.

(*b*) A conventional Rossi coincidence circuit for the two large counters with a resolving time of 3 μsecs.

(*c*) Two blocking oscillator circuits for sending pulses ' a ' and ' b ' from the units to the recording centre at X, fig. 1.

The ' a ' pulses are triggered by the coincidences between the two large counters. The counting rate of a single counter is about 500/min, and the rate of coincidences about 3/min. The ' b ' pulses are triggered by the small counter, and the rate is about 10/min. The blocking oscillator delivers a balanced pulse of 40 μsecs duration through a transformer into unscreened P.V.C.-insulated flex. The pulse amplitude is about 30 volts and the impedance of the line is about 120 Ω. At X, another transformer converts the balanced pulse into a pulse of single polarity with an amplitude of approximately 50 volts. Pick up between one G.M. unit and another, or between blocking oscillators within the same unit due to sending the pulses along the long lengths of unscreened flex is negligible.

Fig. 2

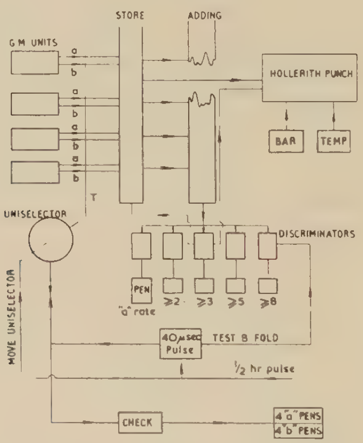

---

† At first, a shorter quench time of 80 μ secs was used. The occurrence of multiple pulses in some counters after a few months' operation led us to increase the quench time. No trouble has been encountered since then.

To test this point, a pulse generator was set up near the centre of the array, and leads taken to each of sixteen units so that any combination of the units could be triggered simultaneously. Several test patterns were tried, and were always registered correctly.

The positive and negative H.T. supplies and the E.H.T. supply for the counters are separately derived at each unit, and the power for the whole lattice is provided by a 500 cycle generator stabilized at 240±1 volts. No attempt has been made to control the temperature of the units, because the counters quenched with ethyl formate operate satisfactorily over the temperature range encountered in this country.

§ 3. RECORDING APPARATUS

The basic circuit used to record the showers is shown in fig. 3. There is one such circuit for each G.M. unit. In the pulse adding circuit, the 'a' pulses from each unit are arranged to cut off the current through one of ninety-one triodes, whose anodes are connected together. (The series germanium diode has the same bias on it as the triode, and prevents small pulses picked up on the cables from appearing in the added-up pulses.) This current is arranged to flow through a common 5 kΩ resistance, across which it develops a pulse of about ten volts. Discriminators set at suitable bias levels select showers which discharge 2, 3, 5 and 8 or more G.M. units within the resolving time of about 40 μsecs. Further details of these circuits are given in Appendix II.

Fig. 3

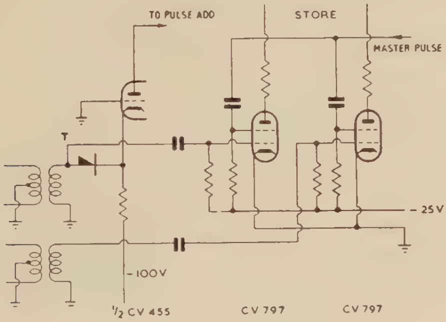

The rate at which showers arrive is recorded by photographing every hour in solar and sidereal time a bank of Post Office registers driven from the discriminators. Two rows of lights photographed at the same time give the barometric pressure and the air temperature on the roof of the building, from which the dependence of the shower rates on these two variables can be determined.

For some experiments, we need to know not only how many, but also which G.M. units have been discharged. A standard automatic punch

(Hollerith type) was adapted to display this information on a punched card. When a coincidence is observed, the information is stored on miniature thyratrons, type CV797 (see fig. 3). These thyratrons have two grids, both of which must be near earth potential for a discharge to occur. A master pulse derived from the 3-fold discriminator† is applied to the first grid of all the thyratrons, and an ‘ a ’ or ‘ b ’ pulse is applied to the other. Then after an event in which three or more ‘ a ’ pulses are produced, there will be at least three ‘ a ’ thyratrons and possibly some ‘ b ’ thyratrons in the conducting state. A relay circuit designed for us by R.C.M. Barnes is then brought into operation by the moving contact of the Hollerith machine, and selects all the thyratrons in turn. If the thyratron is conducting, an appropriate hole is punched in the card. When all the thyratrons have been selected, another relay momentarily breaks the H.T. lead to the thyratron anodes so that they are ready for the next event. Each shower is recorded on a separate card.

Fig. 4

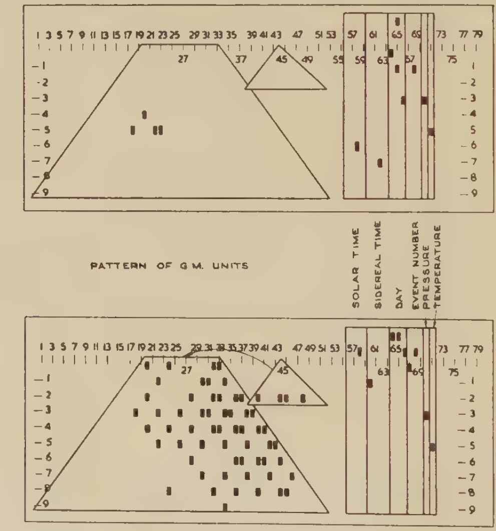

Additional information is punched giving the time to the nearest half-hour, the number of the events in the day, the barometric pressure, air temperature, and sometimes information from other apparatus. This hodoscope unit has operated reasonably well, and the punched cards are very convenient for examination and analysis. Figure 4 shows two cards as examples. The first card shows a typical three-fold shower, in which three ‘ a ’ pulses and one ‘ b ’ pulse were recorded. The second card shows the largest shower so far recorded.

---

† About one-third of two-fold events are due to random coincidences, and it is not worth while to record these on the cards.

§ 4. CHECK ON THE CORRECT OPERATION OF THE APPARATUS

One of the main objectives of the experiment requires reliable and continuous operation of the apparatus over long periods. Continuous checking was therefore carried out in the following ways.

(*a*) The total rate of ' a ' pulses from all ninety-one units is recorded on a chart. Under normal conditions the total ' a ' rate is 250 counts/min.

(*b*) The ' a ' pulses, and every tenth ' b ' pulse from each of four G.M. units, are recorded on multi-pen charts for periods of half an hour. In successive half-hours, four different units are selected, and in this way the whole lattice array is checked twice a day. The pulses are taken from the point T (figs. 2 and 3) and are fed through a test unit which rejects all pulses which have less than a certain amplitude and width. The selected values are 30 volts and 30 μsecs. In this way, it is easy to identify units in which the pulse shape has deteriorated.

(*c*) The pulse adding circuits and the thyratron storage circuits are also checked in sequence at every half-hour interval. A test pulse is applied (again at the point T) to four ' a ' channels and the corresponding ' b 's, and also to another four ' a ' channels alone. A relay circuit is arranged to check that the 8-fold discriminator has been triggered, and then a test card with an easily recognized pattern is produced indicating that twelve thyratron circuits have operated. Thus test (*b*) checks the apparatus up to the point T, and (*c*) checks beyond T.

APPENDIX I

Quench Circuit

It is well known that the performance of Geiger counters can be greatly improved by external quenching. In order that the greatest benefit should be obtained, it is essential that the voltage should be lowered as early as possible in the discharge, which requires that the trigger circuit should be sensitive (Elliot 1949). With most designs of trigger circuit, this conflicts with interchangeability of valves and components, because the valves are being operated on a part of their characteristics which is particularly sensitive to manufacturing tolerances, and to ageing (Cooke-Yarborough *et al.* 1949). In the present experiment, these difficulties have been largely overcome by making use of the properties of the diode in the negative field region, as discussed by Kandiah (1954).

The circuit is shown in fig. 5. It will be seen that both halves of the double triode are on the working part of their characteristics, some asymmetry being introduced in the cathode circuit only to increase the size of quench pulse. The loop gain in the circuit is kept below unity by the impedance of the diode. The value of this impedance, and therefore the pulse required to trigger the circuit, can be controlled by the current through the diode, i.e. by the choice of R. With R fixed, C can be chosen to give the required quench time. In our case $R=1M$, $C=0{\cdot}003\,\mu$F. The circuit is extremely sensitive, but to a great extent independent of valve characteristics.

Fig. 5

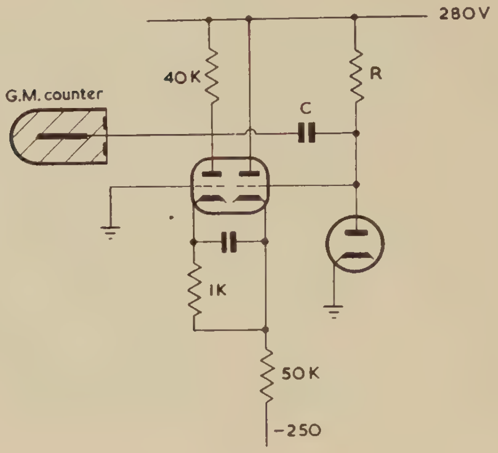

APPENDIX II

Pulse Adding Circuits

The pulse adding circuit is shown in fig. 6. The total current through the triodes is 180 mA. This current is carried by the 500 Ω resistor. The anodes are also connected via a condenser to the cathode of a CV2127, which is passing 30 mA, and is connected in a voltage stabilizer type of circuit, i.e. the impedance at its cathode is approximately $1/g_m G$ where g_m is the mutual conductance of the CV2127, with 5 kΩ in the anode, and G is the gain of the CV138 stage. Thus the impedance is about 10 Ω, and any current changes in the cathode circuit change the cathode potential by very small amounts. Therefore, when the current through the triodes is changed by cutting off some of them by ' a ' pulses, about 2%

Fig. 6

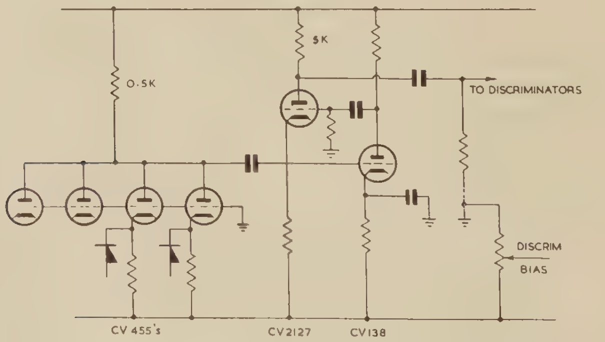

of the current flows through the 500 Ω anode load, the remainder flows in the cathode circuit of the CV2127, and then develops a pulse across the 5 kΩ resistor in its anode.

The current in the CV455's is fixed to within about 1% by the negative line voltage E_{neg} and the wire wound 0·1% tolerance resistor Rc. The pulse developed at the anode of the CV2127 by cutting off $n\frac{1}{2}$CV455's is thus $nE_{\mathrm{neg}}Ra/Rc$. By deriving the bias for the discriminators from a potential divider across E_{neg} to earth, the setting of the discriminators is essentially independent of the value of E_{neg}, and only dependent on the ratio of wire wound resistors. Consistent discrimination between 7-fold and 8-fold coincidences has been achieved for two years' operation.

ACKNOWLEDGMENTS

We would like to thank the following at A.E.R.E. whose help at different stages was invaluable to the setting-up of the experiment : Mr. A. J. McIntyre and his group for the layout and wiring of the G.M. counter lattice ; Mr. C. Lomas and the wiring pool for making the electronic units for the lattice ; Mr. P. R. Robinson, Mr. A. C. Sherwood, Mr. A. G. Parham and others in our group for making and installing much of the electronic apparatus in the control room.

We are grateful to our group leader, Mr. W. J. Whitehouse for many helpful discussions, particularly when ideas were first being formulated about the experiment, and we thank Dr. E. Bretscher, Head of Nuclear Physics Division, for encouragement in this work. Finally we wish to thank the Admiralty for facilities to do this experiment on their land.

REFERENCES

CRANSHAW, T. E., and GALBRAITH, W., 1954, *Phil. Mag.*, **45,** 1109.

KANDIAH, K., 1954, *Proc. Instn elec. Engrs*, **101,** pt. II, no. 81.

ELLIOT, H., 1949, *Proc. phys. Soc. Lond.*, A, **62,** 369.

COOKE-YARBOROUGH, E. H., FLORIDA, C. D., DAVEY, C. N., 1949, *J. sci. Instrum.*, **26,** 124.

Observations on Extensive Air Showers
II : Time Variations in the Energy Region of 10^{17} eV†

By T. E. Cranshaw and W. Galbraith
Atomic Energy Research Establishment, Harwell

[Received March 31, 1957]

Abstract

The rates of arrival of extensive air showers near sea level have been recorded over a period of almost two years. The results show no evidence for sidereal variations in the rates, and the bearing of this in theories of the origin of cosmic radiation is discussed. Evidence is presented of statistically significant variations in solar time for showers containing a mean number of particles of 3×10^7, and the significance of this is briefly discussed.

§ 1. Introduction

Extensive air showers afford the only means of recording the arrival of primary cosmic ray particles of the highest energies. Previous experiments in this field have shown that the rays exhibit a remarkable degree of isotropy up to energies of at least 10^{16} ev. Evidence for a small but none-the-less persistent variation in sidereal time comes from the work of Auger *et al.* (1955) at lower energies (10^{14}–10^{15} ev), and is supported to some extent by the early observations of Citron and Kehler (1955). Later observations by Citron (private communication) have not supported these results and the sum total of events over a period of two years do not show any significant sidereal effect. The amplitude of Auger *et al.*'s effect is only a fraction of 1%, but it exhibits maxima when the plane of the galaxy passes the zenith at the latitude of observation. If one attributes their variation to the distribution of cosmic ray sources about the galactic plane, a more striking effect might be expected to show up at southern latitudes where the centre of the galaxy passes more directly overhead. Farley and Storey (1954) reported a variation with an amplitude of about 1% in the rate of showers of about the same energy recorded at Auckland, New Zealand, and the period of the maximum agreed satisfactorily with the time of transit of the galactic centre. However, further observations in Auckland (Farley, private communication) appear to show no significant effect to support the earlier published result.

At higher energies, we reported (Cranshaw and Galbraith 1954) an experiment at Harwell which seemed to indicate a variation of about

---

† Communicated by the Authors.

5% at an energy then estimated to be about 5×10^{16} ev, although no variation greater than 0·6% could be found at 10^{16} ev, and at higher energies there were insufficient counts to reveal any variation less than 13%. Recent work suggests that the data used to estimate the energy in these experiments resulted in an overestimate by a factor of 2 or 3. It is clear however that at energies up to 10^{16} ev, any variations that may exist are less than 1%, and are too small for present experiments to demonstrate them beyond question. The great importance of these results to astrophysics has led to experiments at higher energies.

Table 1

	Shower size	Mean number of particles	Rate per day	Proby. on χ^2 test	Diurnal term			Semi-diurnal term		
					% Amp.	ϕ	Proby.	% Amp.	ϕ	Proby.
Sidereal time	3-fold	$5{\cdot}7 \times 10^6$	$70{\cdot}0 \pm 0{\cdot}37$	0·9	0·14	–	0·84	0·82	–	0·53
	5-fold	$1{\cdot}4 \times 10^7$	$14{\cdot}5 \pm 0{\cdot}17$	0·9	1·92	–	0·51	2·6	–	0·29
	8-fold	$2{\cdot}7 \times 10^7$	$3{\cdot}72 \pm 0{\cdot}09$	0·7	0·17	–	0·99	4·0	–	0·45
	20-fold	10^8	$0{\cdot}38 \pm 0{\cdot}03$	–	8·3	–	0·76	15·0	–	0·41
Solar time	3-fold	$6{\cdot}7 \times 10^6$	as above	0·30	2·5	213	0·005	1·0	66	0·40
	5-fold	$1{\cdot}4 \times 10^7$		0·13	4·5	242	0·03	4·5	49	0·03
	8-fold	$2{\cdot}7 \times 10^7$		0·01	9·8	216	0·01	13·0	65	0·003
	20-fold	18^8		–	21·0	188	0·18	6·3	–	0·86

Evidence for a variation in rate of showers of energy 10^{17} ev has been presented by Crawshaw and Elliot (1956). However, in this experiment, the rate showed a marked diurnal variation in solar time, and no significant variation in sidereal time. Variations in solar time with a large semi-diurnal component have been reported by McCusker and Wilson (1956) in the rate of dense air showers (>700 particles/m^2) and also of penetrating showers.

This paper gives the results of the observations on air showers made at Culham in the period December 1954–October 1956 using the apparatus described in paper I. We have found no evidence for any variation in sidereal time, but in solar time the results suggest a variation which is mainly semi-diurnal, and may have some relation to McCusker's. Variations of rate of high energy events in solar time are so unexpected that we feel inclined to treat them with suspicion. Nevertheless, they have now been reported in several experiments, and we feel it desirable to report our results in some detail. We also discuss the significance of the absence of sidereal variations.

§ 2. ANALYSIS OF RESULTS

The number of showers discharging n or more G.M. units, with $n = 3$, 5 and 8, in hourly intervals throughout the solar and sidereal day, was obtained from the photographic records of mechanical counters actuated by discriminators biased for the appropriate shower sizes. Following the nomenclature of paper I, an event of type n fold or greater, corresponds to showers which have discharged the two 'a' counters in each G.M. unit, n or more units being involved. According to paper III, we estimate the mean number of particles in the showers detected to be those given in table 1. The results of adding the counts over the whole period are shown in fig. 1.

Fig. 1

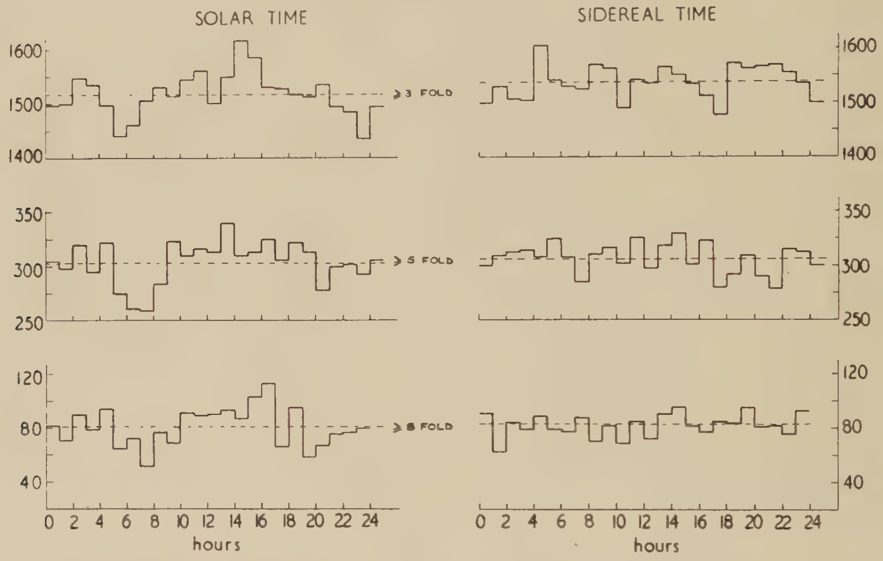

The data have been analysed in the following way. We first suppose that the counts simply obey a Poisson distribution, i.e. that the probability of obtaining a count is independent of time. Two tests of this random hypothesis are made. Firstly χ^2 is calculated for the hourly totals about the mean value, and the results of this analysis are given in table 1. As seen there, the only set of observations which is not in reasonable agreement with the hypothesis is that for the $\geqslant$ 8-fold events in solar time. Secondly, we calculate the amplitudes and phases of the harmonic components present in the data by calculating the best sine waves through 24 and 12 points for the diurnal and semi-diurnal data respectively, and estimate the probability P that such amplitudes should arise on the random hypothesis, using the method of Chapman and Bartels (1951). The statistical significance of the result is then given by

$$P = \exp\left(-\epsilon^2 \Sigma/4\right)$$

where ϵ is the fractional amplitude of the sine wave and Σ is the total number of counts in the data. The results of this analysis are given in table 1.

An analysis of the hodoscope records enabled us to select large showers ($n \geqslant 20$). In those cases where the shower fell near the edge of the array, we estimated how many units might have been discharged if the lattice had been infinite in extent, and so added such events to the category of 20-fold or greater. The results of a harmonic analysis of this data is also given in table 1.

It is clear from the results of our analysis that there is no evidence for any variation in the shower rates in sidereal time. The statistical accuracy of the results is such that, setting $P=0{\cdot}1$ in the above equation as our criterion of significance, we would not consider the variation as significant unless its amplitude exceeded 7% for the $\geqslant$ 8-fold events and 25% for the $\geqslant$ 20-fold events. In solar time, however, there appears to be a semi-diurnal variation in the rate of showers discharging 8 or more units, the amplitude being about 13% and the time of the maxima being at 02.30 and 14.30 hr. The diurnal component also present has an amplitude of 9% with a maximum at 15.30 hrs.

§ 3. MAGNETIC RIGIDITY OF PRIMARY PARTICLES

It was pointed out earlier (Cranshaw and Galbraith 1954) that any anisotropy present in the primary cosmic rays would have to be considered in terms of galactic structure, and the interstellar magnetic field. The magnetic rigidity $H\rho$ of the primary particles therefore plays an important part in their motion, and for a particle of charge Z and total energy E moving across a magnetic field of strength H is given by

$$H\rho=E/300Z \text{ gauss cm.}$$

For our largest showers ($\geqslant$20-fold events) we have estimated (paper III) that the mean shower size is about 9×10^7 particles, which corresponds to a primary energy $E_0\sim5\times10^{17}$ ev, if the initiating particle is a single proton. The value of $H\rho$ for this particle is then $1{\cdot}5\times10^{15}$ gauss cm. If, however, we suppose the incoming particle is a nucleus of iron, making its first collision at the same height as the proton, the number of shower particles per nucleon of the primary is $1{\cdot}6\times10^6$, and allowing for the increase in energy per shower particle as primary energy decreases (Greisen 1956), the primary energy per nucleon is then $\sim1{\cdot}6\times10^{16}$ ev making $E_0\sim9\times10^{17}$ ev. In fact, a heavy nucleus makes its first interaction higher on average than a proton, so that the energy per shower particle is higher in showers produced by heavy nuclei than in showers produced by protons. Thus even for heavy nuclei, a minimum value of $H\rho$ is about $1{\cdot}5\times10^{14}$ gauss cm.

§ 4. DISCUSSION

4.1. *Absence of Sidereal Variation*

We wish to discuss this result in the light of theories of the origin of cosmic rays.

Following Morrison *et al.* (1954) we define δ, the anisotropy, as $2(J_{\max}-J_{\min})/(J_{\max}+J_{\min})$ where $J_{\max}$ and $J_{\min}$ are the maximum and minimum values of the flux We can set an upper limit to δ by choosing a reasonable value o P in the probability expression (§ 2). We have taken $P=0{\cdot}1$. Then with the numbers of counts, Σ, in the experiment, we arrive at the values of ϵ and hence δ given in table 2. These values then represent fairly generous upper limits to the anisotropy which can be supposed to exist undiscovered by the experiment.

Following Cocconi (1956) we also show in this table the total path length, L_{total}, which protons of these energies would have if they diffused for a sufficient time in a spherical galaxy to acquire the isotropy determined by δ, and the estimated maximum path length L_{max} before escape from the galaxy. As can be seen, the path length requirements to account for the observed isotropy are about equal to or exceed the diffusion path lengths in the galaxy. This means that even in a spherical galaxy containing diffusing elements, protons are hardly retained within the galaxy for a time long enough to render them sufficiently isotropic at the earth. This argument is even more forceful when applied to a flatter disc-like galaxy.

Table 2

E_0 ev for primary protons	$\epsilon=0{\cdot}5\delta$	L_{total} cm	L_{max} cm
3×10^{16}	0·015	$1{\cdot}5\times10^{24}$	2×10^{24}
10^{17}	0·07	3×10^{23}	6×10^{23}
5×10^{17}	0·25	10^{23}	10^{23}

A similar conclusion may be reached by considering the motion of particles within a spiral arm of the galaxy in a magnetic field of $5\times10\ ^{6}$ gauss. We have shown in § 3 that the radius of curvature of a proton of 5×10^{-17} ev (the energy of the largest showers, $\geqslant$20-fold events) would be 3×10^{20} cm, which is approximately equal to the radius of the spiral arm containing the solar system. Thus it is difficult to see how primary protons of this energy could be accelerated and then be retained for long enough to acquire isotropy.

The results of the present experiment therefore favour the suggestion put forward recently by Cocconi (1956) and Farley (1956) that the highest energy particles, if protons, have an extra-galactic origin. The situation for galactic origin is only slightly easier if the incoming particles are iron nuclei, for as we have shown, their radii of curvature would be smaller than that of protons by less than an order of magnitude.

4.2. *Evidence for Solar Effects*

We wish now to discuss the evidence for solar variations in showers which discharge 8 or more G.M. units and make some comparisons with other recent experimental work.

The data contained in fig. 1 have been divided into periods of about 1 month and the harmonic components calculated. These are shown in fig. 2 on a harmonic dial, each dot representing the amplitude and phase of the wave for each month. The radii of the circles are chosen so that if the scatter of the points is due to statistical fluctuations only, 39% of the points would be expected to lie within the inner circle, and 90% within the outer circle.

It will be seen that the amplitude and phase of the diurnal component (fig. 2(*a*)) varies considerably from month to month, four of the seventeen points lying outside the 90% circle. A similar erratic variation was observed by Crawshaw and Elliot.

Fig. 2

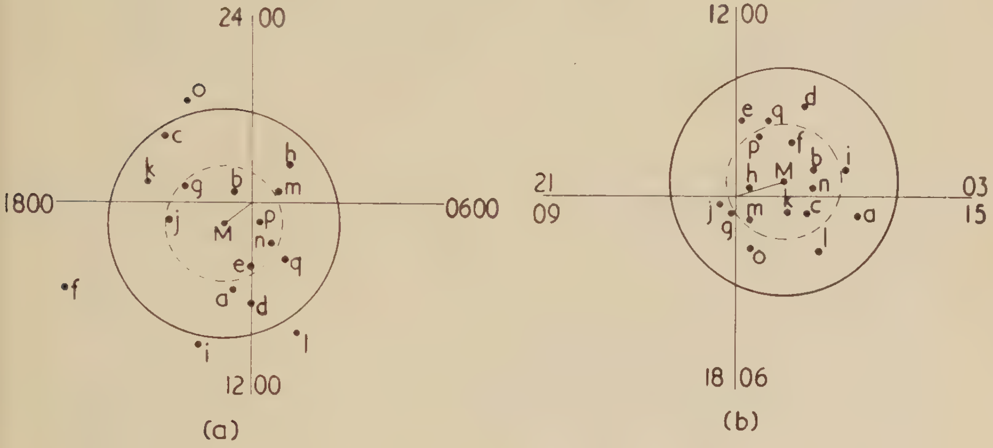

Approximate dates, 1955 : a March, b April, c June, d August, e September, f October, g December ; 1956 : h January, i February, j March, k April, l May, n July, o August, p September, q October.

On the other hand, in our experiment the semi-diurnal vectors (fig. 2(*b*)) show a variation which may be reasonably regarded as a statistical fluctuation from the resultant vector **M**, the amplitude of which is 13%. This is larger than in Crawshaw and Elliot's experiment, where the semi-diurnal term is about 3%.

McCusker and Wilson have considered the possibility that the variations observed in their experiments may be connected with the semi-diurnal pressure oscillations in the atmosphere. The times of the maxima in the rate of high density showers agree well with the pressure maxima, and the rate of local penetrating showers appears to be in antiphase with these maxima. In the present experiment, the times of minimum rate coincide with the times of pressure maxima.

McCusker and Wilson point out that the variation in rate cannot be due simply to variations in the amount of air above the apparatus, since they obtain the usual value for the barometer coefficient when short term variations are considered. The same argument applies here. To obtain a significant change of rate at sea level from a change in the distribution of the air above the apparatus appears to require primaries with a very large interaction cross section, larger even than that of heavy nuclei. Alfven (1954) has suggested that the highest energy primaries might be relativistic dust grains. The behaviour of such particles on entering the atmosphere cannot be predicted with certainty, but the lateral structure of air showers does not favour this hypothesis (Herlofson 1956, and paper IV).

We have as yet no explanation to offer for the variations in solar time.

ACKNOWLEDGMENTS

We are very grateful to Mrs. S. A. Norris and Mr. A. G. Parham for their help in recording and in analysing the data of this experiment.

REFERENCES

ALFVEN, H. 1954, *Tellus*, **6,** 232.
AUGER, P., CACHON, A., DAUDIN, A., FREON, A., and MOSZKOWSKI, C., 1955, *C.R. acad. Sci.*, **240,** 2407.
CHAPMAN, S., and BARTELS, J., 1951, *Geomagnetism* (Oxford), Vol. II.
CITRON, A., and KEHLER, P., 1955, *Proceedings of the Guanajuata Conference*, Mexico. In press.
COCCONI, G., 1956, *Nuovo Cim.*, **3,** 1433.
CRANSHAW, T. E., and GALBRAITH, W., 1954, *Phil. Mag.*, **45,** 1109.
CRAWSHAW, J. K., and ELLIOT, H., 1956, *Proc. Phys. Soc. Lond.* A, **69,** 102.
DARDIS, J. G., MCCUSKER, C. B. A., and WILSON, B. G., 1955, *Proc. Phys. Soc. Lond.* A, **68,** 585.
FARLEY, F. J. M., 1956, *Proceedings Oxford Conference*, April 1956, Ed. T. E. Cranshaw, A.E.R.E. Publication.
FARLEY, F. J. M., and STOREY, J. R., 1954, *Proc. Phys. Soc. Lond.* A, **67,** 996.
GREISEN, K., 1956, *Progress in Cosmic Ray Physics*, Ed. J. S. Wilson.
HERLOFSON, N., 1956, *Proceedings Oxford Conference*, April 1956, Ed. T. E. Cranshaw, A.E.R.E. Publication.
MCCUSKER, C. B. A., and WILSON, B. G., 1956, *Nuovo Cim.*, **3,** 188.
MORRISON, P., OLBERT, S., and ROSSI, B., 1954, *Phys. Rev.*, **94,** 440.

The Specific Heats and Magnetic Susceptibilities of Alloys of Cerium with Lanthanum at Low Temperatures†

By Lois M. Roberts and J. M. Lock
Royal Radar Establishment, Gt. Malvern, Worcs.

[Received March 13, 1957]

Abstract

Specific heat measurements between 1·5°K and 20°K, and magnetic susceptibility measurements between 1·5°K and 290°K have been made on four alloys containing respectively 78·9%, 37·6%, 27·0% and 5·03% by weight of cerium in lanthanum. Comparison is made with similar previous measurements on pure cerium. The single anomaly in the specific heat of pure cerium at 12·3°K splits into two in the alloys, and as the dilution is increased these anomalies move to lower temperatures. The lower of the two only is accompanied by a change in the magnetic properties, a maximum occurring in the susceptibility of the most concentrated alloy and temperature-independent paramagnetism setting in suddenly in the next two. In the most dilute alloy the anomalies in both the specific heat and in the susceptibility appear to have moved to temperatures below 1·5°K. Above 80°K the magnetic susceptibilities of all the alloys obeyed a Curie–Weiss law, $\chi = C/(T-\theta)$. The Curie constant C varied smoothly from $56{\cdot}1 \times 10^{-4}$ e.m.u./g Ce for the most concentrated alloy (cf. $55{\cdot}3 \times 10^{-4}$ e.m.u./g for pure cerium) to about 140×10^{-4} e.m.u./g Ce for the most dilute alloy.

As in pure cerium, anti-ferromagnetism is believed to be the explanation of the anomalous magnetic behaviour of the alloys. However, the double specific heat anomalies in the latter suggest that the ordering of the 4f electronic orbitals takes place in two stages, while the temperature-independent paramagnetism of the more dilute alloys may be the consequence of freedom of the direction of magnetic ordering to orient itself perpendicular to the applied field. The increase in the Curie constant suggests that the population of the 4f shell increases, with dilution of the alloys, to 2 or 3 electrons per atom of cerium.

§ 1. Introduction

Previous measurements on cerium (Parkinson *et al.* 1951, Parkinson and Roberts 1957, Lock 1957, referred to hereafter as PSS, PR and L respectively), have suggested that its anomalous behaviour below 20°K is due to anti-ferromagnetic interactions associated with the 4f shell of electrons. In order to investigate the effect of magnetic dilution on these interactions, specific heat and magnetic susceptibility measurements have been carried out on a number of alloys of cerium with lanthanum, varying in composition from 5% to 80% of the former, at temperatures down to 1·5°K. Lanthanum was chosen because it forms solid solutions with cerium in all proportions (Vogel and Klose 1954), and is only weakly paramagnetic (L).

---

† Communicated by the Authors.

§ 2. EXPERIMENTAL DETAILS

2.1. *Specimens*

Four alloy specimens, containing 78·9% (alloy 1), 37·6% (alloy 2), 27·0% (alloy 3), and 5·03% (alloy 4) cerium by weight, were supplied by Johnson, Matthey and Co., Ltd. They were prepared by melting together the pure metals, and a portion of each specimen was analysed afterwards. The iron content of the specimens was stated to be about 0·05%. X-ray powder photographs showed that their crystal structures were predominantly hexagonal close-packed, like that of lanthanum, whereas pure cerium is usually face-centred cubic (Spedding *et al.* 1956).

For the susceptibility measurements a small specimen of each alloy, weighing 0·4 to 1·1 g according to the concentration of cerium, was cut from the main ingot, and the remainder, weighing 35 to 45 g was used for the specific heat determinations.

2.2. *Calorimetry*

The specific heats of the alloys were measured from 1·5°K to 20°K in a liquefier-cryostat combination (Parkinson 1954), using a thin-walled copper calorimeter (PR) employing a constantan heater and a carbon thermometer. The specific heat of the empty calorimeter was determined in a separate experiment and a small correction was made for the varying mass of Wood's metal used for sealing the lid of the calorimeter.

2.3. *Magnetic Measurements*

The susceptibilities of the alloys were measured from room temperature down to 1·5°K, using a Sucksmith balance and cryostat (L). In order to correct for ferromagnetic impurities, the measurements were made in two different fields (4780 gauss and 2530 gauss) at each temperature, and the susceptibility was deduced from the slope of the straight line joining these two points on a magnetization curve, plotting magnetic moment against applied field. An estimate of the ferromagnetic saturation moment can also be obtained in this way.

§ 3. RESULTS

3.1. *Specific Heats*

The heat capacities of alloys 1, 2 and 3 are shown in figs. 1 and 2. The atomic heats of pure lanthanum (PSS) and pure cerium (PR) are included for comparison. For pure cerium the heat capacity showed a marked dependence on the previous thermal history of the sample, and the curve plotted is that obtained after the sample had been cooled to 20°K many

Fig. 1

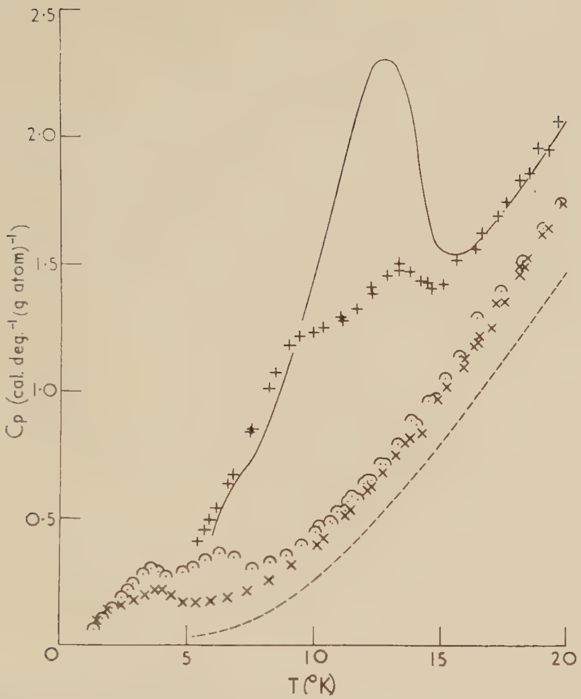

Heat capacities of cerium–lanthanum alloys. —— pure cerium ; + 78·9% Ce ; ⌒ 37·6% Ce ; x 27·0% Ce ; – – – – pure lanthanum. (One g atom is here defined as that weight of alloy which contains Avogadro's number of atoms.)

Fig. 2

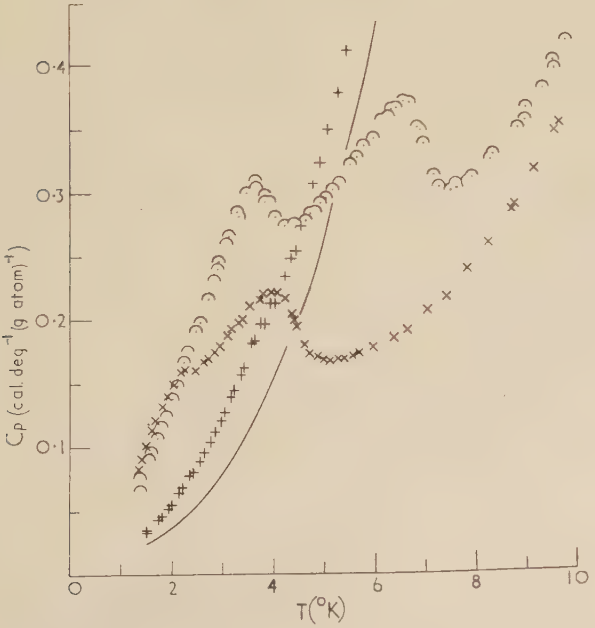

Heat capacities of cerium–lanthanum alloys. ———— pure cerium ; + 78·9% Ce ; ⌒ 37·6% Ce ; x 27·0% Ce.

times. The cerium atoms are then believed to have stabilized with one 4f electron in each. No dependence on thermal history was observed in the present measurements.

The most interesting feature of the results is that the single specific heat anomaly in pure cerium appears to split, in the alloys, into two related anomalies. These move to lower temperatures as the proportion of cerium is reduced, until in alloy 4 (5·03% Ce) (not plotted), the observed heat capacity is about the same as for pure lanthanum except below 5°K. At this temperature the curve levels off indicating that the anomalies probably still exist, but centred below 1·5°K, the lowest temperature at which measurements were made. A small irregularity at 3·5°K in the curve for alloy 1 may be related to one found at 7°K in pure cerium (PR).

Fig. 3

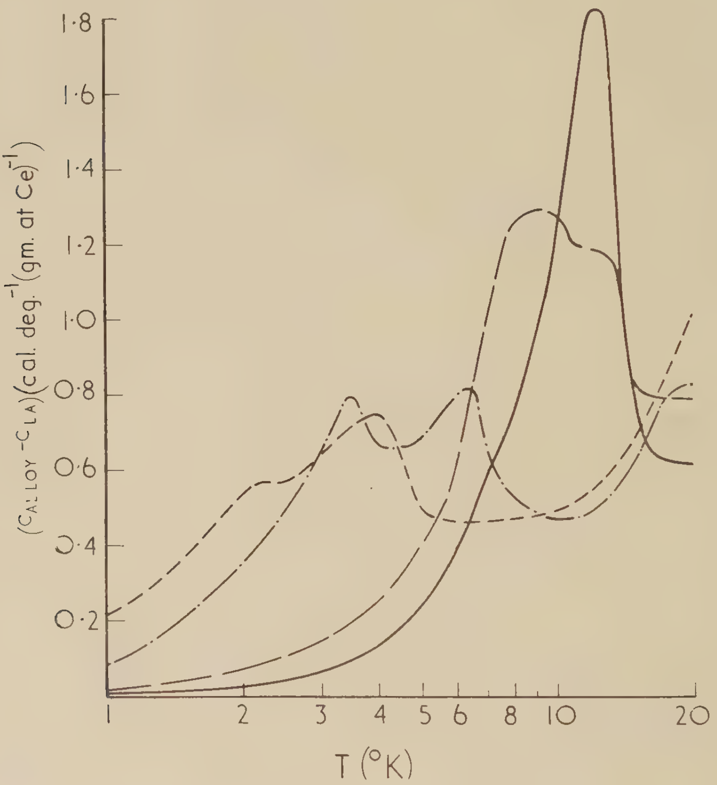

Excess heat capacities of alloys per g atom of cerium. ———— pure cerium ; — — 78·9% Ce ; —·—· 37·6% Ce ; – – – – 27·0% Ce.

In order to compare the results for the different alloys, it has been assumed that the specific heat of each can be divided into three parts : the specific heat of the lattice, the specific heat of the conduction electrons and an excess specific heat due to the unfilled 4f shell of the cerium atoms.

It is reasonable to assume that the first two of these are about the same as in lanthanum (PSS), and therefore the atomic heat of lanthanum has been subtracted from the heat capacity of one gram-atom of alloy. The difference has then been divided by the atom fraction of cerium in the alloy to give the excess heat capacity for a quantity of alloy containing one gram-atom of cerium. The results are plotted in fig. 3, together with the corresponding curve for pure cerium. The temperatures T_1 and T_2, at which the maxima in this diagram occur are given in the table.

Since the temperature scale in fig. 3 is logarithmic, the areas under the curves are a direct measure of the entropy associated with the anomalies, and these entropy values are of interest in the interpretation of the results. For pure cerium the entropy summation was arbitrarily terminated at 20°K, a temperature of approximately 1·6 times that of the peak of the anomaly. Therefore the summations for alloys 1, 2 and 3 have been terminated at about $1{\cdot}6\,T_2$, that is 20°, 10·5° and 6·5°K respectively. These temperatures also coincide with the upper minima in fig. 3. The entropies per gram of cerium, S, thus obtained are given in the table.

The rise in the excess heat capacities for alloys 2 and 3 above 10°K may imply the existence of a further anomaly at higher temperatures. A similar rise was found in pure cerium above 20°K (PSS).

3.2. *Magnetic Susceptibility*

Figures 4 and 5 show values of $1/\chi$ for the alloys plotted against temperature, where χ is the susceptibility per gramme of cerium, corrected for the paramagnetism of lanthanum (L). The correction has been made on the assumption that $\chi_0 = f\chi + (1-f)\chi_L$ where χ_L is the susceptibility per gramme of lanthanum and χ_0 the observed susceptibility per gramme of an alloy containing a fraction f by weight of cerium. For comparison the values of $1/\chi$ for pure cerium after 100 coolings (L) are also plotted.

The ferromagnetic saturation moments, M, of the alloys were roughly temperature-independent (except for alloy 3, in which a marked drop above 200°K was found) and their values are given in the table. Since the saturation moment of pure iron is about 200 e.m.u./g (Bates 1948) an iron impurity content of 0·05% can give a maximum saturation moment of 100×10^{-3} e.m.u./g. It is unfortunate that in fact the two most dilute cerium alloys gave the highest values of this moment, since the corrections to χ due to this factor then become exceedingly large, particularly in the upper part of the temperature range, amounting to 30% for alloy 4 at room temperature, and 40% for alloy 3 at 170°K. For alloys 1 and 2 this ferromagnetic correction is less than 3% at all temperatures.

Figure 4 shows that the susceptibilities of the alloys above about 80°K obey a Curie–Weiss law, $\chi = C/(T-\theta)$, where the Curie constant C increases steadily with dilution from $55{\cdot}3 \times 10^{-4}$ e.m.u./g for pure cerium

Fig. 4

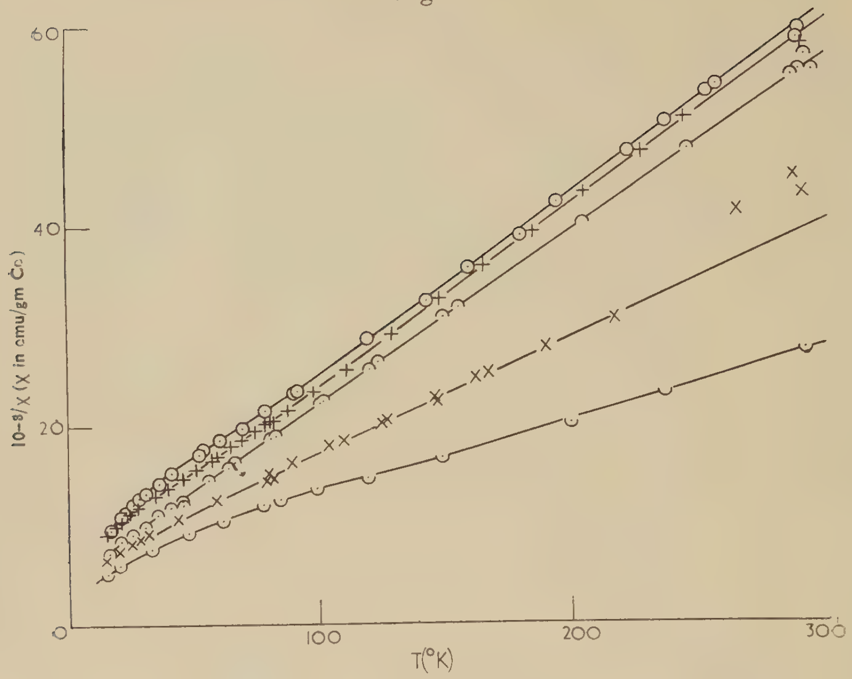

Temperature variation of $1/\chi$ for cerium–lanthanum alloys. ⊙ pure cerium; + 78·9% Ce; ◠ 37·6% Ce; × 27·0% Ce; ◡ 5·03% Ce.

Fig. 5

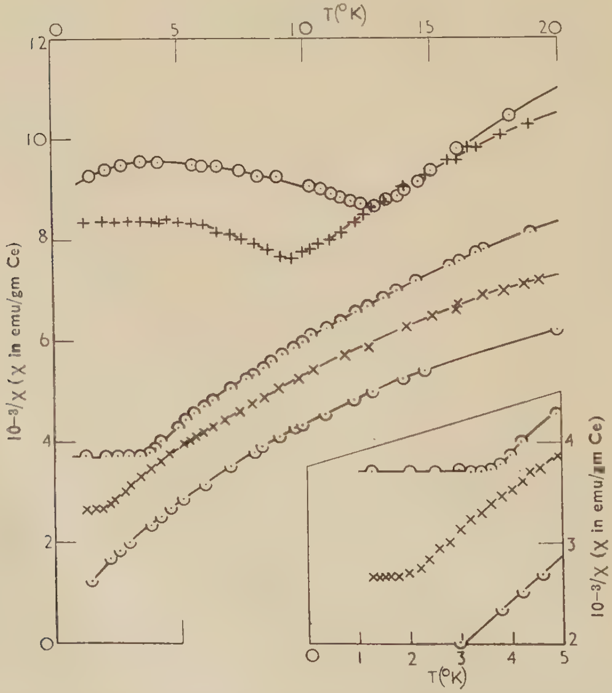

Temperature variation of $1/\chi$ for cerium–lanthanum alloys. ⊙ pure cerium; + 78·9% Ce; ◠ 37·6 Ce; × 27·0% Ce; ◡ 5·03% Ce.

to roughly 140×10^{-4} e.m.u./g Ce for alloy 4 (see the table). It is true that the values for alloys 3 and 4 are probably rather inaccurate owing to uncertainty in the ferromagnetic correction, but it is improbable that this could account for the entire variation of C observed. It is interesting that the temperature hysteresis found in the susceptibility of virgin specimens of pure cerium (L) is entirely absent in the alloys.

Figure 5 shows the behaviour of the low temperature magnetic anomaly as the cerium concentration is altered. The maximum in the susceptibility of pure cerium at 12·5°K moves to a lower temperature for alloy 1. In alloys 2 and 3 no maximum is found, but a rather sharp change to temperature-independent paramagnetism occurs. Alloy 4 shows no anomaly down to 1·5°K, the lowest temperature at which measurements were made. The temperature at which the behaviour of the susceptibility changes, T_3, is given in the table, together with values of the effective atomic moments in Bohr magnetons (μ_B) calculated from the Curie constants per gramme of cerium at the higher temperatures.

Alloy	T_1	T_2	T_3	$M\times10^3$ (e.m.u./g)	$C\times10^4$ (e.m.u./g Ce)	(μ_B) eff	S (cal/°K/g at Ce)
Pure Ce	12·3	—	12·5	—	55·3	2·50	1·3
1	9·3	~12·5	9·5	<1	56·1	2·51	1·45
2	3·5	6·4	3·6	~2	59·2	2·59	1·2
3	~2·2	4·0	1·9	~35 (below 200°K)	85	3·1	1·1
4	—	—	—	8	140	4·0	—

§ 4. DISCUSSION

A theory of anti-ferromagnetism in anisotropic crystals has been given by Néel (1936) and Van Vleck (1941). It shows that there is a general tendency for the atomic moments to line up in an antiparallel array perpendicular to the direction of the applied field, and when this happens an almost temperature-independent susceptibility should occur. This tendency is opposed by the anisotropic crystal field which tends to align the atomic moments in a preferred direction in the crystal. When the magnetic field is applied parallel to such a direction, the susceptibility should fall as the temperature is lowered, tending to zero at 0°K. The combination of these two effects in polycrystalline materials gives rise to the maximum normally associated with anti-ferromagnetism. Experimental evidence from susceptibility measurements on single crystals is in general agreement with this theory (van den Handel *et al.* 1952).

This suggests a possible explanation for the appearance of temperature independent paramagnetism in the more dilute alloys of cerium with lanthanum. In pure cerium and in the concentrated alloy 1, the crystalline anisotropy is great enough to cause the usual maximum in the susceptibility when anti-ferromagnetism sets in at the temperature T_3. In the more dilute alloys however, although anti-ferromagnetic ordering still occurs, its direction is free to orient itself perpendicular to the applied field, and this gives rise to temperature-independent paramagnetism.

If the change in behaviour of the susceptibility at the temperature T_3 is indeed indicative of the onset of some kind of magnetic ordering we should expect an anomaly in the specific heat at this temperature, and we see from the table that the temperature T_1 of the lower maximum in the specific heat does in fact coincide very closely with T_3. The upper maximum in the specific heat, however, remains unexplained. There is no observable anomaly in the susceptibility coinciding with it, and yet it seems probable that it is closely related to the lower maximum, since T_1 and T_2 both decrease steadily with dilution. In addition both specific heat maxima must be taken into account in order to obtain an entropy contribution per atom of cerium comparable with that for pure cerium. It therefore appears that, whatever form the ordering of the 4f electrons takes, it is in some way divided into two stages in the alloys, whereas in pure cerium the stages coincide. Possibly the difference is associated with the fact that the crystal structure of the alloys (hexagonal close-packed) has a lower symmetry than that of pure cerium (face-centred cubic).

The increase in the effective moment of the cerium atoms in the more dilute alloys suggests that there is a tendency for transitions from the outer valency bands of electrons (5d and 6s) into the 4f shell to take place, thus increasing the population of the latter. The maximum moment found is $4{\cdot}0\mu_B$ per atom, slightly greater than the theoretical value for neodymium ($3{\cdot}62\mu_B$), whose moment should be the greatest among the first half of the rare-earth group (Van Vleck 1932). This high value may be partly due to an over-estimate of the Curie constant of alloy 1 owing to errors in the ferromagnetic correction and in the estimate of the paramagnetism of the conduction electrons. The measurements suggest however that in dilute alloys of cerium with lanthanum the population of the 4f shell is increased from 1 to 2 or 3 electrons per atom.

Such a transfer of electrons would not necessarily increase the entropy in the low temperature anomaly. In pure cerium the degeneracy of the ground state of the atom ($^2F_{5/2}$) should give rise to a total excess entropy of $R \ln (2J+1) = 3{\cdot}58$ cal deg^{-1} (g atom)$^{-1}$, whereas only a part, $1{\cdot}27$ cal deg^{-1} (g atom)$^{-1}$ (cf. $R \ln 2 = 1{\cdot}38$) appears to be associated with the anti-ferromagnetic ordering at 12·5°K. The remainder is found between 20°K and room temperature (Skochdopole *et al.* 1955). A similar entropy distribution may therefore be expected in the alloys, and as we have seen, alloys 2 and 3 do in fact show an appreciable rise in excess specific heat above 10°K.

The conclusions reached in this section are of a tentative nature, and clearly are not a completely satisfactory explanation of all the features observed.

ACKNOWLEDGMENTS

The authors are indebted to Dr. D. H. Parkinson for suggesting this problem and for his continued interest and advice. They wish to thank Mr. D. C. Handley, Mr. A. G. Harris and Mr. J. F. C. Oliver for their help with the experiments. This paper is published by permission of the Controller, H.M. Stationery Office.

REFERENCES

BATES, L. F., 1948, *Modern Magnetism*, 2nd Edn. (Cambridge : University Press), p. 245.
VAN DEN HANDEL, J., GIJSMAN, H. M., and POULIS, N. J., 1952, *Physica*, **18,** 862.
LOCK, J. M., 1957, *Proc. phys. Soc. Lond.* B, **70,** 566.
NÉEL, L., 1936, *Ann. Phys, Paris*, **5,** 232.
PARKINSON, D. H., 1954, *J. sci. Instrum.*, **31,** 178.
PARKINSON, D. H., and ROBERTS, L. M., 1957, *Proc. phys. Soc. Lond.* B, **70,** 471.
PARKINSON, D. H., SIMON, F. E., and SPEDDING, F. H., 1951, *Proc. roy. Soc.* A, **207,** 137.
SKOCHDOPOLE, R. E., GRIFFEL, M., and SPEDDING, F. H., 1955, *J. chem. Phys.*, **23,** 2258.
SPEDDING, F. H., DAANE, A. H., and HERRMAN, K. W., 1956, *Acta Cryst.*, **9,** 559.
VAN VLECK, J. H., 1932, *The Theory of Electric and Magnetic Susceptibilities* (Oxford : University Press), p. 243 ; 1941, *J. chem Phys.*, **9,** 85.
VOGEL, R., and KLOSE, H., 1954, *Z. Metallk.*, **45,** 633.

A Propane Bubble Chamber†

By Margaret H. Alston, B. Collinge, W. H. Evans, R. W. Newport
and P. R. Williams
Nuclear Physics Research Laboratory, University of Liverpool

[Received March 25, 1957]

Abstract

A propane bubble chamber of effective volume 1 litre has been constructed for experiments on the elastic scattering of low energy ($<$ 40 MeV) π^+-mesons on hydrogen and carbon. Stereoscopic pairs of pictures are taken on 35 mm film with a stero angle of 90°. The design and operation of the chamber and associated equipment is described. and examples of pictures taken are shown.

§ 1. Introduction

The mechanism governing the operation of bubble chambers is not fully understood but a theory proposed by Glaser (Glaser 1953, 1954) enables the approximate operating conditions to be determined for a variety of liquids. Since the pioneer work of Glaser in 1952 (Glaser 1952) several authors (Glaser 1953, Glaser and Rahm 1955, Leitner *et al.* 1955, Parmentier and Schwemin 1955, Bassi *et al.* 1956, Glaser and Brown 1956, Glaser *et al.* 1956, Nagle *et al.* 1956 Pless and Plano 1956) have published details of bubble chambers of the two main types in current use, namely ‘ clean ’ chambers, constructed entirely of glass and ‘ dirty ’ chambers fabricated of metals, gaskets and glass.

The present paper gives details of the construction and operation of a ‘ dirty ’ propane bubble chamber which has been designed to investigate the interactions of low energy pions ($<$40 MeV) with hydrogen and carbon using the external pion beams of the Liverpool synchrocyclotron. At these energies the range of the recoil protons in propane is short. To minimize the risk of missing short recoil tracks during the analysis of the pictures two plane projections of the sensitive volume of the chamber at 90° to each other are photographed using dark field illumination. This procedure also makes the computation of the true geometry of the interactions relatively simple and eliminates corrections for the high index of refraction of the glass windows and the chamber liquid.

§ 2. Description of the Chamber

The body of the chamber (fig. 1 (*a*)) is a rectangular block of MG5 aluminium alloy, 6 in. × 6 in. × 12 in. with a 3 in. diameter cylinder removed along the axis of greatest length. Two rectangular windows of

---

† Communicated by Professor H. W. B. Skinner, F.R.S.

$\frac{1}{2}$ in. armour-plate glass are fastened to adjacent faces of the chamber body by flanges of MG5 using Bridgman type seals with 'Gaco' oil-seal rubber gaskets (fig. 1 (*b*)). Each window is 6 in. × 3 in. and a useful volume of approximately 1 litre is photographed. In this region the inner diameter of the chamber is increased to $3\frac{3}{8}$ in. to prevent the direct illumination of the walls. The illumination window is 3 in. in diameter and is attached in the same way as the other windows. Opposite this is a thin metal window of $2\frac{1}{2}$ in. diameter and 0·194 in. thick through which the beam of particles enters the chamber. The whole of the inside surface of the chamber is highly polished to reduce wall boiling and anodised black to provide a good photographic background. When fully assembled the chamber was tested with a static pressure of 800 p.s.i. which is twice the operating pressure.

The chamber is pressurized by means of a free-moving aluminium piston (Leitner *et al.* 1955) running in a brass cylinder with a polished chromium-plated liner. Sealing is effected by means of two 'Gaco' piston seals, the space between them being connected to the atmosphere. The position of the piston is measured by pushing a rod into contact with its outer end, and this enables the change in volume during an expansion to be measured. The expansion cylinder communicates with the bubble chamber through a low impedance 'neck' $4\frac{1}{4}$ in. long and 2 in. in diameter.

The expansion cylinder, safety valve, condenser-type pressure gauge, and filling line are attached to the chamber in the unphotographed region to reduce the amount of background boiling appearing on the photographs.

The filling system allows propane gas to pass through a filter and condense in the chamber. There are facilities for evacuating the chamber, adjusting the amount of propane therein and for measuring the static pressure.

The whole of the chamber and expansion cylinder are immersed in a water bath, of capacity ~100 litres, the temperature of which is thermostatically controlled to within ±0·2°c in the range 56°c to 62°c.

§ 3. The Expansion System

To operate a bubble chamber of the 'dirty' variety the expansion system must be capable of performing, in a reproduceable manner, a rapid expansion and a rapid recompression a few milliseconds later. A rapid expansion is necessary since the minimum pressure obtained during an expansion is the net result of a lowering of the pressure, due to movement of the piston, and a return to the saturated vapour pressure due to boiling on the walls and gaskets. If the bubbles formed are permitted to coalesce at the top of the chamber it may be necessary to delay recycling for several minutes while these bubbles collapse, but, if the recompression is sufficiently rapid most of the bubbles can be made to collapse before they reach the top of the chamber (Leitner *et al.* 1955). Rapid collapse of the bubbles is assisted by pressurizing the chamber above the saturated vapour pressure at the operating temperature.

Fig. 1 (*a*)

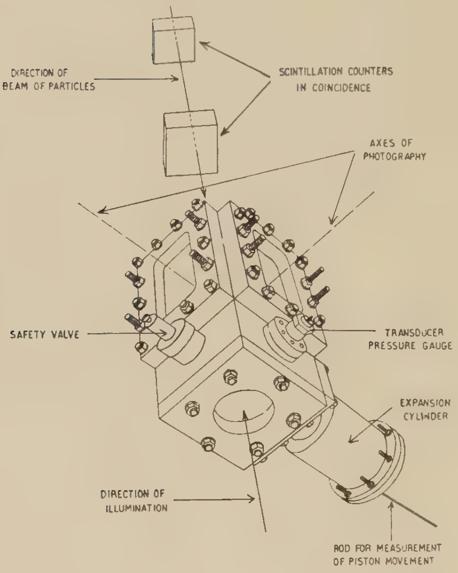

Schematic drawing of the bubble chamber.

Fig. 1 (*b*)

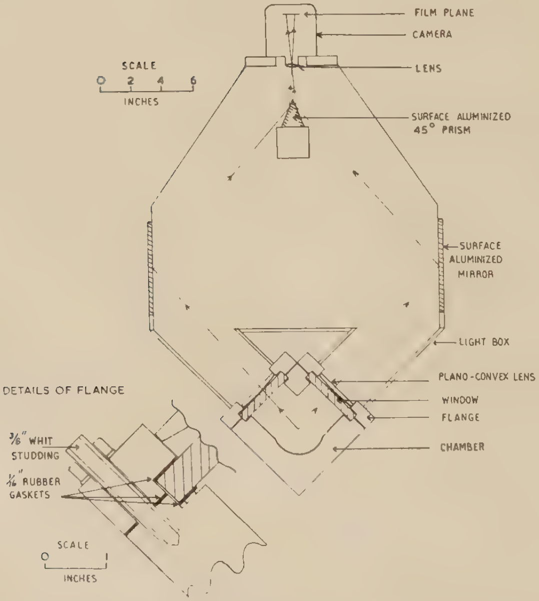

Schematic drawing of the bubble chamber and camera mounting.

A commercial valve with the required speed and reliability could not be found in this country when the work was started. The expansion system used (fig. 2) consists essentially of two valves. The first C is a high-pressure high-speed three way valve of novel design which is connected to the expansion cylinder. This valve is in turn controlled by a low-pressure three-way pilot valve. The piston of the high-pressure valve C is held sealed on a ½ in. diameter hole, against the 375 p.s.i. in the expansion cylinder, by applying 65 p.s.i. to its larger diameter end. When the lower pressure is released and falls below that required for sealing, the high pressure acts on the full area of the 1 in. diameter end of the piston of valve C. After the first ½ in. of its stroke this piston imposes a high impedance in the high pressure gas inlet. During the second ½ in. of its stroke, when it is moving fastest, it opens two ½ in. diameter holes to the atmosphere releasing the gas acting on the piston of the expansion cylinder and thus expanding the chamber. The replacement of the low pressure gas in valve C returns the piston of C to its original position and thus re-applies the high pressure gas to the expansion cylinder. Sealing takes place in this valve before the pressure in the expansion cylinder has fully built up.

Fig. 2

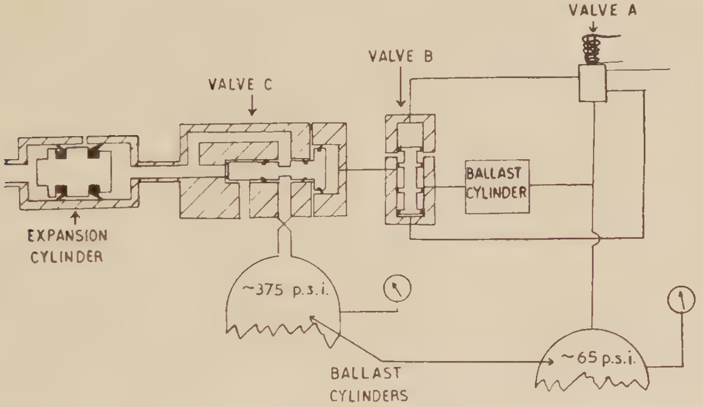

Expansion system.

The low pressure gas in valve C is controlled by valves A and B. A is a commercial solenoid operated valve. On energizing or de-energizing this solenoid the gas pressure from one end of valve B is removed and pressure is applied to the other end. This causes the piston of valve B to move from one end to the other. During its movement this piston releases the gas from the low pressure end of valve C and replaces it after a short delay. Valve B although constructionally asymmetric is symmetric in operation. By varying the low pressure applied to valves A and B the time for valve B to complete its stroke is altered, thus changing the delay between expansion and recompression of the chamber.

In this way the chamber is made to undergo a complete expansion and recompression cycle by either energizing or de-energizing the solenoid of valve A. Due to the high impedance of valves A and B about 80 msec elapses from the start of operation of valve A to the beginning of the expansion stroke in the chamber. Most of this delay is due to the high impedance in A but the delay is constant to less than $\frac{1}{2}$ msec. Two gas pressures are required, one ($\sim$65 p.s.i.) for valves A and B and the other (375 p.s.i.) for valve C; both of these are supplied by one compressor which feeds two automatically adjusting reducing valves. To avoid variations in pressure due to gas flow through long supply lines, ballast cylinders are placed close to the expansion valve system, the connections to the latter being made by short pipes of wide bore.

§ 4. Pressure Measurement

A capacitance transducer gauge with a frequency response of 25 kc/s and a linear capacitance change of 20 pF over the range of pressures 0 to 720 p.s.i. is fitted into the wall of the chamber (fig. 1 (*a*)). The variations in capacitance of this gauge due to changes in the pressure in the chamber are used to modulate the frequency of a Franklin oscillator (fig. 3). The resulting frequency changes are transformed into voltage changes by means of a ratio detector (Sturley 1955) and after amplification these voltage variations are fed on to the Y plates of a specially designed oscilloscope. To ensure that the full pressure cycle takes place with the ratio detector working in its linear region the frequency of the oscillator is set at 10·7 Mc/s when the chamber pressure is 230 p.s.i.

Fig. 3

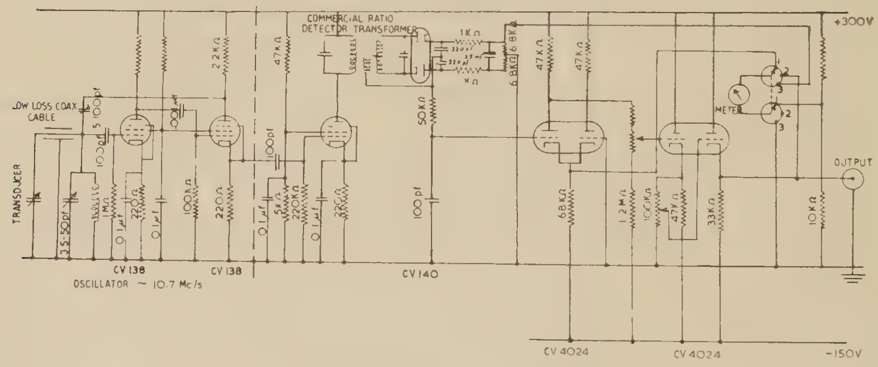

Electronic pressure gauge.

The oscilloscope used has a triggered time base of 200 msec length and the tube has a persistence of 10 seconds. The brightness can be modulated by a multivibrator of period 0·75 msec thus providing a time calibration on the trace. It also has facilities for mixing sharply defined timing pulses with the output from the pressure measuring circuit.

The trace is triggered at the same time as the expansion valve begins to operate and after a fixed interval (~ 80 msec) the variation of the chamber pressure with time is displayed. Figure 4 (Plate) shows a photograph of the trace obtained. The full cycle of expansion and recompression takes place in <30 msec, the lowest pressure of about 180 p.s.i. is attained in 3 msec and the chamber is sensitive for less than 2 msec. It is seen from the photograph that much of the re-pressurization is due to boiling in the chamber and occurs before the high pressure gas is re-admitted into the expansion cylinder.

The output voltage from the pressure measuring circuit is also used to measure the static pressure in the chamber by applying it to a voltmeter calibrated in p.s.i. This measurement is important since the chamber is isolated from the pressure gauge in the filling system during operation.

Great care is taken to ensure that the dynamic pressure changes in the chamber are accurately represented by the oscilloscope trace. A knowledge of the minimum pressure attained during an expansion at a given temperature is extremely useful since the minimum pressure required for sensitivity at a given temperature can be calculated approximately from Glaser's formulae (Glaser 1953). It is found that the minimum pressure obtained with the given expansion system, rises more slowly with temperature than that given by Glaser's formula. By comparing the variation in the minimum pressure obtained as the temperature is raised with that required, it is possible to predict approximately the minimum operating temperature for a given instrument.

An accurate knowledge of the dynamic pressure in the chamber also enables the effect of varying the speed of expansion to be assessed quantitively, and is of great value during the initial testing of the bubble chamber.

§ 5. THE TIMING SEQUENCE

During normal operation the 156 in. synchrocyclotron provides a beam of accelerated particles in short bursts (100 to 400 μsec long) repeated at 10 msec intervals. For use with the bubble chamber the machine can be operated to give a single burst of particles. The sensitive time of the bubble chamber is not more than 2 msec and to ensure that the beam of particles traverses the chamber during this interval the operation of the chamber is synchronized with the modulation frequency of the synchrocyclotron radio frequency system.

An optical system attached to the shaft of the rotating condenser of the synchro-cyclotron generates a positive pulse for each modulation cycle of the radio-frequency. One of these synchronizing pulses (fig. 5) is arbitrarily selected by the bubble chamber control unit and successive pulses are counted using a cold cathode decatron tube (CV 2223). After a number of pulses n, not greater than 10, have been counted, the $(n+1)$th pulse is used to initiate a sequence of operations which causes the synchrocyclotron to accelerate a single pulse of particles after a delay of 13 msec.

The total time T between the selection of the first synchronizing pulse and the entry of the particles into the chamber is thus $10(n+1)+13$ msec. The time taken for the chamber to attain a sensitive condition after the actuation of the expansion system is $(T-t)$ msec and by a suitable choice of n, t can be made not more than 10 msec. The expansion system is therefore pulsed t msec after the first synchronizing pulse is selected, t being continuously variable from 0 to 10 msec.

The entry of the beam of particles into the chamber is registered by two scintillation counters in coincidence. The coincidence pulse is used as a time marker which can be mixed with the output of the electronic pressure gauge and appears as a sharp pulse superimposed in the pressure time curve. To obtain the correct timing sequence for operation of the chamber the oscilloscope is observed and the two variables n and t adjusted so that the time marker pulse appears on the correct region of the pressure time curve. The coincidence pulse also triggers the light source after a delay which is variable from 0 to 3 msec.

Fig. 5

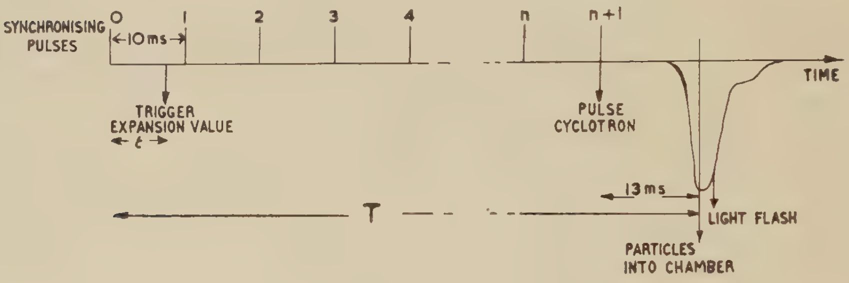

Timing sequence.

The complete sequence of operations described above is regularly repeated at predetermined intervals variable from 2 to 40 sec.

§ 6. Illumination and Photography

The camera and illumination are arranged to give a 90° stereoscopic angle and dark field illumination with the direction of the light at 90° to the directions of photography (fig. 1 (*b*)). A high intensity light source is required since only a small fraction of the incident light is scattered into the camera lens. The source must also be of small dimensions, since the light traversing the chamber must be well collimated to minimize the direct illumination of the walls.

A light pulse of 20 μsec duration is produced by discharging a condenser of capacity 33 μF charged to 4000 volts, through a spark gap in air. This spark gap is a type described by Bardócz and Klatsmányi (1955) and can be easily triggered. A condensing lens placed in front of the spark gap produces a beam of light which is slightly convergent. To increase the intensity of the light a concave mirror is placed behind the spark gap and the inner surface of the beam entry window is chromium plated and highly polished.

A camera and mirror system are mounted as shown in fig. 1 (*b*). The two plano-convex lenses are placed so that the camera lens is in their focal plane (Campbell and Pless 1956). With this system two plane projections at right angles are obtained side by side on the film. Photographs are taken with a camera lens of 3 in. focal length working at *f*/8 on Kodak R60, 35 mm recording film giving a demagnification of 8·5.

For analysis each pair of pictures is projected on to a translucent screen to give images double the real size. Measurements are made on each projection separately by viewing against the direction of the light and the true measurements are computed.

§ 7. CHARACTERISTICS OF THE CHAMBER

In the operation of a bubble chamber there are five principal parameters, namely: (1) the temperature, (2) the minimum pressure reached during an expansion, (3) the volume change during an expansion, (4) the static pressure applied to the propane, (5) the delay between the entry of the particles into the chamber and the taking of the photograph. The effect of varying these parameters on the operating characteristics has been found and will now be discussed.

Below 56°c the chamber is not sensitive because the minimum pressure reached is not far enough below the vapour pressure to produce a sufficient degree of superheat. As the temperature is raised to 56°c the chamber becomes sensitive to the electron track endings produced when a ^{60}Co source is placed near. The volume change needed for this condition to be attained is 3% of the chamber volume, and this is called the expansion ratio. As the temperature is raised to 59°c, the chamber records 95 MeV π-mesons ($\beta=0{\cdot}8$) with an expansion ratio of 2% and a minimum pressure of 170 p.s.i. At 61°c the chamber is sensitive to minimum ionizing particles; the minimum pressure under these conditions is 180 p.s.i. An increase in the expansion ratio from 2% to 4% does not alter the minimum pressure reached but increases the sensitive time. As the timing sequence is reproduceable to $\frac{1}{2}$ msec an expansion ratio of 2% is sufficient.

The effect of increasing the static pressure applied to the propane is to increase the possible recycling rate by recompressing more rapidly the bubbles formed during an expansion. At 61°c the vapour pressure of propane is 320 p.s.i. and with a static pressure of 370 p.s.i. the chamber can be recycled every 5 seconds.

The time taken for the bubbles to grow to a convenient size for photography is 2 msec, but photographs have been obtained with flash delays of 300 μsecs. With a delay of 2 msec no distortion of the tracks of 95 MeV π-mesons is observable, other than that due to multiple coulomb scattering.

These results were obtained with a filling of commercial quality propane, the impurities being ethane, 2% and sulphur, 0·003%.

Apart from the parameters discussed the characteristics of the chamber depend on the smoothness of the internal surfaces. When initial attempts were made to operate the chamber, the sensitive volume was seen to contain large ‘plumes’ of bubbles in addition to tracks (fig. 6, Plate). This effect is thought to be due to roughness of the chamber walls as a result of the machining because the effect is no longer observed since the inner surfaces have been highly polished and re-anodized (fig. 7, Plate).

§ 8. DISCUSSION

A bubble chamber has several advantages over a diffusion cloud chamber or a Wilson cloud chamber for the proposed experiment on low energy pion scattering. The medium has a high density (0·43 g/cm^3) and a larger number of interactions will be obtained per picture than in a cloud chamber. The rate at which pictures can be taken is also greater.

The bubble chamber does however have several disadvantages. The medium contains both hydrogen and carbon (C_3H_8) and the interactions occurring in H and C have to be identified accurately from the kinematics. The high stopping power of the medium makes the recoil tracks very short and therefore difficult to detect and measure. This latter difficulty is partially overcome by using 90° stereo-photography and cumbersome corrections for the high refractive index of the glass and propane are avoided by using plane projections.

A hydrogen bubble chamber is an ideal instrument for this experiment but is considerably more difficult to construct and operate.

No magnetic field is applied to the propane chamber since the multiple coulomb scattering is large at these low energies and a very large field is required (∼30 k gauss).

Recycling rates considerably faster than one every 5 sec are mechanically possible. The recycling rate used at present is determined by the amount of high pressure gas available.

The instrument has been used for several days in conjunction with the 156 in. synchrocyclotron. The initial setting up is accomplished by observing the trace on the oscilloscope and varying the delay between the start of the expansion valve cycle and the entry of the particles into the chamber until the coincidence pulse appears on the correct portion of the pressure time curve (fig. 4, Plate). Tracks can also be observed in the chamber visually.

The optical resolution achieved with the system used is not high enough for accurate bubble counts to be made. This is not however a serious disadvantage for the proposed experiment since at low pion energies the tracks are essentially solid unless extremely high resolution is used or the chamber is operated at low sensitivity (Glaser *et al.* 1956, Blinov *et al.* 1956). The energy spectrum of the incident π-mesons can be obtained by measuring the track lengths in the chamber and the energy of scattering events determined from the kinematics. Bubble counting is very tedious and time consuming and would not in any case, be used when several thousands of tracks have to be measured. It is likely to be of use in the future to assist in the identification of particles from their tracks in bubble chambers (Budde *et al.* 1956).

ACKNOWLEDGMENTS

The authors would like to thank Professors H. W. B. Skinner and J. M. Cassels for their encouragement and interest ; and also Messrs. A. Cave and R. Thompson who built much of the apparatus. R. W. Newport wishes to thank D.S.I.R. for a maintenance grant.

REFERENCES

BARDÓCS, A., and KLATSMÁNI, Á., 1955, *Rev. sci. Instrum.*, **26**, 945.
BASSI, P., LORIA, A., MEYER, J. A., MITTNER, P., and SCOTONI, J., 1956, *Nuovo Cim.* 491.
BLINOV, G. A., KRESTNIKOV, I. S., and LOMANOV, M. F., 1956, *CERN Symposium*, **2**, 25.
BUDDE, R., CHRETIEN, M., LEITNER, J., SAMIOS, N. P., SCHWARTZ, M., and STEINBERGER, J., 1956, *Phys. Rev.*, **103**, 1827.
CAMPBELL, N. P., and PLESS, I. A., 1956, *Rev. sci. Instrum.*, **27**, 875.
GLASER, D. A., 1952, *Phys. Rev.*, **87**, 665 ; 1953, *Ibid.*, **91**, 762 ; 1954, *Nuovo Cim.*, **11**, Suppl. 2, 361.
GLASER, D. A., and BROWN, J. L., 1956, *Phys. Rev.*, **102**, 586.
GLASER, D. A., and RAHM, D. C., 1955, *Phys. Rev.*, **97**, 474.
GLASER, D. A., RAHM, D. C., and DODD, C., 1956, *Phys. Rev.*, **102**, 1653.
LEITNER, J., SAMIOS, M., SCHWARTZ, M., and STEINBERGER, J., 1955, *Nevis Report*, 10. R 105. CU84 (unpublished).
NAGLE, D. E., HILDEBRAND, R. H., and PLANO, R. J., 1956, *Rev. sci. Instrum.*, **27**, 203.
PARMENTIER, D., and SCHWEMIN, A. J., 1955, *Rev. sci. Instrum.*, **26**, 954.
PLESS, A., and PLANO, R. J., 1956, *Rev. sci. Instrum.*, **27**, 935.
STURLEY, K. R., 1955, *Wireless World*, **61**, 532.

REVIEWS OF BOOKS

Thermodynamics and Statistical Mechanics. By A. H. Wilson. (Cambridge University Press, 1957.) Price 50*s.*

This is an advanced textbook written, as the author says, for theoretical physicists. It will be invaluable for them and for the growing number of solid-state physicists, physical chemists and others who need a thorough understanding of both thermodynamics and statistical mechanics and of their relationship to atomic mechanisms in order to understand the problems that they investigate. The author develops these subjects and has applied them to selected fields, such as electrolytes and electrochemical systems, chemical reactions and superlattices in alloys. As a clear and reliable introduction, the book can be thoroughly recommended. N. F. M.

Radiation Handbook. (National Bureau of Standards Handbook 62. U.S. Government Printing Office, Washington, D.C.) Price 40 cents.

This small volume published by the International Commission of Radiological Units and Measurements contains much information basic to the practice of dosimetry as well as the most recent international recommendations. It can confidently be commended to the attention of readers of the *Philosophical Magazine.* L H. G.

[*The Editors do not hold themselves responsible for the views expressed by their correspondents*]

Fig. 1

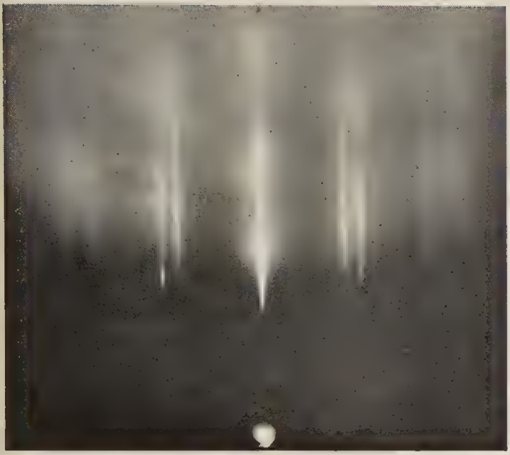

Silver substrate plus 2 Å of lead: silver $[1\bar{1}0]$ azimuth.

Fig. 2

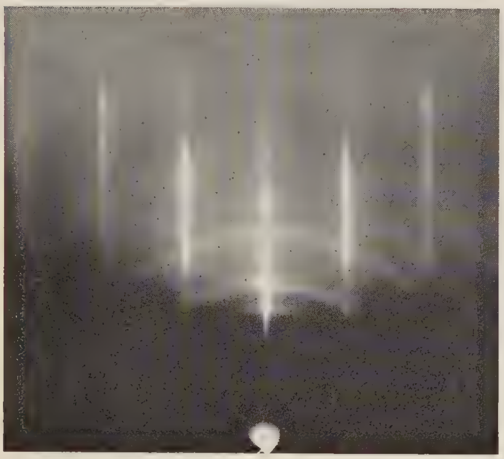

6 Å of lead on silver: (111) plane, $[1\bar{1}0]$ azimuth.

Fig. 3

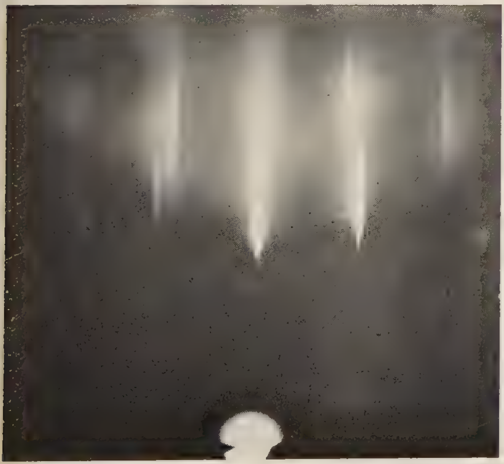

Silver substrate plus 1·5 Å of thallium: silver $[1\bar{1}0]$ azimuth.

Fig. 4

8 Å of tin on silver: silver $[1\bar{1}0]$ azimuth.

Fig. 5

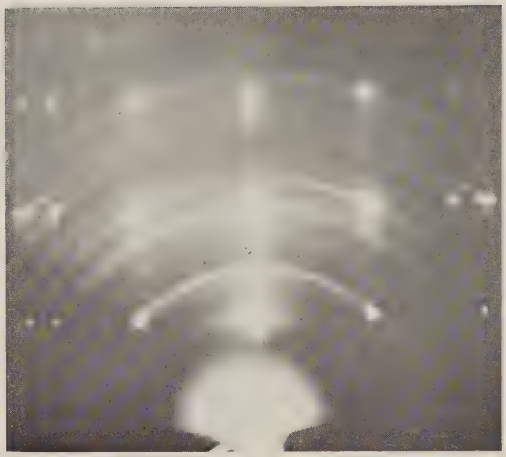

60 Å of tin on silver: silver $[2\bar{1}\bar{1}]$ azimuth.

Fig. 7

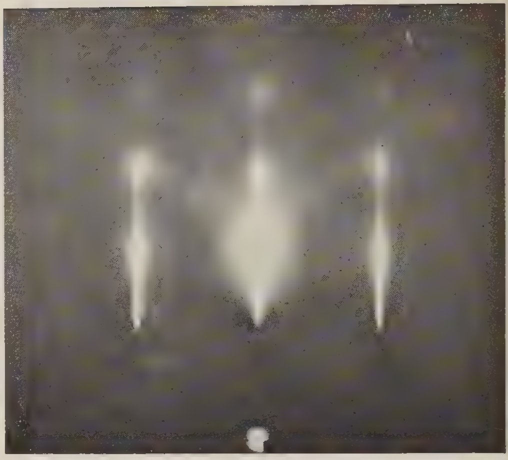

40 Å of silver on silver: (111) plane, $[2\bar{1}\bar{1}]$ azimuth.

Fig. 8

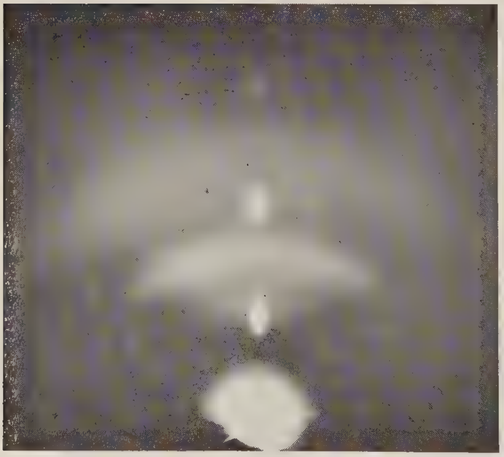

10 Å of antimony on silver: silver $[1\bar{1}0]$ azimuth.

Fig. 9

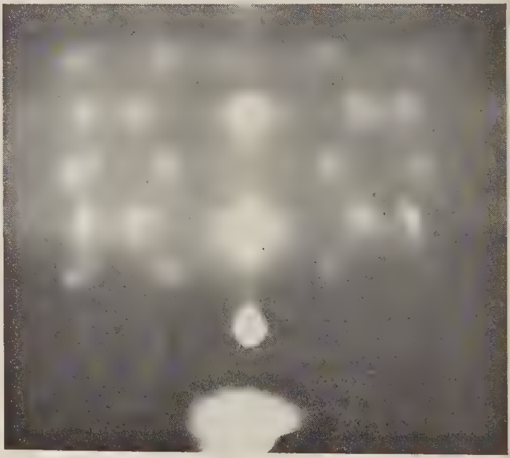

80 Å of antimony on silver: pattern independent of azimuth setting.

Fig. 1

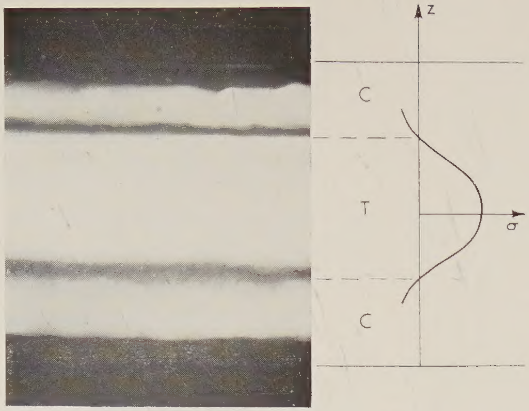

(*a*) ×13 (*b*)

Bar of silver chloride plastically deformed in tension; load released. (*a*) photoelastic pattern, (*b*) distribution of longitudinal stress σ.

Fig. 3

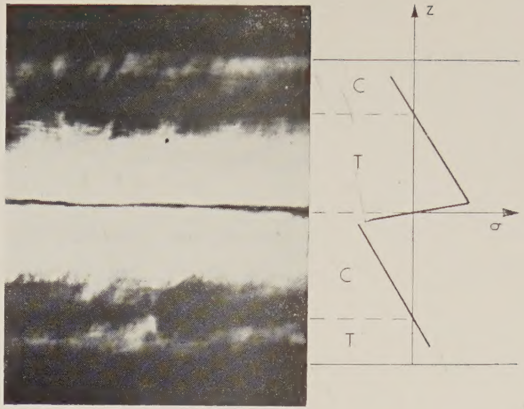

(*a*) ×11 (*b*)

Bar plastically bent; external couples removed. (*a*) photoelastic pattern, (*b*) stress distribution.

Photographs taken with crossed nicols, at 45° to the extinction directions. T=tension, C=compression.

Fig. 2

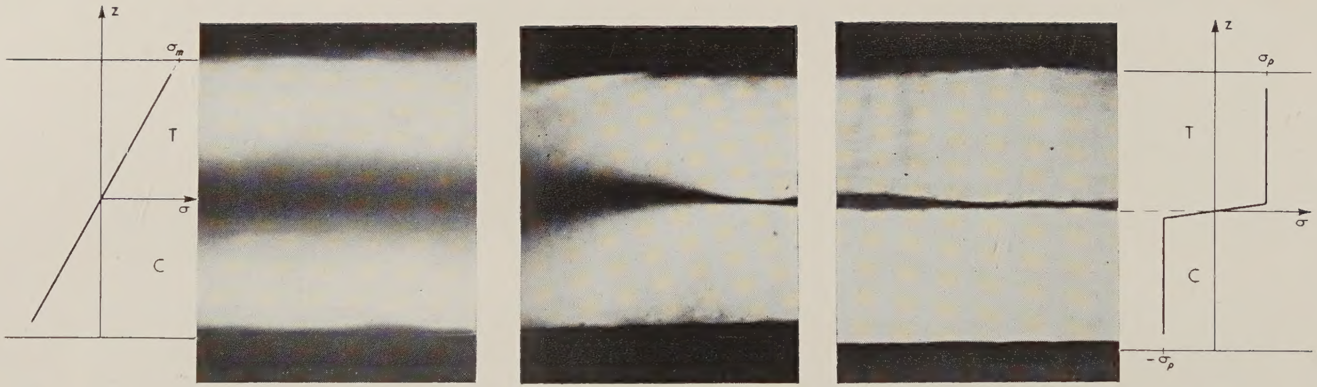

(*a*) (*b*) ×11 (*c*) ×10 (*d*) ×10 (*e*)

Bent bar with external couples still applied, showing longitudinal propagation of plastic deformation. (*a*) stress in elastic region, (*b*) elastic region, (*c*) elastic–plastic transition, (*d*) plastic region, (*e*) stress in plastic region.

Photographs taken with crossed nicols, at 45° to the extinction directions. T=tension, C=compression.

Fig. 4

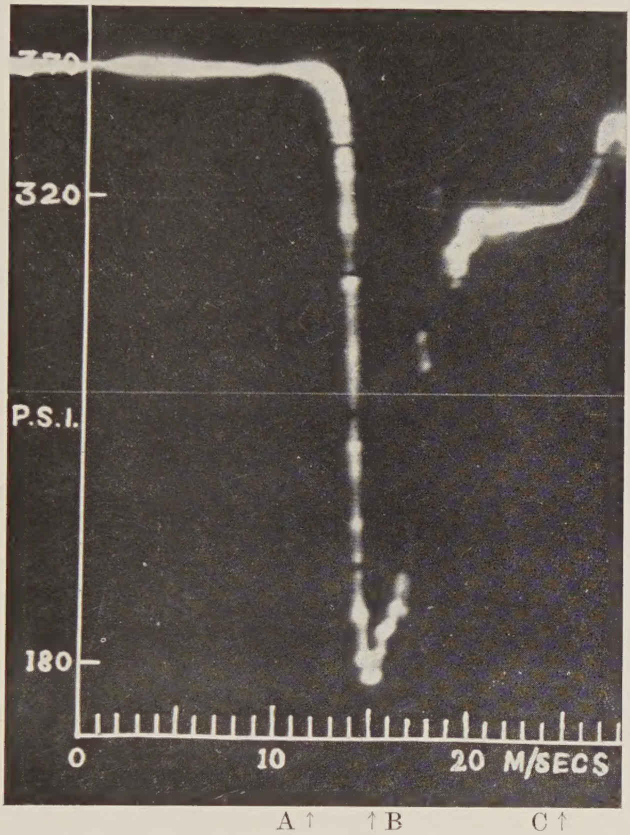

A photograph of the pressure time curve displayed on the oscilloscope.

A. The chamber starts expanding.
B. Particles enter the chamber.
C. High pressure is re-applied to the chamber.

Fig. 6

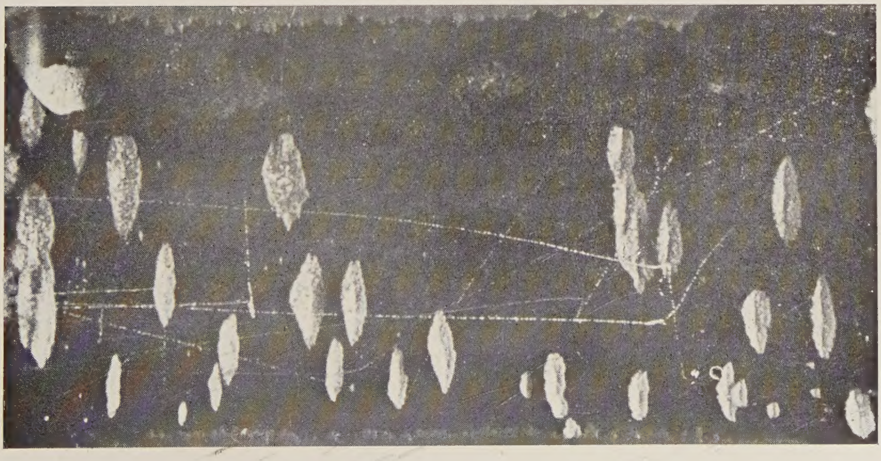

A single photograph of low energy π^+-meson tracks in the bubble chamber, showing the ' plumes ' produced by boiling on the walls.

Fig. 7

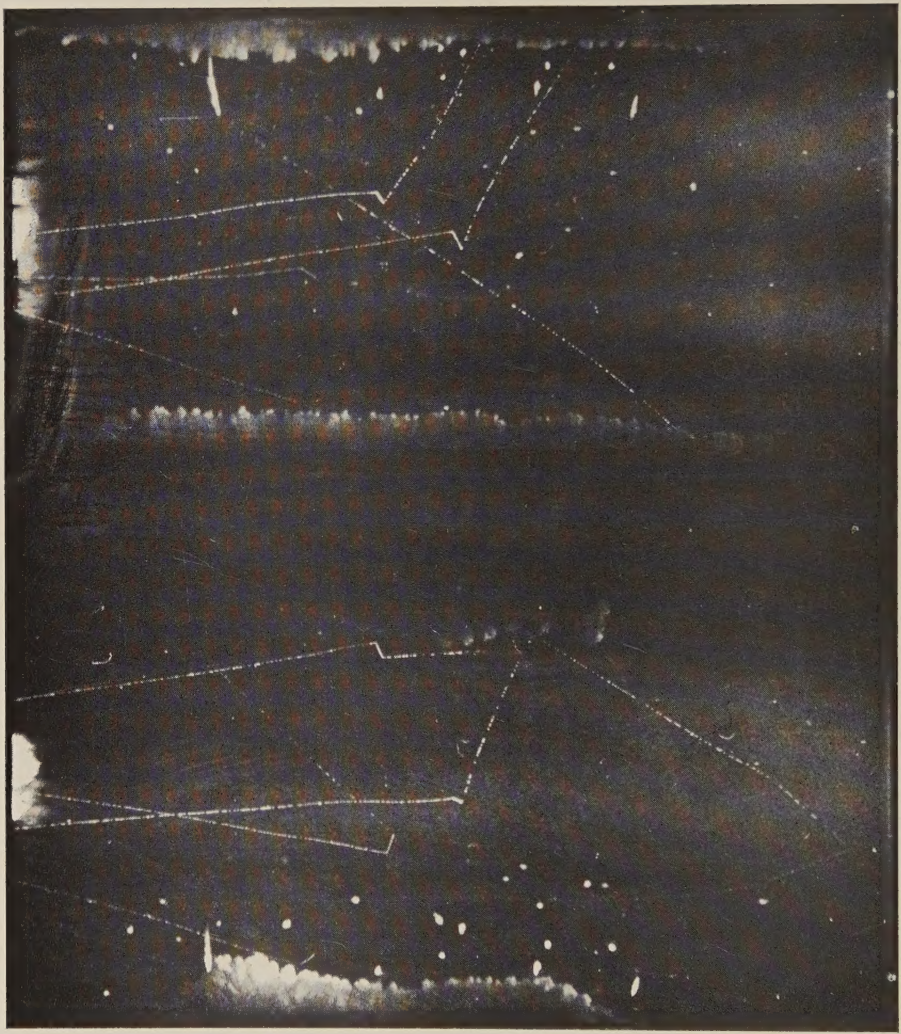

A pair of photographs showing π^+-mesons stopping in the bubble chamber.